NON-LINEAR FRICTIONAL SLIDING CONTACT ANALYSIS USING THE STEP BOUNDARY METHOD WITH EXACT GEOMETRY

By

JOHN DEWS-FLICK

A THESIS PRESENTED TO THE GRADUATE SCHOOL
OF THE UNIVERSITY OF FLORIDA IN PARTIAL FULFILLMENT
OF THE REQUIREMENTS FOR THE DEGREE OF MASTER OF SCIENCE IN
AEROSPACE ENGINEERING

UNIVERSITY OF FLORIDA

2022

Dedicated to my mom Denisé, and my grandparents, Sharon and John Dews for their never-ending support

ACKNOWLEDGMENTS

I would like to express unwavering gratitude to my research adviser, Dr. Ashok Kumar, who taught me my fundamentals as a student and guided me in this research as a Graduate student. His dedication and time commitment were paramount in completing this thesis. This work has greatly enriched my master's education and opened more paths for my future. I also express gratitude to Dr. Bhavani Sankar for being a member of my thesis committee.

TABLE OF CONTENTS

page

ACKNOWLEDGMENTS 4

LIST OF TABLES 8

LIST OF FIGURES 9

LIST OF ABBREVIATIONS 13

1. INTRODUCTION 16

2. TRADITIONAL CONTACT ANALYSIS 19

2.1. Contact Condition 19
2.2. Penalty Method 21
2.3. Lagrangian Multiplier Method 23
2.4. Hertzian Contact 24
2.5. Inclusion of Friction 26
2.6. Contact Analysis Available in Contemporary FEA Software 28

3. THE IMMERSED BOUNDARY METHOD 31

3.1. Fixed Essential Boundary Condition 33
3.2. Sliding Essential Boundary Condition 35
3.3. Volume Integration 37
3.4. IBFEM Solution Structure 38

4. REPRESENTING EXACT GEOMETRY 43

4.1. Traditional Representation of Geometry 43
4.2. Projecting onto Exact Geometry 44
4.2.1. Line and Plane 45
4.2.2. Circles and Spheres 46
4.2.3. Ellipse 47
4.2.4. Cylinder 49
4.2.5. Cone 50
4.2.6. Torus 52
4.2.7. Verifying Projection Methods 54
4.2.8. General Curves & Surfaces 54
4.2.9. Application to FEM 55

5. MODELING CONTACT WITHIN IBFEM 57

5.1. Contact Solution Structure 58
5.2. Contact Area Representation 60

5.3. Non-Linear Automatic Solution 61
5.4. Frictional Contact 64
5.4.1. Tied Formulation 65
5.4.2. Sliding Formulation 66
5.5. Contact Width Growth 66
5.5.1. Enforcing No Penetration 68
5.5.2. Enforcing No Tensile Stress 69
5.5.3. Incrementing the Contact Width 69
5.5.4. Determining the Width Increment 70

6. RESULTS 72

6.1. Effect of Projected Geometry on an Ellipse in Contact 72
6.1.1. Comparison of Contact Width 73
6.1.2. Comparison of Contact Pressure 74
6.1.3. Comparison of Sub Surface Von Mises Stress 75
6.1.4. Displacement results 76
6.2. Mesh Independent Convergence of Contact Width 78
6.2.1. Comparison of Half-Width for Differing Loads 78
6.2.2. Error In Contact Width Across Differing Meshes 79
6.3. Frictionless Contact 80
6.3.1. Contact Width Comparison 81
6.3.2. Displacement Results 82
6.3.3. Von Mises' Stress Field 83
6.4. Partial-Slip: Cylinder on Flat 84
6.4.1. Contact Width and Ratio Comparison 84
6.4.2. Contact Region Shear Stress 85
6.4.3. Contact Region Normal Stress 86
6.4.4. Von Mises Results 86
6.5. Partial-Slip: Cylinder on Cylinder 88
6.5.1. Contact Width and Ratio Comparison 89
6.5.2. Contact Region Normal Stress 90
6.5.3. Stress Fields 90
6.5.4. Displacement results 93
6.6. Partial-Slip: Cylinder on Concave 94
6.6.1. Contact Width and Ratio Comparison 95
6.6.2. Contact Region Shear Stress 96
6.6.3. Contact Region Normal Stress 97
6.6.4. Stress Fields 97
6.6.5. Displacement results 100
6.7. Frictionless Sliding: Cylinder on Wedge 101
6.7.1. Contact Width and Transmitted Force Comparison 103
6.7.2. Stress Fields 103
6.7.3. Displacement results 105

7. CONCLUSION 107

7.1. Conclusion 107
7.2. Future Scope 108

LIST OF REFERENCES 110

BIOGRAPHICAL SKETCH 112

LIST OF TABLES

Table page

Table 6-1. Contact Half-Width comparison for Example 1. 74

Table 6-2. Contact half-width and ratio comparison for Example 4. 85

Table 6-3. Contact half-width and ratio comparison for Example 5 Cylinder-on-Cylinder contact. 89

Table 6-4. Contact half-width and ratio comparison for Example 6. 96

LIST OF FIGURES

Figure page

Figure 2-1. General contact problem between bodies in 2D 19

Figure 2-2. Differing Hertzian contact possibilities within 2D for point-contact. N and Q represent the normal and tangential force transferred through the contact region. 24

Figure 2-3. Analytical shear force distribution through the contact width for various contact force ratios normalized by the friction coefficient μ. 27

Figure 3-1. Examples of IBFEM meshes. a) 2D frame structure immersed within square elements. b) 3D propeller immersed within cubic elements. 31

Figure 3-2. Step boundary region of a part. ϕ is the signed distance function which gives the distance of any point from the surface. $\phi = 0$ on the surface. 33

Figure 3-3. Part with boundaries not aligned with the global coordinate system. The local surface normal n is shown. 35

Figure 4-1. Line segment approximation of an ellipse. With error in the surface normal and the position shown 43

Figure 4-2. Exact surface projection algorithm for a plane 46

Figure 4-3. Exact surface projection algorithm for circles and spheres 47

Figure 4-4. Exact surface projection algorithm for an ellipse 49

Figure 4-5. Exact surface projection algorithm for a cylinder 50

Figure 4-6. Exact surface projection algorithm for a cone 51

Figure 4-7. Exact surface projection algorithm for a torus. 53

Figure 5-1. Underlying grids for each part in a contact problem. Which are connected by the overlapping elements known as contact elements. The contact point in this example is shown by the black dot. 57

Figure 5-2. Compatibility condition for contact. Consider two points that come into contact due originally separated by a displacement Δi. 58

Figure 5-3. Sliding and tied region of a contact area. Measured by half-widths a and c which represent the entire region and tied region. A example cord length is shown measuring from the contact point to an arbitrary point on the boundary. 60

Figure 5-4. Determination if a point on Part 1 is penetrating Part 2. 68

Figure 6-1. Boundary conditions for ellipse on plane contact. 72

Figure 6-2. Comparison of the Von Mises stress plot between (a) projected and (b) non-project results. The only difference between simulations and results is the addition of the ellipse projection algorithm. 73

Figure 6-3. Contact pressure distribution using both the IBFEM method with projection and without projection compared to the analytical solution. 75

Figure 6-4. Subsurface Von Mises stress along the vertical axis from the contact point. 76

Figure 6-5. Projected result displacement magnitude. 77

Figure 6-6. Non-projected result displacement magnitude. 77

Figure 6-7. Boundary conditions for mesh independent convergence analysis. The bottom part is fixed at the bottom, while the top part has a specified displacement. 78

Figure 6-8. Contact half-width computed during eight different analyses while using the same mesh density (25 contact elements). Only the normal load boundary condition was varied between analyses. This is compared to the analytical contact half-width from (2-23) 79

Figure 6-9. Error in contact half-width compared across increasing mesh density. The same boundary conditions were used for all analyses with only the background mesh was modified 80

Figure 6-10. Comparison of mesh densities: (a) Course mesh containing ~5 contact elements (b) Fine mesh containing ~30 contact elements 80

Figure 6-11. Cylinder-on-Cylinder boundary conditions. Both vertical and horizontal displacements are specified. The contact is frictionless with $\mu = 0$. 81

Figure 6-12. The components of displacement for frictionless contact (a) the displacement in the Y direction and (b) the displacement in the x-direction. 82

Figure 6-13. Von Mises Stress for Frictionless contact. This result is expected to match the Hertzian normal force only Von Mises contour plot. 83

Figure 6-14. Cylinder-on-Flat plane boundary conditions. Both vertical and horizontal displacement is applied along the top boundary. 84

Figure 6-15. Shear Stress through the contact half-width compared to the analytical result. Only half of the geometries' contact width is plotted. 85

Figure 6-16. The Normal Stress plotted through the contact region. 86

Figure 6-17. Von Mises' Stress field for cylinder-on-flat contact under partial slip. (a) Full result view (b) Zoomed, contact region result view 87

Figure 6-18. "Stresses produced by a contact with a combined normal and tangential load made visible by polarization optics" courtesy of Valentin Popov, who released this image into the public domain [17]. 88

Figure 6-19. Boundary conditions for Cylinder-on-Cylinder contact under partial-slip. .. 89

Figure 6-20. Normal stress through the contact region for Cylinder-on-Cylinder contact 90

Figure 6-21. Von Mises' Stress for Cylinder-on-Cylinder contact with normal and tangential load 91

Figure 6-22. σyy stress field for Cylinder-on-Cylinder contact with normal and tangential load. 92

Figure 6-23. σxy stress field for Cylinder-on-Cylinder contact with normal and tangential load. 92

Figure 6-24. ux displacement field for cylinder-on-cylinder point contact. 93

Figure 6-25. uy displacement field for cylinder-on-cylinder point contact 94

Figure 6-26. Boundary conditions for Cylinder-on-Concave. Both vertical and horizontal displacements are applied to the top boundary. 95

Figure 6-27. Shear Stress through the contact half-width compared to the analytical result for Cylinder-on-Concave contact. Only half of the geometries' contact width is plotted. 97

Figure 6-28. Normal Stress plotted through the contact region for Cylinder-on-Concave contact 97

Figure 6-29. Von Mises' Stress field for Cylinder-on-Concave contact 98

Figure 6-30. σyy stress field for Cylinder-on-Concave contact 99

Figure 6-31. σxy stress field for Cylinder-on-Concave contact 99

Figure 6-32. ux displacement field for cylinder-on-concave point contact. 100

Figure 6-33. uy displacement field for cylinder-on-concave point contact 101

Figure 6-34. Boundary conditions for Cylinder-on-wedge. Only a vertical displacement on the top boundary is specified. 102

Figure 6-35. Free body diagram of the forces applied to the top cylinder..... 102

Figure 6-36. Von Misses Stress field for cylinder-on-wedge 104

Figure 6-37. (a) σyy stress field (b) σxx stress field for cylinder-on-wedge contact.... 104

Figure 6-38. u magnitude displacement field for cylinder-on-wedge point contact..... 105

Figure 6-39. (a) uy displacement field (b) ux displacement field for cylinder-on-wedge..... 106

LIST OF ABBREVIATIONS

IBFEM	Immersed Boundary Finite Element Method
FEM	Finite Element Method
FEA	Finite Element Analysis
CAD	Computer Aided Design
DOF	Degree of Freedom
RHS	Right Hand Side. (Reference to the RHS of an equation)
LHS	Left Hand Side. (Reference to the LHS of an equation)

Abstract of Thesis Presented to the Graduate School
of the University of Florida in Partial Fulfillment of the
Requirements for the Degree of Master of Science

NON-LINEAR FRICTIONAL SLIDING CONTACT ANALYSIS USING THE STEP BOUNDARY METHOD WITH EXACT GEOMETRY

By

John Dews-Flick

August 2022

Chair: Dr. Ashok V. Kumar
Committee: Dr. Bhavani V. Sankar
Major: Aerospace Engineering

Contact is an important phenomenon to capture within solid mechanics, many methods have been proposed and are in use for traditional methods using conforming meshes. However, these meshes increase complexity, and can lead to distorted elements compared to the uniform structured meshes used within the immersed boundary method finite element method (IBFEM). This present work extends current contact methods within IBFEM to include a new contact representation based on the scaler half-width value of the contact region. The tied formulation is extended to including sliding contact between two bodies. This sliding contact formulation can be used to represent frictionless contact problems. This method can also be applied to partial-slip problems, these problems are static; however, a region of relative slip develops within the outer most contact region. In the partial-slip case this region can be identified by knowing the ratio of the load transferred through the contact region. The need for exact projection of geometry was identified and implemented for differing surface primitives, this allows the exact projection of points onto the surface and determination of the exact normal. Multiple Hertzian and Hertzian-like problems are

considered and compared to the analytical solutions regarding the contact width found, the pressure distribution through the contact region, and the shear stress through the contact region.

CHAPTER 1
1. INTRODUCTION

Contact analysis has four main objectives; determining whether contact is present, isolating the contact region, calculating the magnitude of the forces and stresses within the contact region, and predicting relative motion between the surfaces. Generally, since the contact forces and displacements are not known beforehand, this requires a non-linear solution to develop the contact region while satisfying equilibrium [1].

Contact has been well studied when conforming meshes are considered; thus, these are considered traditional FEA methods. Generally, these methods use very high mesh densities within the contact region. The nodes of the meshes conform to the underlying boundary of the geometry—these often distorted elements lead to both geometric inaccuracy and inaccuracy in the stiffness of the elements. To overcome these inaccuracies, a non-conforming mesh can be used where the nodes of elements are not necessarily on the boundary of the part. Here, the geometry is immersed into a rectangular or cuboid structured mesh, leading to higher accuracy in the underlying approximation. This method is known as the immersed boundary method, further introduced later in Chapter 3 [2].

Contact analysis within IBFEM has been explored in previous work. Burla et al. developed a multi-grid solution structure to handle composite materials [3] which was extended by Tupsakhare, who demonstrated a linear contact formulation using the Hertzian analytical solution to pre-determine the contact region [4]. More recent work by Nittala expands this method to non-linear analysis, where the contact region is no longer known a priori [5]. This present work extends these by implementing a new

method for contact region representation and growth, the addition of sliding frictionless and frictional partial-slip contact, and the exact projection of geometry onto surface primitives. The main goals of this thesis are:

- Represent the surfaces of geometric primitive exactly using the underlying geometric definition of the parts.
- Implement a new contact half-width-based solution structure for representing the contact region and its growth.
- Develop a new contact formulation that can handle sliding in local degrees of freedom
- Develop a solution structure based on contact half-width and the tied ratio to handle partial-slip frictional contact problems

A general outline of each chapter in this thesis follows.

Chapter 2 briefly introduces contact theory within traditional FEA methods and coverage of the Hertzian theory of contact, which is used as an analytical basis for comparison later in this thesis. Contact formulations within traditional FEA theory and commercial applications are also presented.

Chapter 3 reviews the immersed boundary finite element method (IBFEM). Focusing on the application of essential boundary conditions using the step boundary method. The weak form for solution structure (without contact) for IBFEM is also given.

Chapter 4 presents the projection algorithms developed for the most common geometric surface primitives, which allow for exact projection within IBFEM. A discussion is given on projection for generalized surfaces via minimization.

Chapter 5 explains the contact solution structure within the IBFEM framework for both tied and sliding contact regions. The contact half-width-based solution structure is described along with a method for contact growth. An algorithm for computing the contact force is presented, which is used for determining the partial-sliding ratio. A review of the automatic non-linear solution method used for obtaining a solution is also presented.

Chapter 6 is a presentation of contact examples. One example is focused on the effect and the need to project to the exact geometry. Another example studies the mesh dependence of the contact half-width computed; presented to validate the reliability of the solution structure. A frictionless example is given to validate sliding contact. Then multiple Hertzian-like partial-slip problems of various geometry are presented and compared to the analytical solutions presented in Chapter 2.

Chapter 7 contains an extended discussion of the examples, concluding remarks, limiting factors, and the future scope.

CHAPTER 2
2. TRADITIONAL CONTACT ANALYSIS

2.1. Contact Condition

In traditional finite elements, contact problems are generally divided into identifying contact, enforcing equilibrium, then identifying relative motion in the contact region. This generally must be done iteratively as contact is highly non-linear. For example, consider the general 2D contact case shown in Figure 2-1; if a displacement is applied to the secondary body, initially, there will be no resistance, and rigid body motion will occur until the point of contact. This will produce a discontinuous jump in the force-displacement graph.

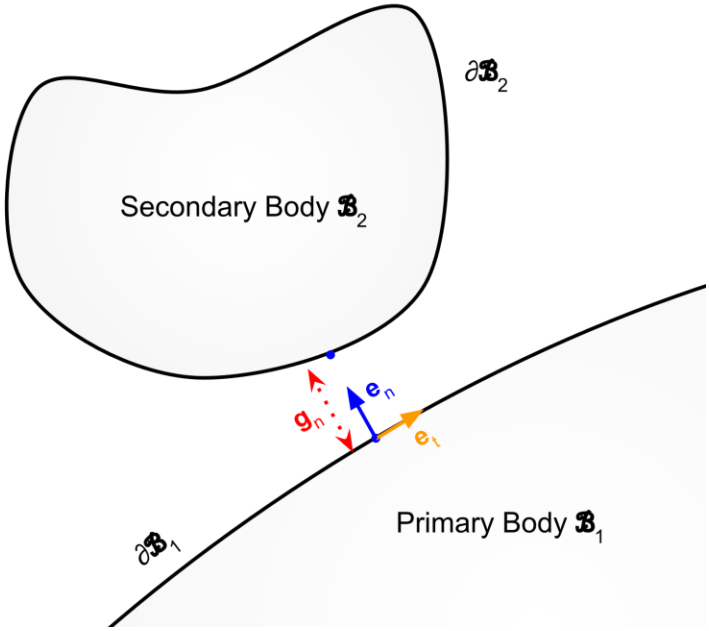

Figure 2-1. General contact problem between bodies in 2D

Generally, for contact problems, one of the two bodies is denoted as the primary surface and the other the secondary. This distinction is somewhat arbitrary and arises from the need that only one surface needs to be searched for penetration from the other surface. For contact to occur between two points, it must be along the normal between

the two surfaces, representing the shortest distance between the two given points. The closest point between the two bodies shown in Figure 2-1 can be found as it will satisfy:

$$(\vec{x}_2 - \vec{x}_1)^T \hat{e}_t = 0 \tag{2-1}$$

Which is to say, a point on the primary body $\vec{x}_1$ is closest to point $\vec{x}_2$ on the secondary body if the vector between them is entirely along the normal direction [1]. If two points satisfy Equation (2-1), they are not necessarily in contact rather, they are the location of closest contact and thus potential contact. The gap between the two points g_n can be determined as:

$$g_n = (\vec{x}_2 - \vec{x}_1)^T \hat{e}_n \tag{2-2}$$

Note the normal gap g_n is a scaler, but its sign indicates if there is penetration. If $\vec{x}_2$ penetrates $\vec{x}_1$ then the gap is negative. Thus, a no penetration condition can be written as [1]:

$$\vec{u}^T \hat{e}_n + g_n \geq 0 \tag{2-3}$$

In the present work, only non-adhesive contact is considered, which means the bodies will not stick together in any form. This implies no tension can be transmitted through the contact region, only compressive forces. This net force is known as the normal contact force or contact pressure P_n. Note that though P_n results in a compressive force but is defined as positive. This results in the following conditions:

$$P_n \geq 0 \tag{2-4}$$

$$P_n[(\vec{x}_2 - \vec{x}_1)^T \hat{e}_n + g_n] = 0 \tag{2-5}$$

Equation (2-5) combines Equations (2-3)(2-4) to create a consistency condition that will always be zero. This is done by considering P_n is zero if there is a gap and that $(\vec{x}_2 - \vec{x}_1)^T \hat{e}_n + g_n$ is zero if the two points are in contact.

The complete solution can be formulated by extending the principle of virtual work for elastic-static problems given as:

$$\underbrace{\int_{\mathcal{B}} \{\delta\varepsilon\}^T\{\sigma\}\, dV}_{\text{Internal Force}} = \underbrace{\int_{\partial\mathcal{B}} \{\delta u\}^T\{t\}dS}_{\text{Surface Traction}} + \underbrace{\int_{\mathcal{B}} \{\delta u\}^T\{b\}\, dV}_{\text{Body Forces}} \tag{2-6}$$

Here $\{\delta\varepsilon\}$ and $\{\delta u\}$ are the virtual strains and displacements. Equation (2-5) will be applied to introduce contemporary methods of contact analysis using the penalty method, augmented Lagrangian methods, and as the basis for the IBFEM contact formulation using the step boundary method.

2.2. Penalty Method

The appropriately named penalty method adds a penalty to the potential energy to enforce the non-penetration condition. Traditionally, this is done by adding a penalty based on the gap g_n between the contact points only when penetration occurs or $g_n < 0$, the total penalty P is defined using the Macaulay bracket $\langle x \rangle$ as [6]:

$$\langle x \rangle = \begin{cases} 0 & x \leq 0 \\ x & x \geq 0 \end{cases} \tag{2-7}$$

$$P = \frac{P_C}{2} \int_{\partial\mathcal{B}} \langle -g_n \rangle^2\, dS \tag{2-8}$$

Were P_N is the penalty parameter for normal contact. This penalty can be included in the variational form in Equation (2-6) as:

$$\delta P = P_C \int_{\partial\mathcal{B}} \delta g_n \langle -g_n \rangle\, dS = P_C \int_{\partial\mathcal{B}} \{\delta u\}^T \langle -g_n \rangle \{\hat{e}_n\}\, dS \tag{2-9}$$

$$\underbrace{\int_{\mathcal{B}} \{\delta\varepsilon\}^T\{\sigma\}\, dV}_{\text{Internal Force}} + \underbrace{P_C \int_{\partial\mathcal{B}} \{\delta u\}^T\langle -g_n\rangle\{\hat{e}_n\}}_{\text{Contact Penalty}} = \underbrace{\int_{\partial\mathcal{B}} \{\delta u\}^T\{t\}dS}_{\text{Surface Traction}} + \underbrace{\int_{\mathcal{B}} \{\delta u\}^T\{b\}\, dV}_{\text{Body Forces}} \quad (2\text{-}10)$$

As can be seen, the contact penalty term $\delta P(u_i, \delta u_i)$, is non-linear, depending on the deformation; thus, Equation (2-10) cannot be solved as a system of linear equations. Instead, a non-linear incremented solution must be used where the total displacement is instead incremented by Δu_i, thus allowing for the re-computation of g_n. To accomplish this, δP must be linearized as:

$$\Delta g_n = \{\overrightarrow{\Delta x}_2 - \overrightarrow{\Delta x}_1\}^T \hat{e}_n = \{\Delta \mathrm{u}\}^T \hat{e}_n \quad (2\text{-}11)$$

$$P(u_i, \delta u_i) \rightarrow P(\Delta u_i, u_i, \delta u_i) = P_C \int_{\partial\mathcal{B}} \{\delta u\}^T\langle -\{\Delta \mathrm{u}\}^T \hat{e}_n\rangle\{\hat{e}_n\}\, dS \quad (2\text{-}12)$$

Here the operator $\langle x\rangle$ still enforces no penalty when the gap is zero if there is no penetration. The penalty term of Equation (2-8) restricts penetration, thus allowing sliding in an unrestricted or frictionless way. To enforce tied or bonded contact, the tangential gap must be considered and penalized as:

$$\delta P = \int_{\partial\mathcal{B}} P_N \delta g_n\langle -g_n\rangle + P_T g_t \delta g_t dS \quad (2\text{-}13)$$

However, if frictional contact is considered instead of a penalty $P_T g_t$, the friction force $\vec{t}_T$ is used such as in [7], [8]:

$$\delta P = \int_{\partial\mathcal{B}} P_N \delta g_n\langle -g_n\rangle + \vec{t}_T \delta g_t dS \quad (2\text{-}14)$$

This substitution will similarly be applied when including friction within the Lagrangian method.

2.3. Lagrangian Multiplier Method

The Lagrangian multiplier method augments the solution structure of the potential energy equation by adding a new unknown, the Lagrange multiplier λ_n. Here the solution is such that the minimum of the augmented potential energy will determine λ_n such that the constraint condition is satisfied. This gives the additional contribution due to contact as:

$$\int_{\partial\mathcal{B}} \lambda_n \delta g_n dS \tag{2-15}$$

As in the above described penalty method, when relative sliding with friction is considered, the additional contact term for the Lagrange method becomes:

$$\int_{\partial\mathcal{B}} \lambda_n \delta g_n + \vec{t}_T \delta g_t \, dS \tag{2-16}$$

Unlike the penalty method here, the multiplier λ_n is an additional variable which must be solved for. This method can be converted back into the penalty method by regularizing via $\lambda_n \approx P_N g_n$ which holds true as $P_N \to \infty$. However, with the exact determination of λ_n only then will $g = 0$ on the contact region. To achieve this while still being able to solve for λ_n the augmented Lagrangian method has been developed as [9]:

$$\int_{\partial\mathcal{B}} \overline{\lambda_n} \delta g_n + P_N \delta g_n \langle -g_n \rangle + \vec{t}_T \delta g_t \, dS \tag{2-17}$$

Here, the augmented Lagrangian $\overline{\lambda_n}$ is updated each iteration loop, note the appearance of the penalty term P_N. There are multiple methods for updating $\overline{\lambda_n}$, the simplest is given as:

$$\overline{\lambda}_{n,new} = \overline{\lambda}_{n,old} + P_n g_{n,new} \tag{2-18}$$

This method has the effect of enforcing $g = 0$ on the contact region, while making the solution to λ_n more approachable. Thus, the augmented Lagrangian method may be considered a combination of the penalty and Lagrangian multiplier methods. A comparison of the accuracy of these methods is given in [10] additional methods, some of which extend the Lagrangian method, are given in [1], [6].

2.4. Hertzian Contact

The analytical solution to contact between two constant curvature surfaces was first published by Heinrich Hertz in 1881 [11]. Originally this work focused on the non-adhesive point-contact between bodies without friction and generally assumes that there is only a normal load N that is applied through the contact region. Some point contact problems are shown in Figure 2-2; note physically that these represent line contact problems.

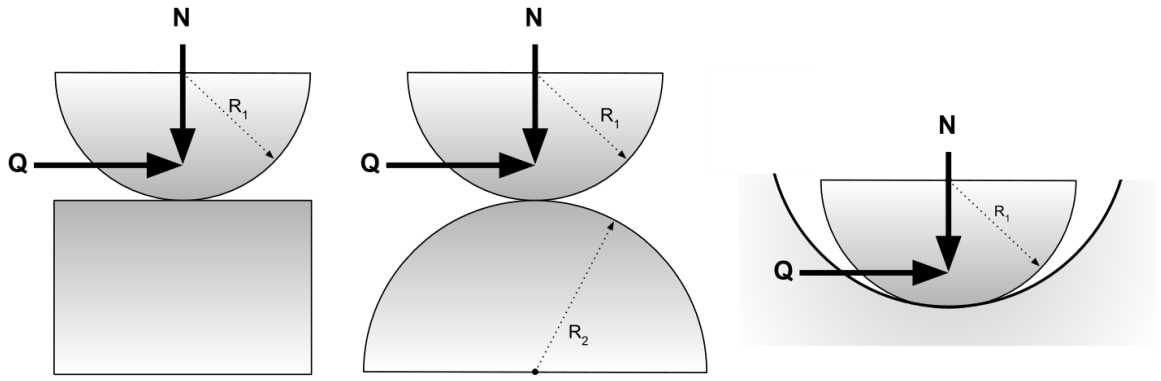

Figure 2-2. Differing Hertzian contact possibilities within 2D for point-contact. N and Q represent the normal and tangential force transferred through the contact region.

In Hertzian theory, the pressure distribution across the contact half-width a is an elliptical distribution given by:

$$p(x) = -p_0\sqrt{1-\left(\frac{x}{a}\right)^2} \tag{2-19}$$

$$p_0 = \frac{2N}{\pi a} \tag{2-20}$$

where p_0 is the peak contact pressure that occurs at the contact point [12]–[15]. A solution for a can be computed analytically if the composite modulus $E^*$and composite radius R^* of the bodies coming into contact are known; these are defined by

$$\frac{1}{E^*} = \frac{1-\nu_1^2}{E_1} + \frac{1-\nu_2^2}{E_2} \tag{2-21}$$

$$\frac{1}{R^*} = \frac{1}{R_1} + \frac{1}{R_2} \tag{2-22}$$

where E_1 and ν_1 are the elastic modulus and Poisson's ratio for part 1, and E_2 and ν_2 for part 2. Note that for a flat plane such as in Figure 2-2, the radius is infinity which has the effect of reducing Equation (2-22) to $R^* = R_1$ and for the concave example the radius would be negative.

The analytical solution for 2D line contact is given as follows [13]:

$$a = \sqrt{\frac{4NR^*}{\pi E^*}} \tag{2-23}$$

Here N is the normal load transferred through the contact. This solution is obtained by equating the integration of Equation (2-19) across the contact region to the total normal load applied N [13]. This analytical method is used to compute the half-width a directly without iterative methods leading to an entirely linear solution structure as pursued in [4]. Although such a solution structure requires prior knowledge of the final load transmitted through the contact and an ability to compute R^* for two given parts.

2.5. Inclusion of Friction

Many have extended this classical solution to include the addition of a tangential force applied to the body. One class of these problems is known as micro-slip or partial slipping, where within the contact area's outermost region relative slip between the parts occurs. In fact, with any applied tangential force, a small region on edge of the contact region will be in slip. The slipping region becomes larger as the ratio of the applied tangential to normal force increases. For linear elastic assumptions, the normal force and shear force effects can be split into two problems [15]. When a shear force is applied, the pressure distribution is still the same as in Equation (2-19). However, once a tangential force is applied to the contact, a net shear force Q must be transferred through the contact region. From the definition of Coulombs' law of friction, the maximum shear force that can be transferred between two points of a body in contact is given by [8]:

$$q_{friction} \leq \mu \sigma_{normal} \tag{2-24}$$

Noting the elliptical distribution of the contact pressure, the max shear force which can be maintained between two points in contact at the very edge of contact tends toward zero; thus, a relative slip occurs in this region. The distribution of shear in the contact region has been derived as

$$q(x) = -\mu p(x) + q'(x) = \mu p_0 \sqrt{1 - \left(\frac{x}{a}\right)^2} + q'(x) \tag{2-25}$$

where $q'(x)$ is a perturbation on the fully sliding solution within the sticking zone [12][15]. The perturbation $q'(x)$ will always be zero within the slip zone $a > |x| > c$ as

within this region the shear is already the maximum. Considering the net shear Q that the contact region needs to transmit, $q'(x)$ has been determined as:

$$q' = -\mu p_0 \left(\frac{c}{a}\right) \sqrt{1 - \left(\frac{x}{c}\right)^2} \qquad \left|\frac{x}{c}\right| < 0 \tag{2-26}$$

Note that the shear distribution $q(x)$ is continuous, but it is not continuously differentiable. The plot of $q(x)$ through the contact width is shown in Figure 2-3, where it has been normalized by the coefficient of friction μ.

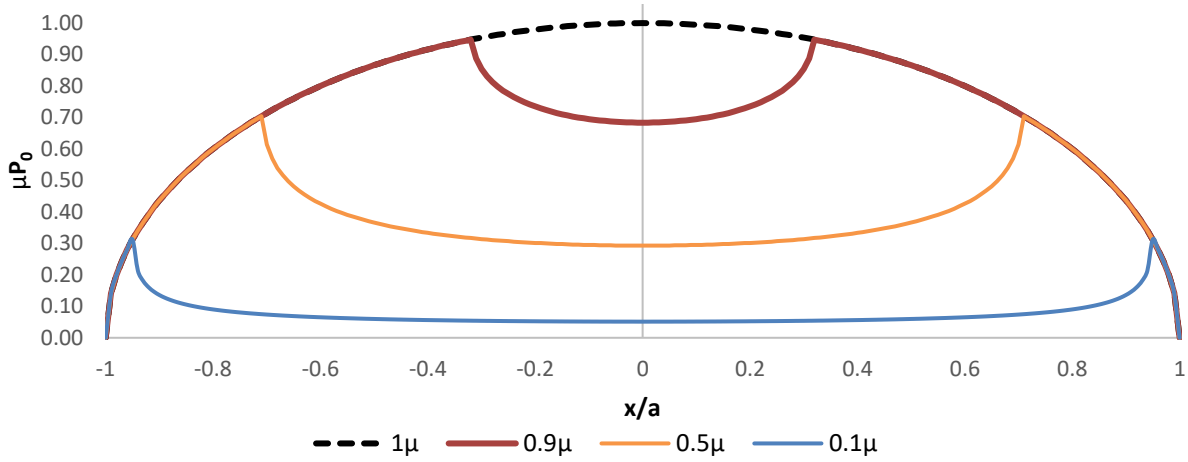

Figure 2-3. Analytical shear force distribution through the contact width for various contact force ratios normalized by the friction coefficient μ.

A contact force ratio β can be defined as a ratio of the shear force and normal force transmitted through the contact by:

$$\beta = \frac{Q}{N} = \frac{\text{Contact Tangental Force}}{\text{Contact Normal Force}} \tag{2-27}$$

Gross slip or sliding will occur when $Q \geq \mu P$ or $\beta \geq \mu$, which would indicate that the tied region c is equal to zero (as the region is entirely sliding). The gross slip condition is represented by the dashed line in Figure 2-3 where $\frac{\beta}{\mu} = 1$. Taking the integral of Equation (2-25) across the contact region yields the equations:

$$Q = \frac{f p_0 \pi}{2a}(a^2 - c^2) \tag{2-28}$$

$$\frac{c}{a} = \sqrt{1 - \left|\frac{Q}{\mu N}\right|} = \sqrt{1 - \left|\frac{\beta}{\mu}\right|} \quad \text{(2D)} \tag{2-29}$$

$$\frac{c}{a} = \sqrt[3]{1 - \left|\frac{\beta}{\mu}\right|} \quad \text{(3D)} \tag{2-30}$$

Equation (2-29) gives the contact width ratio c/a as a function of the contact load ratio β and friction coefficient μ. Similarly, the contact width ratio is defined for the 3D case in Equation (2-30) and have no dependence on the geometry. For constant curvatures, some analytical solutions for the stress distribution have been found for both cases in 2D and 3D [12], [15] under linear strain assumptions.

2.6. Contact Analysis Available in Contemporary FEA Software

Contact analysis solutions are provided in various commercial software and in a few free applications. The implementations generally fall into three categories listed in order of increasing computational cost: bonded, no-penetration, and no penetration with friction. The above terms are based on the terminology used in SolidWorks FEA [16]. The most general of these cases is contact without penetration and with friction, which is defined by the requirement that the two bodies cannot penetrate each other, and an additional friction force is enforced. The friction force in this case is equal to Equation (2-24) based on a specified material friction coefficient. In this work, the following terms will be used to describe the relative motion of the two bodies: tied, fully sliding, and sliding with friction.

Physically speaking, tied (or bonded) can be thought of as when two surfaces come into contact; they forever remain in contact. In effect, there is an infinite coefficient of friction such that no tangential force will cause relative displacement once two

surface points come in contact. Altogether for problems without gross sliding, this is a good approximation, and for problems without tangential forces, such as with the classical Hertz problem with only normal force, the tied assumption will provide a result identical to the analytical solution [5]. At the tips of a contact region, the normal force relative to the surface between the two parts trends toward zero. Since the max friction force is a function of normal force, some slipping will always occur at the tips if a net shear force is transferred through the contact [12]. With a tied assumption, when a tangential force is applied, stress singularities can occur at the contact edges since the shear force needed within this region to enforce the no sliding condition tends toward infinity [15]. However, the solution recovered is still generally valid if gross slip is not expected.

Sliding contact is similar to the tied condition, but there is only a restriction that the two parts can’t penetrate, transferring only a normal force with respect to the contact surface. Therefore, the coefficient of friction is assumed to be equal to zero. While physically impossible, this analysis method provides a simplified way to simulate contact while allowing gross sliding. For the Hertzian problem with tangential force, at least under linear assumptions, the normal force is a decoupled problem from the shear force [15]. A primary limitation is the neglection of friction makes this assumption unsuitable for simulation of structures that are unconstraint in the absence of friction.

Sliding with friction is a combination of the tied and sliding contact method. According to Hertz's contact theory, a contact region under shear experiences a partial slip. The region on the inside of the contact area is tied since the inequality of Equation (2-24) is satisfied. Within the sliding region, instead, Equation (2-24) becomes an

equality (or one could say it is at the maximum friction) since the normal force at the edges is not enough to fully resist sliding between the surfaces. This results in two distinct regions, one tied and the other slipping [14], [17]. In cases where the whole region is slipping, gross sliding occurs. These situations fall outside the scope of methodology presented in this work as, generally, the bodies are no longer static. However, a constrained frictionless example is given in Example 3 which includes some gross slip between the bodies.

CHAPTER 3
3. THE IMMERSED BOUNDARY METHOD

The immersed boundary finite element method (IBFEM) is an extension of traditional finite element analysis without the need for a mesh that conforms to the part's geometry. Instead, with IBFEM, one considers a body (or part) that is immersed into a mesh of rectangles or cuboids; this is shown in 2D and 3D in Figure 3-1. The motivation behind this method is both a simplification of meshing for analysis of parts as well as a more exact integration and approximation by using elements that are square or cubic.

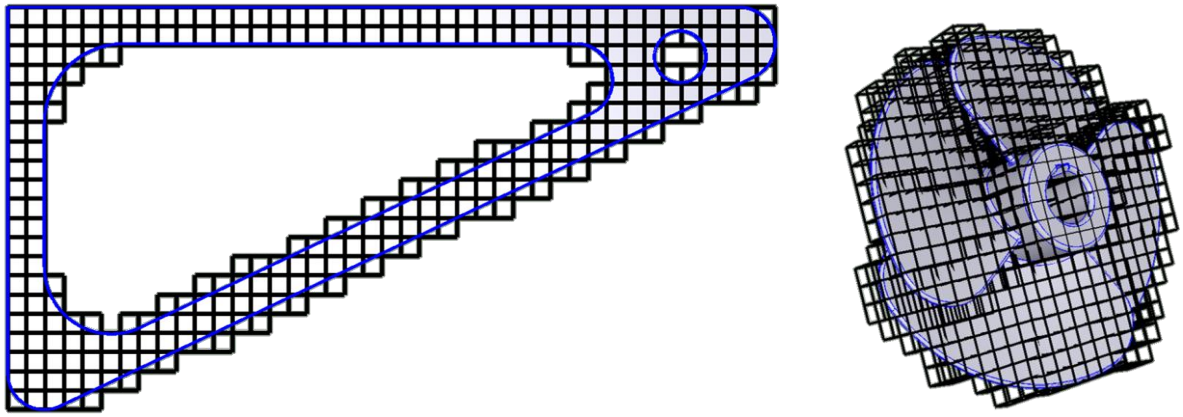

a) b)

Figure 3-1. Examples of IBFEM meshes. a) 2D frame structure immersed within square elements. b) 3D propeller immersed within cubic elements.

Simplified meshing is achieved by an initial structured mesh. Consider the meshing process in IBFEM. The user specifies an initial mesh size or counts, determining the element dimensions. A background mesh is constructed using the bounding box of the geometry, then any elements which do not have any volume of the part within them are eliminated. This leaves two classes of elements: ones completely within the part and those on the boundary of the part. Invoking the immersion analogy, if a volume is subdivided into a bunch of cubes, then the body is immersed within that volume. Some of the cubes will still contain nothing and are discarded, others will be

completely within the part, and some will only be partially occupied by the part. The boundary elements in Figure 3-1 are those which intersect with the boundary, which is represented by the blue lines. Computationally this is much faster than generating a mesh that directly conforms to the geometry; that said, polygon slicing is required for boundary elements within the IBFEM for volume integration.

The idea of achieving more exact integration follows from using completely cubic or square elements. For elements that are completely within the part, the stiffness matrix is exact, and there are direction solutions for the stiffness without the need for numerical integration. This is because the Jacobian for rectangular and cuboid elements are constant, taking on values proportional to the side length ratios. Generally, but not necessarily, within IBFEM, all side lengths are the same; this further reduces the Jacobian to a single value in all spatial directions. The Jacobian is still constant for boundary elements, but a volume integration is only performed for the region occupied by the part. This is compared to traditional FEM meshes, which are skewed or otherwise deformed.

Consider from traditional FEM the displacement approximation of a 2D element with n nodes; which is nothing more than the application of the element shape functions to approximate the displacement within the element:

$$\{u^h\} = \underbrace{\begin{bmatrix} N_1 & 0 & \dots & N_n & 0 \\ 0 & N_1 & \dots & 0 & N_n \end{bmatrix}}_{2\times 2n} \begin{Bmatrix} q_{1x} \\ q_{1y} \\ \dots \\ q_{nx} \\ q_{ny} \end{Bmatrix} = [N]\{X_e\} \tag{3-1}$$

Within IBFEM, the approximation of $\{u\}$ is modified from $\{u^h\}$ to enforce essential boundary conditions. In the absence of these, $\{u\}$ reduces to $\{u^h\}$. Alike traditional finite element methods, implicit boundary conditions, such as traction on a surface, can be

applied by integrating along the surface to solve for the force contribution to each element node. However, applying an essential boundary condition, such as fixed displacement in solid mechanics, is not as straightforward since the boundaries do not necessarily conform to the mesh in IBFEM.

3.1. Fixed Essential Boundary Condition

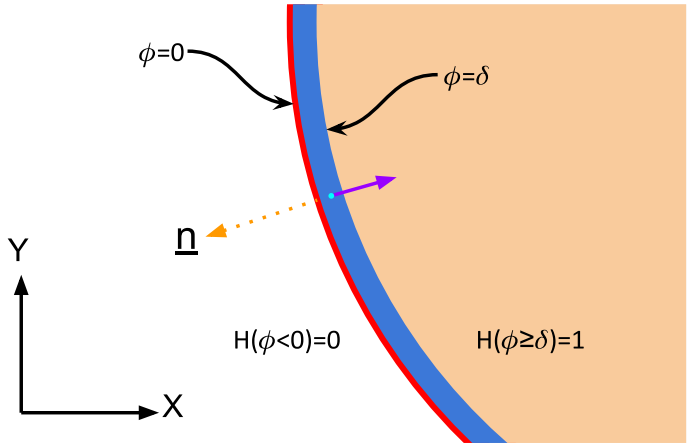

Figure 3-2. Step boundary region of a part. ϕ is the signed distance function which gives the distance of any point from the surface. $\phi = 0$ on the surface.

In traditional FEM, essential boundary conditions are imposed by specifying displacement at nodes for specified degrees of freedom. This allows one to strike these equations from the final assembly. If a non-zero displacement is specified for a particular DOF of a node, the additional force from that equation must be accounted for as an external force in the RHS of the assembled problem $[K]\{X\} = \{F\}$. Within IBFEM, the nodes are no longer necessary on the edge of a part; this makes specifying displacements and striking nodes not feasible. To specify a displacement a_i on a boundary, the following solution structure has been proposed [2]:

$$u_i = H_{ij}u_i^h + \left(\delta_{ij} - H_{ij}\right)a_i \tag{3-2}$$

The variable $\{\mathrm{u}^{\mathrm{h}}\} = [N]\{X_e\}$ is defined as the underlying mesh displacement, and the matrix H_{ij}, which is generally diagonal, enforces the specified boundary condition a_i. Equation (3-2) can also be written more compactly by introducing $\left[\overline{N}\right] = [H][N]$ as:

$$\{u\} = \left[\overline{N}\right]\{X_e\} + ([I] - [H])\{a\} \tag{3-3}$$

While binary step functions can be used to satisfy Equation (3-2), doing so is prone to numerical inaccuracy and produces infinite derivatives. Instead, an approximate step function $\mathrm{H}(\phi)$ is used. It can be noted that as the boundary region δ approaches zero, H approaches the unit step function [2]. The value ϕ is the signed distance function from the body's surface. Outside of the body, the step value ϕ is negative, inside of the body ϕ is positive, and on the boundary the step value is ϕ zero; this is shown in Figure 3-2. $\mathrm{H}(\phi)$ is defined as a function of the signed distance ϕ as:

$$\mathrm{H}(\phi) = \begin{cases} 1 & \phi \geq \delta \\ \dfrac{\phi}{\delta}\left(2 - \dfrac{\phi}{\delta}\right) & 0 \leq \phi \leq \delta \\ 0 & \phi < 0 \end{cases} \tag{3-4}$$

This is known as the step boundary method, which is the basis for enforcing essential boundary conditions within IBFEM [2].

For example, consider when all degrees of freedom have a specified displacement $a_i = (u_0, v_0, w_0)$ on the boundary. To satisfy this condition, Equation (3-2) must reduce to $u_i = a_i$ on the boundary, suggesting H_{ij} will take on the form:

$$H_{ij} = \begin{bmatrix} \mathrm{H}(\phi) & & \\ & \mathrm{H}(\phi) & \\ & & \mathrm{H}(\phi) \end{bmatrix} \tag{3-5}$$

Now consider restricting only some degrees of freedom such that $a_i = (u_0, \mathbf{free}, w_0)$. To satisfy these boundary conditions, Equation (3-2) must instead reduce to $u_x = u_0,\ u_y = u_y^h,\ u = w_0$. Meaning H_{ij} will take on the form:

$$H_{ij} = \begin{bmatrix} \mathrm{H}(\phi) & & \\ & 1 & \\ & & \mathrm{H}(\phi) \end{bmatrix} \tag{3-6}$$

Generally, if we are considering a local coordinate system L where a_i^L can be expressed. H_{ij}^L will always be a diagonal matrix defined by the vector H_i^L as

$$H_{ij}^L = \delta_{ij} H_i^L$$
$$H_i^L = \begin{cases} \mathrm{H}(\phi) & a_i^L \quad \text{is not } free \\ 1 & a_i^L \quad \text{is } free \end{cases} \tag{3-7}$$

That is to say H_{ij} will be diagonal if $H_i^L = \mathrm{H}(\phi)$ meaning every DOF is fixed, such as in Equation (3-5). H_{ij} will also be diagonal if the coordinate system a_i^L is the same as the global coordinate system, such as in Equation (3-6).

3.2. Sliding Essential Boundary Condition

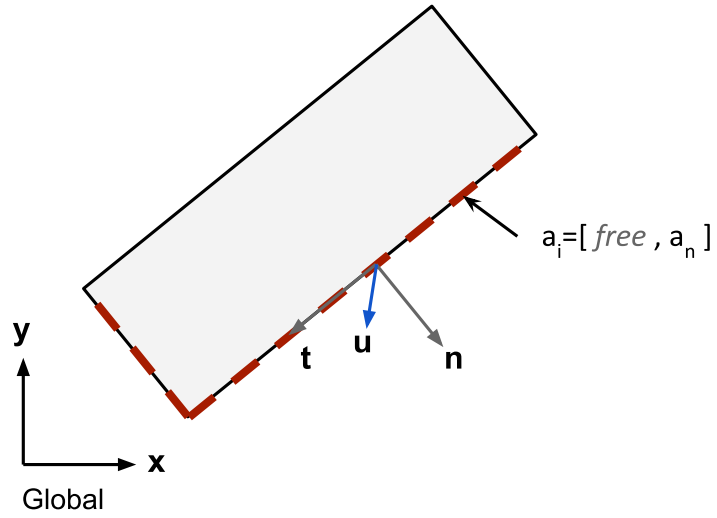

Figure 3-3. Part with boundaries not aligned with the global coordinate system. The local surface normal $\hat{n}$ is shown.

Now consider a boundary that is not aligned with the global coordinate system, such as the one shown in Figure 3-3. A displacement may be specified along the normal direction while allowing the tangential direction to be free or sliding. This is easily represented in a coordinate system local to the surface, such as: $a_i^L = (free, a_n, free)$. However, a_i^L cannot be logically represented in the global coordinate system since the notion of "free" loses meaning with respect to the global coordinate system. Such a sliding boundary condition must be defined with respect to the local surface as in Equation (3-7). Consider a rotation matrix $[R]$ defined between the displacement in the local coordinate system u_i^L and the global coordinate system u_i such as:

$$u_i^L = R_{ij} u_j \tag{3-8}$$

Then Equation (3-25) is transformed using $[R]$ as:

$$\underbrace{u_i^L = H_{ij}^L u_j^{L,h} + \left(\delta_{ij} - H_{ij}^L\right) a_j^L}_{\substack{\text{Local Coordinate System.} \\ H^L \text{ is always diagonal}}} \quad \leftrightarrow \quad \underbrace{u_i = H_{ij} u_j + \left(\delta_{ij} - H_{ij}\right) a_j}_{\text{Global Coordinate System}} \tag{3-9}$$

However, as noted for an arbitrary aligned sliding or "free" boundary condition, a_i^L seemly cannot be readily converted to the global system a_j. Although, it has been shown that any value can be assigned to the free components of a_i^L since, in the end, its effect simply drops out because of the construction of H_{ij}^L. This is proven below in 2D when only the local surface normal direction is fixed. Consider a rotation matrix $[R]$ which maps the local coordinate system to the global one as defined in Equation (3-8). This matrix can be constructed using the local normal of a point on a surface, as shown in Figure 3-3. In 2D, this rotation can be represented using a single angle θ as

$$[R] = \begin{bmatrix} c & s \\ -s & c \end{bmatrix} = \begin{bmatrix} \cos(\theta) & \sin(\theta) \\ -\sin(\theta) & \cos(\theta) \end{bmatrix} \tag{3-10}$$

$$[H^L] = \begin{bmatrix} 1 & \\ & \mathrm{H}(\phi) \end{bmatrix}$$

$$[H] = [R]^T[H^L][R] = \begin{bmatrix} -s^2\,(\mathrm{H}-1) & c\,s\,(\mathrm{H}-1) \\ c\,s\,(\mathrm{H}-1) & -c^2\,(\mathrm{H}-1) \end{bmatrix}$$

$$\{a^L\} = \begin{Bmatrix} a_t \\ a_n \end{Bmatrix} = [R]\{a\}$$
$$\{a\} = [R]^T\{a^L\} = \begin{Bmatrix} a_t\,c - a_n\,s \\ a_n\,c + a_t\,s \end{Bmatrix}$$

$$[H]\{a\} = \begin{Bmatrix} \mathrm{H}\,a_n\,s^3 - a_n\,s^3 - a_n\,c^2\,s + \mathrm{H}\,a_n\,c^2\,s \\ a_n\,c^3 - \mathrm{H}\,a_n\,c^3 + a_n\,c\,s^2 - \mathrm{H}\,a_n\,c\,s^2 \end{Bmatrix} = \begin{Bmatrix} a_n\,s\,(\mathrm{H}-1) \\ -a_n\,c\,(\mathrm{H}-1) \end{Bmatrix} \tag{3-11}$$

It can be seen from the expansion of Equation (3-11) that by imposing the sliding condition within $[H^L]$ (i.e. setting the local tangential direction to one), that a_t has no effect on the final result and can take on any value even after transformation.

Equation (3-9) can be written for 2D with sliding allowed in the tangential direction using matrix notation as:

$$\begin{Bmatrix} u_x \\ u_y \end{Bmatrix} = \underbrace{[R]^T \begin{bmatrix} 0 & \\ & H \end{bmatrix} [R]}_{[\dot{H}]} \begin{Bmatrix} u_x^h \\ u_y^h \end{Bmatrix} + [R]^T \begin{bmatrix} 0 & \\ & 1-\mathrm{H} \end{bmatrix} [R] \begin{Bmatrix} a_x \\ a_y \end{Bmatrix} \tag{3-12}$$

The second term, in this case, is dependent only upon the specified displacement normal to the sliding direction a_n. In practice a_n is often specified as zero displacements, thus eliminating the second term from Equation (3-12).

3.3. Volume Integration

Integrating across the part volume also required a different treatment in IBFEM than traditional FEA methods but only for boundary elements. For completely full elements or rather ones completely immersed within the body, the volume integration reduces to traditional methods. In fact, some exact solutions for the stiffness of rectangular and cuboid elements do exist, which can further reduce the computational

requirement for these elements [18]. In addition, the fact that all the elements often have the same size indicates that the complete elements will all have the same stiffness (for some analysis types), which can be leveraged to reduce computational requirements further. However, for boundary elements, one must perform numerical integration of only the volume within the element which is occupied by the part. This can be accomplished by splitting the occupied region within the element into approximate triangles or tetrahedrons. For each of these regions, numerical integration can be performed, and their contribution is added to the element's stiffness [2]. Similarly, this can be applied to any volume integration, such as the inclusion of a body force.

3.4. IBFEM Solution Structure

For static solid mechanics problems, the principle of virtual work is given as:

$$\underbrace{\int_{\mathcal{B}} \{\delta\varepsilon\}^T\{\sigma\}\, dV}_{\text{Internal Force}} = \underbrace{\int_{\partial\mathcal{B}} \{\delta u\}^T\{t\}dS}_{\text{Surface Traction}} + \underbrace{\int_{\mathcal{B}} \{\delta u\}^T\{b\}\, dV}_{\text{Body Forces}} \tag{3-13}$$

$$\sum_{e=1}^{NE} \int_{\mathcal{B}} \{\delta\varepsilon\}^T\{\sigma\}\, dV = \sum_{e=1}^{NBE} \int_{\partial\mathcal{B}} \{\delta u\}^T\{t\}\, dS + \sum_{e=1}^{NE} \int_{\mathcal{B}} \{\delta u\}^T\{b\}\, dV \tag{3-14}$$

Here $\{\delta\varepsilon\}$ is the virtual strain, $\{\delta u\}$ is the virtual displacement, $\{\sigma\}$ is the stress, $\{t\}$ and $\{b\}$ are external surface tractions and body forces. To apply Equation (3-13), first consider the definition of strain under small-strain theory. For this, the linear strain operator ∇_s is introduced as:

$$\{\varepsilon\} = \begin{Bmatrix} \varepsilon_1 \\ \varepsilon_2 \\ 2\varepsilon_{12} \end{Bmatrix} = \begin{Bmatrix} \dfrac{\partial u_1}{\partial x_1} \\ \dfrac{\partial u_2}{\partial x_2} \\ \dfrac{\partial u_1}{\partial x_2} + \dfrac{\partial u_2}{\partial x_1} \end{Bmatrix} = \nabla_s(u_i) \tag{3-15}$$

which, when applied to the solution structure, Equation (3-25) yields the following result for strain:

$$\{u\} = [H][N]\{X_e\} + [I - H]\{a\}$$

$$\nabla_s(u_i) = \nabla_s([H][N])\{X_e\} - \nabla_s([H])\{a\} \tag{3-16}$$

$$\{\varepsilon\} = \nabla_s(u_i) = ([\nabla_s H][N] + [\mathrm{H}][\nabla_s N])\{\mathrm{X_e}\} - \nabla_s([H])\{a\}$$

$$\left[\overline{B}\right] = \nabla_s\left[\overline{N}\right] = \nabla_s([H][N]) = [\nabla_s H][N] + [\mathrm{H}][\nabla_s N]$$

$$[B] = \nabla_s[N] \tag{3-17}$$

Here $[B]$ is the same as the strain displacement matrix obtained in traditional FEM [18] while $\left[\overline{B}\right]$ is the modified form that allows for the inclusion of the essential boundary condition. For boundaries that do not have specified essential boundary condition $\left[\overline{B}\right]$ simply reduces to $[B]$ as can be shown from Equation (3-17) when $[H]$ is constant. The extra strain associated with $\{a\}$ is $\nabla_s([H])\{a\}$ similarly the force due to $\{a\}$ would become $[C]\nabla_s([H])\{a\}$. This extra force only occurs for a non-zero fixed displacement, which is analogous to traditional FEA where one must compute the RHS contribution from a specified displacement on a node before striking it from the final assembly. However, it may be noted the value of $\nabla_s([H])\{a\}$ is not equal to the externally applied load. Rather it is the force required to overcome the extra stiffness associated with the essential boundary condition and move the boundary by the specified amount.

The term $\nabla_s([H])$ is the linear strain operator applied to the $[H]$ matrix. Considering the sliding condition, $[H]$ is not a diagonal matrix. Rather it is defined as:

$$[H] = [R]^T[H^L][R] = \begin{bmatrix} H_{11} & H_{12} \\ H_{12} & H_{22} \end{bmatrix} \tag{3-18}$$

$$[\partial H] \equiv \nabla_s([H]) \tag{3-19}$$

Computing $[\partial H]$ requires the spatial gradient of $[H]$ which normally results in a 3rd order tensor as $[H]$ is a 2nd order tensor. However, if the symmetry of $[H]$ is leveraged, the spatial gradient of $[H]$ in 2-dimensions can be written compactly as:

$$\nabla H = \begin{bmatrix} \frac{\partial H_{11}}{\partial x} & \frac{\partial H_{11}}{\partial y} \\ \frac{\partial H_{22}}{\partial x} & \frac{\partial H_{22}}{\partial y} \\ \frac{\partial H_{12}}{\partial x} & \frac{\partial H_{12}}{\partial y} \end{bmatrix} \tag{3-20}$$

Considering the definition of ∇_s the matrix $[\partial H]$ can be computed as

$$[\partial H] = \begin{bmatrix} \frac{\partial H_{11}}{\partial x} & \frac{\partial H_{12}}{\partial x} \\ \frac{\partial H_{21}}{\partial y} & \frac{\partial H_{22}}{\partial y} \\ \frac{\partial H_{11}}{\partial y} + \frac{\partial H_{21}}{\partial x} & \frac{\partial H_{22}}{\partial x} + \frac{\partial H_{12}}{\partial y} \end{bmatrix} \tag{3-21}$$

The matrix $[\partial H]$ can be constructed using the terms of the special gradient ∇H. If all local/global degrees of freedom are fixed at an essential boundary condition, then $[H]$ is diagonal as shown in Equation (3-5). This reduces $[\partial H]$ to:

$$[\partial H] = \begin{bmatrix} \frac{\partial H_{11}}{\partial x} & \\ & \frac{\partial H_{22}}{\partial y} \\ \frac{\partial H_{11}}{\partial y} & \frac{\partial H_{22}}{\partial x} \end{bmatrix} \tag{3-22}$$

The above equation is only true if $[H]$ is diagonal, which is to say that all local degrees of freedom are fixed via the essential boundary condition. Equation (3-17) applies to all cases as the non-diagonal terms reduce to zero. Consider when $[H^L]$ is allowed to slide in the local x-direction as shown in Equation (3-6). If the rotation matrix from the local to

the global coordinate system is used as defined in Equation (3-8) the global $[H]$ becomes:

$$[H] = [R]^T \begin{bmatrix} 1 & 0 \\ 0 & H(\phi) \end{bmatrix} [R] = \begin{bmatrix} {R_{11}}^2 + H(\phi){R_{21}}^2 & R_{11}\,R_{12} + R_{21}\,R_{22}\,H(\phi) \\ R_{11}\,R_{12} + R_{21}\,R_{22}H(\phi) & {R_{12}}^2 + H(\phi)\,{R_{22}}^2 \end{bmatrix} \quad (3\text{-}23)$$

$$[\partial H] = \begin{bmatrix} {R_{21}}^2 \dfrac{\partial H(\phi)}{\partial X_1} & R_{21}\,R_{22}\dfrac{\partial H(\phi)}{\partial X_1} \\ R_{21}\,R_{22}\dfrac{\partial H(\phi)}{\partial X_2} & {R_{22}}^2\dfrac{\partial H(\phi)}{\partial X_2} \\ {R_{21}}^2\dfrac{\partial H(\phi)}{\partial X_2} + R_{21}\,R_{22}\dfrac{\partial H(\phi)}{\partial X_1} & {R_{22}}^2\dfrac{\partial H(\phi)}{\partial X_1} + R_{21}\,R_{22}\dfrac{\partial H(\phi)}{\partial X_2} \end{bmatrix} \quad (3\text{-}24)$$

While $[R]$ is a function of the local normal, it is assumed that $\frac{\partial R_{ij}}{\partial x_i}$ is zero. The spatial derivatives of H can be found by applying the chain rule.

$$\frac{\partial H(\phi)}{\partial x_i} = \frac{\partial H}{\partial \phi}\frac{\partial \phi}{\partial x_i} \quad (3\text{-}25)$$

The value $\frac{\partial \phi}{\partial x_i}$ is the derivative of the boundary distance function with respect to the spatial direction x_i the value of $\frac{\partial \phi}{\partial x_i}$ Is simply the i^{th} component of the normal at that point. This notion $\frac{\partial \phi}{\partial x_i} = \hat{n}_i$ has been rigorously proven within [19].

The virtual strains can be represented by considering a virtual displacement field $\{\delta X\}$ which is applied to the structure resulting in a virtual displacement:

$$\{\delta u\} = [\overline{N}]\{\delta X\} \quad (3\text{-}26)$$

Applying the linear strain operator ∇_s gives the virtual strain as:

$$\{\delta \varepsilon\} = \left[\overline{B}\right]\{\delta X\} \quad (3\text{-}27)$$

The virtual displacements are zero on the surface of the part with a prescribed displacement (essential boundary condition), making the work done by its reactions

zero. Therefore, the value $\{a\}$ does not appear in the virtual field's definition. The stress within an element can be written considering an isotropic linear material as:

$$\{\sigma\} = [C]\{\varepsilon\} = [C]([\bar{B}]^T\{\mathrm{X_e}\} - [\partial H]\{a\}) \tag{3-28}$$

Combining these results into the principle of virtual work Equation (3-12) yields:

$$\sum_{e=1}^{NE}\{\delta X_e\}^T\left(\underbrace{\int_{\mathcal{B}}[\bar{B}]^T[C][\bar{B}]dV}_{\text{Element Stiffness }[\mathrm{K_e}]}\{X_e\} - \underbrace{\int_{\partial\mathcal{B}}[\bar{B}]^T[C][\partial H]\{\mathrm{a}\}\,dS}_{\text{Essential Boundry Load }\{F_a\}}\right) = \sum_{e=1}^{NE}\{\delta X_e\}^T\underbrace{\int_{\partial\mathcal{B}}[\bar{N}]^T t\,dS}_{\text{Applied Traction }\{\mathrm{F_t}\}} + \sum_{e=1}^{NE}\{\delta X_e\}^T\underbrace{\int_{\mathcal{B}}[\bar{N}]^T b\,dV}_{\text{Body Forces }\{\mathrm{F_b}\}} \tag{3-29}$$

$$\{F_a\} = \int_{\mathcal{B}}[\bar{B}]^T[C][\partial H]\{\mathrm{a}\}\,dV \tag{3-30}$$

$$\underbrace{\sum_{e=1}^{NE}\{\delta X_e\}^T[K_e]\{X_e\}}_{\text{Element Stiffness }(LHS)} = \underbrace{\sum_{e=1}^{NE}\{\delta X_e\}^T(\{\mathrm{F_t}\} + \{\mathrm{F_b}\} + \{F_a\})}_{\text{Element Force (RHS)}} \tag{3-31}$$

The load $\{F_a\}$ is the force needed to apply a non-zero boundary displacement of $\{\mathrm{a}\}$. The need for this force can be understood by considering the extra stiffness which is applied near the specified essential boundary conditions. For this extra stiffness, there is a corresponding force $\{F_a\}$ needed to displace the boundary to the specified displacement $\{\mathrm{a}\}$. This force is not to be confused with the reaction force resultant from the specified essential boundary condition.

CHAPTER 4
4. REPRESENTING EXACT GEOMETRY

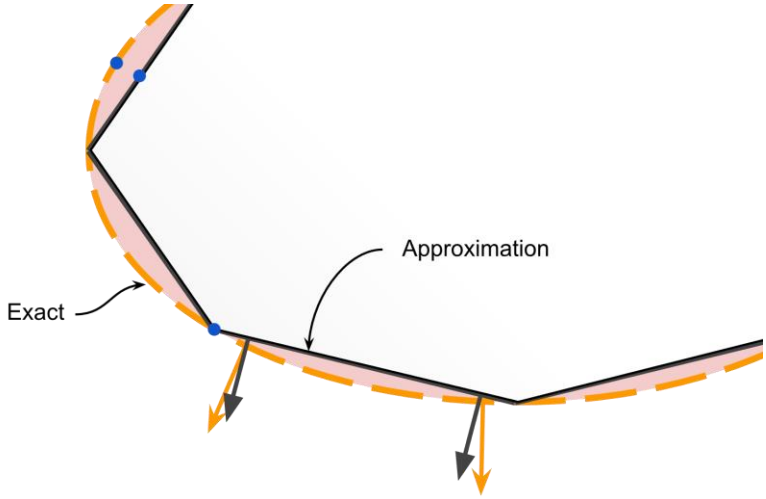

Figure 4-1. Line segment approximation of an ellipse. With error in the surface normal and the position shown

4.1. Traditional Representation of Geometry

Today most engineered parts are designed within CAD applications which are used to make drawings for the manufacture or, in most cases, directly exported to an automated manufacturing process. Most of these CAD applications combine Boolean operations to differing underlying surface elements; however, the output is almost always approximated into triangles (and lines) such as in the common STL format. It can be generally shown that with a finer approximation, your result tends toward the true geometry. This is analogous but distinct to finer meshes in IBFEM. For example, if an ellipse is represented by the line segment approximation as in Figure 4-1. No matter how fine the mesh is there will always remain geometric inaccuracy. For the geometry in Figure 4-1, consider integration along the boundary of the straight-line approximation as opposed to the true ellipse; the normal is constant along the straight lines, and there is an obvious position inaccuracy, except at the vertices. One can also observe that for a

concave surface, you will have an under approximation of stiffness. While for convex surfaces, you will have an over-approximation of stiffness. Of course, in many FEA programs, the mesh is generated using the exact geometry; thus, a more exact answer is found from a progressively finer mesh, but this is done at the expense of more elements and is still an approximation. Another solution to geometric inaccuracy leverages isogeometric analysis using NURB basis functions, which allows one to represent exact geometry or a close approximation at the expense of higher computational requirements. Contact has been successfully implemented within isogeometric analysis using a penalty function [20].

Along with the common STL representation of the geometry of a part, there are also formats that define the underlying surface and curve representations of a part. This includes all the surface and curve primitives one can consider such as: lines, circles, ellipses, planes, cones, spheres, ellipsoids, and tori. One such file format is ACIS; alternatively, such as in this work, a JSON API provided by the CAD software OnShape was utilized to obtain the exact geometry information for a part. This allows one to design a part within the OnShape CAD application and then import not only the approximated triangles and lines but also the surface definitions.

4.2. Projecting onto Exact Geometry

A solution to the use of inaccurate line segments is to project the needed points and normals of a curve or surface. This is accomplished using the underlying definition of the geometry primitive. Given a point on a straight-line segment in Figure 4-1 the closest point will always be along the normal between the point and the true surface. Once the projected point location is found, one can compute the normal. This operation is trivial and computationally efficient for most primitives. However, for

example, for an ellipse and generalized surfaces a search algorithm must be used to find the closest point on the true surface. The effect of the results from these projection algorithms are shown in Example 1 within Chapter 6; these are compared to the non-projected result. Here the points being projected are the integrations points along the approximated line segments.

4.2.1. Line and Plane

This is the most trivial case as no projections are generally needed for positions or normals. This is justified by considering that the output geometry approximation is made up of straight-line segments and triangles therefore they can already represent the exact underlying geometry of lines and planes. For completeness, consider a random point $\vec{p}$ which is projected to a point $\vec{p}^*$ on to a line segment between vertices $\overline{v_1}$ and $\overline{v_2}$ given by:

$$\vec{r} = \vec{p} - \overrightarrow{v_1} \tag{4-1}$$

$$\hat{t} = \frac{\overrightarrow{v_2} - \overrightarrow{v_1}}{\|\overrightarrow{v_2} - \overrightarrow{v_1}\|} \tag{4-2}$$

$$\vec{r}_t = (\vec{r} \cdot \hat{t})\hat{t} \tag{4-3}$$

$$\vec{p}^* = \overrightarrow{v_1} + \vec{r}_t \tag{4-4}$$

Similarly, a random point $\vec{p}$ can be projected onto a plane defined by the normal $\hat{n}$ and origin $\vec{o}$ as shown in Figure 4-2.

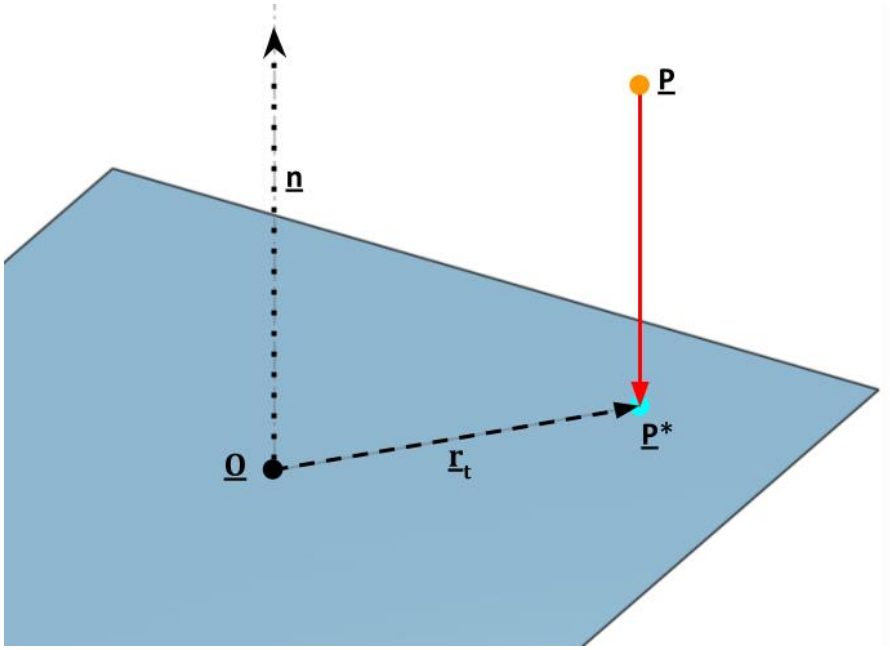

Figure 4-2. Exact surface projection algorithm for a plane

The projected point $\vec{p}^*$ can be found as:

$$\vec{r} = \vec{p} - \vec{o} \tag{4-5}$$

$$\vec{r}_n = (\vec{r} \cdot \hat{n})\hat{n} \tag{4-6}$$

$$\vec{r}_t = \vec{r} - \vec{r}_n \tag{4-7}$$

$$\vec{p}^* = \vec{o} + \vec{r}_t \tag{4-8}$$

Both operations are computationally insignificant as the projected values can be computed directly using the definition of the geometry. The normals are constant and given directly in the case of a plane's definition.

4.2.2. Circles and Spheres

Circles and spheres are defined by an origin $\vec{o}$ and radius R as shown in Figure 4-3. As can be seen for a random point $\vec{p}$ which is to be projected onto the true surface. The closest point will be along the normal, which is a vector from the origin to the point in question.

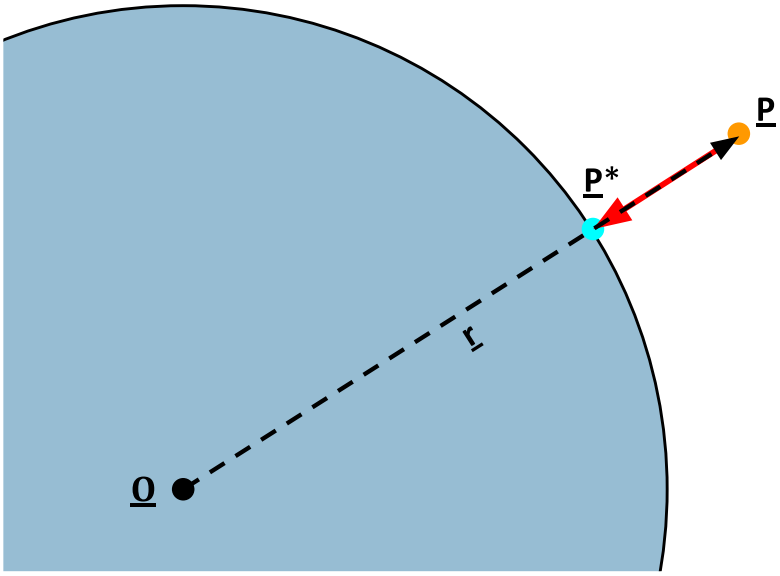

Figure 4-3. Exact surface projection algorithm for circles and spheres

This makes computing the normal to the surface for circles and spheres as simple as:

$$\vec{r} = \vec{p} - \vec{o} \tag{4-9}$$

$$\hat{n} = \frac{\vec{r}}{\|\vec{r}\|} \tag{4-10}$$

Then the closest point projection $\vec{p}^*$ can be found using the radius R:

$$\vec{p}^* = R\hat{n} \tag{4-11}$$

4.2.3. Ellipse

This is one of the most complicated primitives (aside from general surfaces), as finding the closest point is not a trivial computation. Instead, it requires the use of a search algorithm which in effect is a distance minimization. The convexity of the problem lends itself to the use of a minimization via a Newton-Raphson method; however, the use of the simple bisection method is much more effective [21]. Some CAD programs support ellipsoid primitives, which is the 3D version generalization of an ellipse. Similarly, this leads to a minimization problem where the bisection method still is

the most performant method [21]. Compared to other primitives, the ellipse is far more computationally expensive as it requires an iterative method. That said, using the bisection method for an ellipse, no more than four iterations are generally required for a satisfactory solution. More iterations would be needed for a hyper ellipsoid, but this primitive is not considered.

In 3D for an ellipse, the search algorithm becomes a minimization of the distance to the intersection of the surface formed by the union of an ellipsoid and plane defined by:

$$\frac{x^2}{a^2}+\frac{y^2}{b^2}+\frac{z^2}{c^2}=1 \tag{4-12}$$

$$xn_x+yn_y+zn_z=0 \tag{4-13}$$

More practically, the point of interest $\vec{p}$ can first be projected onto the plane of the ellipse $\hat{n}$ by using:

$$\vec{p}_p=\vec{p}-(\vec{p}\cdot\hat{n})\hat{n} \tag{4-14}$$

Then the problem can be made two-dimensional using the ellipse plane coordinate system (u,v). This is shown in Figure 4-4; it may be observed there is no simple analytical method to determine the projected point.

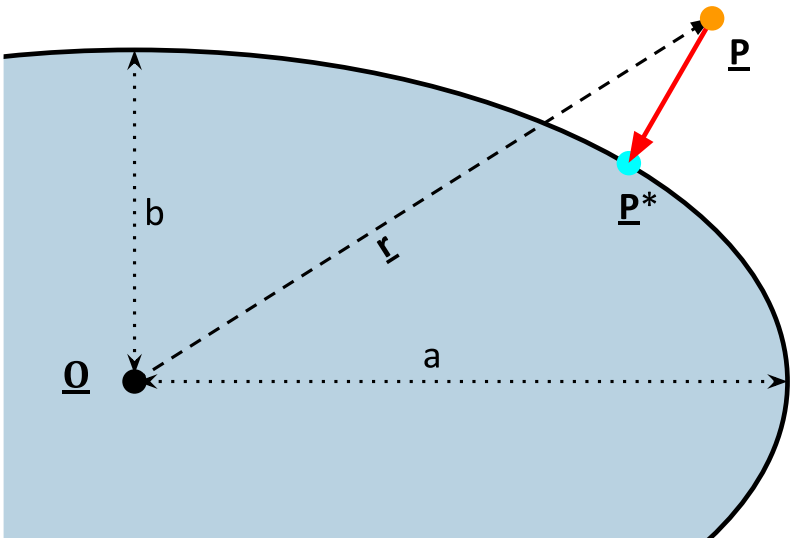

Figure 4-4. Exact surface projection algorithm for an ellipse

For the plane coordinate system, the minimization problem then becomes to find a value t which has the minimum distance to $\vec{p}_p$ in the coordinate system (u, v) from the ellipse surface:

$$u = \text{acos}(t) \quad v = bsin(t) \tag{4-15}$$

This can be readily solved via the bisection method and converted back to the global coordinate system. Extensive explanation and algorithmic approaches are covered in [21]. The normal at a point on an ellipse is defined explicitly following Equation (4-15) as:

$$\frac{ax}{\cos(t)} - \frac{by}{\sin(t)} = a^2 + b^2 \tag{4-16}$$

4.2.4. Cylinder

To project a random point $\vec{p}$ onto a cylinder which is defined by its origin $\vec{o}$, radius R, and axis $\hat{a}$ as shown in Figure 4-5.

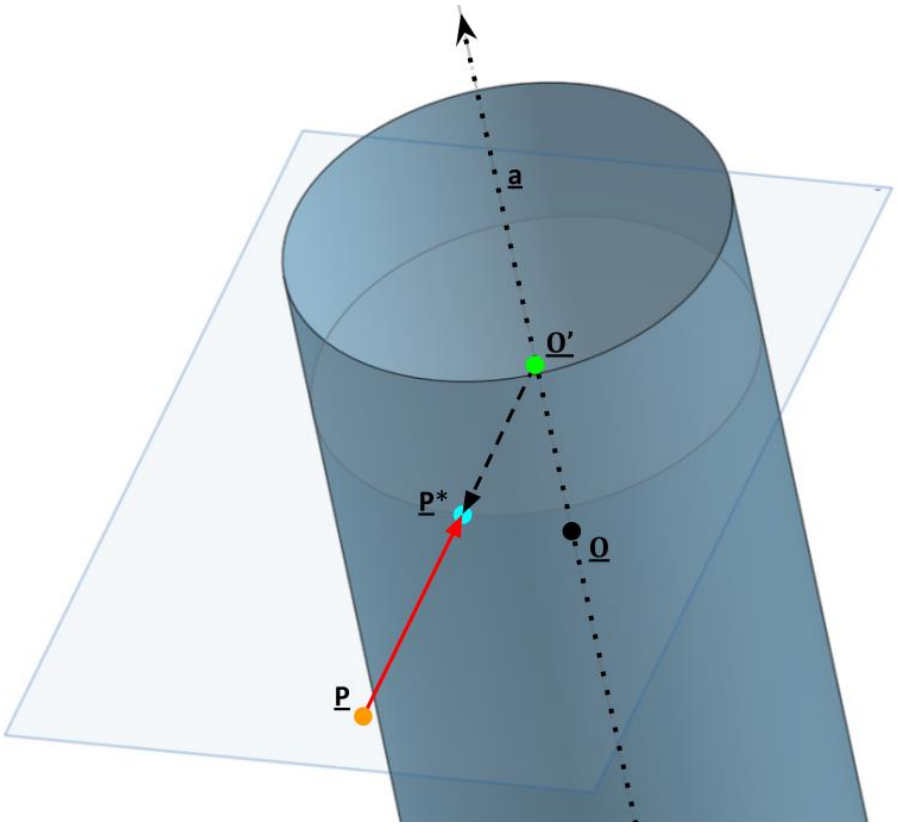

Figure 4-5. Exact surface projection algorithm for a cylinder

The projected point $\vec{p}^*$ can be found from geometric construction as:

$$\vec{r} = \vec{p} - \vec{o} \tag{4-17}$$

$$\vec{o}' = \vec{o} + \underbrace{(\vec{r} \cdot \hat{a})\hat{a}}_{\text{Length Along Axis}} \tag{4-18}$$

$$\vec{p}^* = \vec{o}' + \frac{\vec{p} - \vec{o}'}{\|\vec{p} - \vec{o}'\|} R \tag{4-19}$$

This gives the normal at the point $\vec{p}$ on the cylinder as:

$$\hat{n} = \frac{\vec{p} - \vec{o}'}{\|\vec{p} - \vec{o}'\|} \tag{4-20}$$

4.2.5. Cone

A cone can be defined by its origin $\vec{o}$, axis $\vec{a}$, and half-angle θ. Though not intuitive, many underlying geometry engines use this representation along with a radius R to define cylinders, the main one being ACIS which is the engine used for many

common CAD applications [22]. A diagram of a projection onto a cone is shown in Figure 4-6.

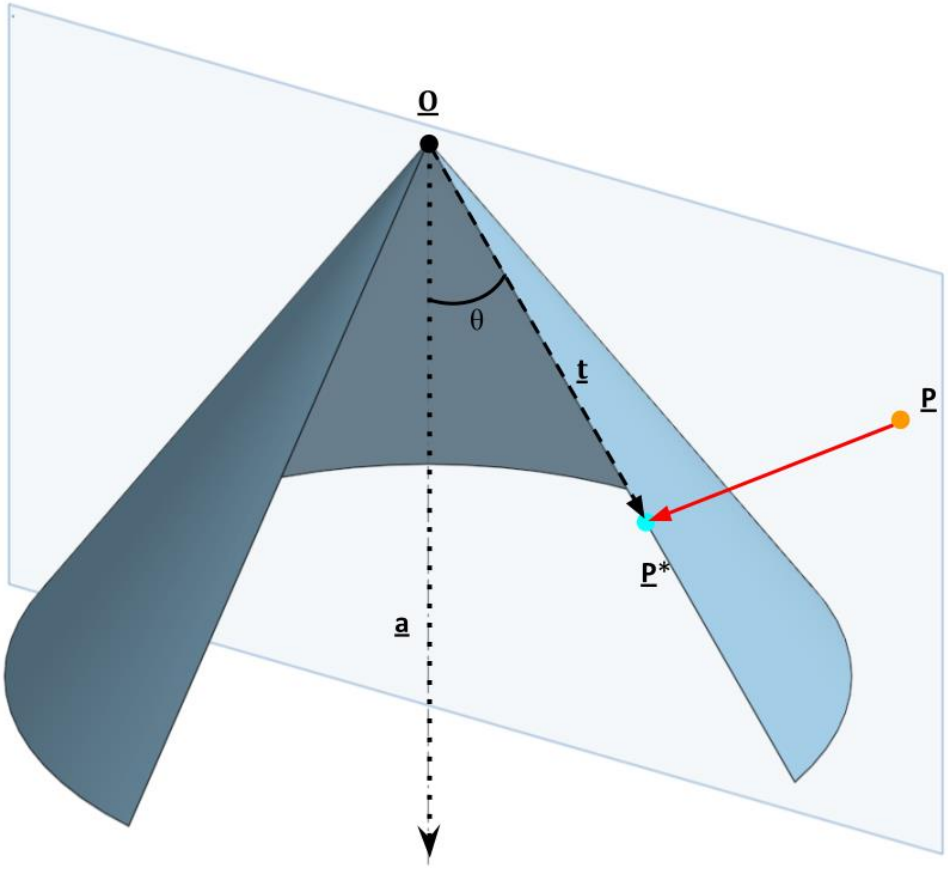

Figure 4-6. Exact surface projection algorithm for a cone

If one is to project a point $\vec{p}$ onto the cone surface a local plane $\hat{m}$ can first be defined as:

$$\hat{m} = \vec{a} \times (\vec{p} - \vec{o}) \tag{4-21}$$

The plane $\hat{m}$ is represented in Figure 4-6 as the blue rectangle. Knowing the half-angle θ, the axis $\vec{a}$ can then be rotated about $\hat{m}$ to give a vector $\hat{t}$ which is along the cone using Rodrigues' rotation formula [23]:

$$\hat{t} = \vec{a}\cos(\theta) + (\hat{m} \times \hat{a})\sin(\theta) + \hat{m}(\hat{m} \cdot \hat{a})(1 - \cos(\theta)) \tag{4-22}$$

The line $\hat{t}$ is the intersection of the plane $\hat{m}$ and cone surface closest to point $\vec{p}$. Finally, knowing the direction $\hat{t}$ the projected point $\vec{p}^*$ which is on the cone surface is computed as:

$$\vec{p}^* = [(\vec{p} - \vec{o}) \cdot \hat{t}]\hat{t} + \vec{o} \tag{4-23}$$

The normal of the cone in this plane can be found by considering the geometry as:

$$\hat{n} = \hat{m} \times \hat{t} \tag{4-24}$$

4.2.6. Torus

The torus turns up quite often in parts when you consider features such as fillets (radius on edge). A circular torus is defined with a major radius R and a minor radius r. At the center of the torus is its origin $\vec{o}$ with the torus orientation defined by an axis $\vec{a}$ this is shown in Figure 4-7 [23]. The projection can be made from geometric construction alone, which consists of identifying the intersection plane (shown in blue), then finding a vector from the center of the outer torus loop to the point to be projected. Once the plane is identified, the problem reduces to one alike the projection of a circle.

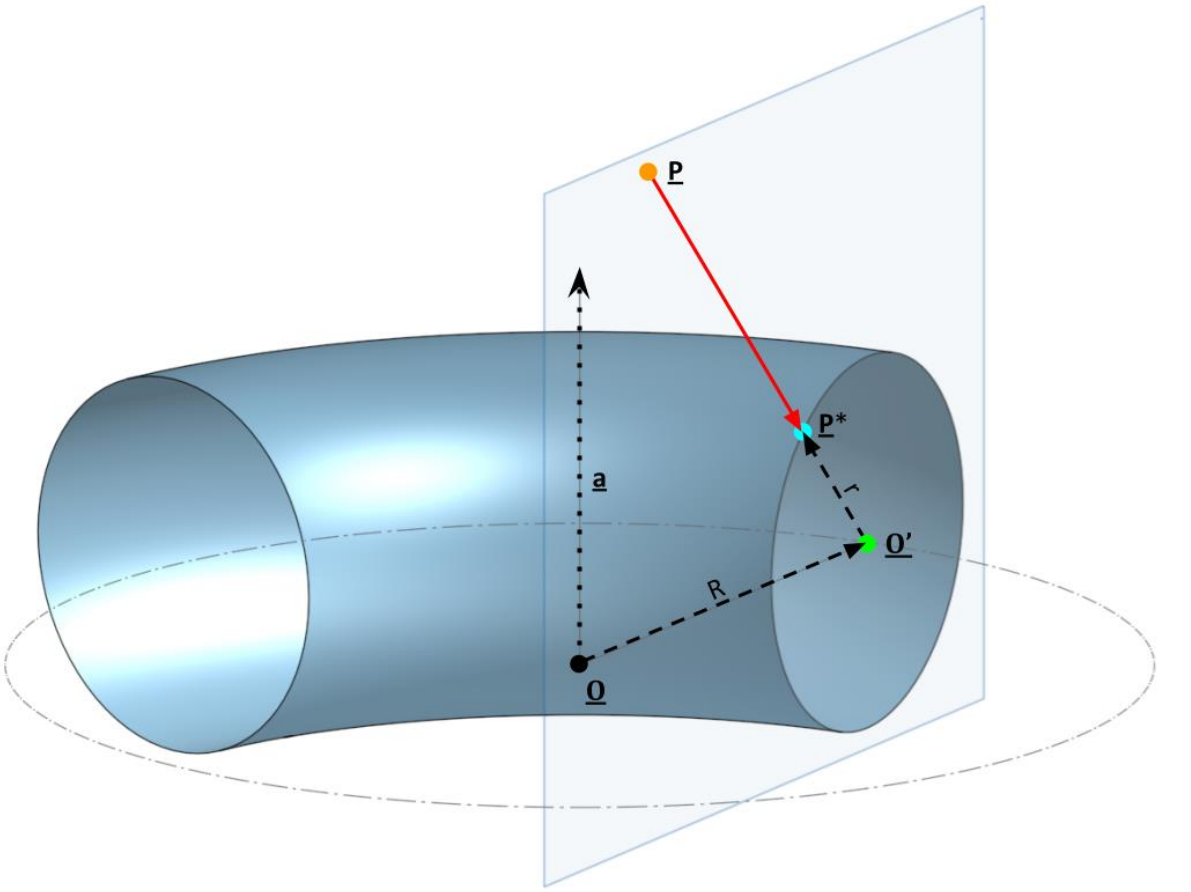

Figure 4-7. Exact surface projection algorithm for a torus.

Alike the cone first, the plane $\hat{m}$ is determined as:

$$\hat{m} = \vec{a} \times (\vec{p} - \vec{o}) \tag{4-25}$$

Within the plane defined by $\hat{m}$, $\hat{t}$ is the direction from the torus origin to the center of its ring defined as:

$$\hat{t} = \hat{m} \times \hat{a} \tag{4-26}$$

An additional origin $\vec{o}'$ is introduced, which is at the center of the circle closest to $\vec{p}$ formed by the intersection of the torus and plane $\hat{m}$. $\vec{o}'$ is defined as:

$$\vec{o}' = \vec{o} + R\hat{t} \tag{4-27}$$

This reduces similarly to projecting a point onto a circle. The normal of the torus at the point to be projected is given as:

$$\hat{n} = \frac{\vec{p} - \vec{o}'}{\|\vec{p} - \vec{o}'\|} \tag{4-28}$$

Making the projected point $\vec{p}^*$ equal to

$$\vec{p}^* = \vec{o}' + r\hat{n} \tag{4-29}$$

While a seemly daunting primitive, the projection on a torus can be computed extremely efficiently; however, for a general elliptical torus, an iterative method would have to be used, as previously discussed for ellipses. Most CAD programs do not use an elliptical torus to represent geometry.

4.2.7. Verifying Projection Methods

The preceding projection methods were tested using various geometry made within the CAD application OnShape. These parts where imported with their tessellated faces and underlying surface definitions. Then at each vertex of the tessellated triangles, which is guaranteed to be on the actual surface, the point is offset by a small distance along its normal. This new point is then projected using the algorithm developed for the given surface, the expected result is for it to return the original vertex. This was used to test all the projection algorithms resulting in only floating-point numerical error between the projected result and the original vertex. The costliest algorithm is the ellipse since it requires an iterative method, however, often only a maximum of four iterations where needed to find the desired closest point. The other surface projection algorithms have no significant computational cost given they are done via direct computation from geometric a construction.

4.2.8. General Curves & Surfaces

General surface representations can differ between different CAD programs. However, most of these are represented by a function of one or two variables; this is

known as a parametric space. Thus, a distance minimization can be used to find the closest point on a given surface to a given point. This is computationally expensive, and with more advanced surfaces comes the possibility of finding a local minimum. But this is often an insignificant issue as the point in question is in the vicinity of the surface; therefore, a good initial guess can be made. Computing the normal to a general surface also varies depending on the underlying representation. If you consider a point you want to project $\vec{p}$ onto an arbitrary boundary $\partial\mathcal{B}$ you are seeking a point $\vec{p}^*$ on the boundary which is closest to $\vec{p}$. This can be represented as a minimization problem of the form:

$$minimize \quad \{ \parallel \vec{p}^* - \vec{p} \parallel \} \quad \vec{p}^* \in \partial\mathcal{B} \tag{4-30}$$

$$\vec{p}^* = \vec{p}^*(s,t) \tag{4-31}$$

Newton iterations can be used to solve for the point $\vec{p}^*$ based on its parametric definition normally represented by the coordinates (s,t) [23]. To determine an initial guess, a random sampling can be made. However, the possibility of finding a local minimum depends on how far the point to be projected $\vec{p}^*$ is away from the surface.

4.2.9. Application to FEM

Figure 4-1 shows the geometry representation that most FEM software use to represent a curved boundary. This can lead to inaccuracy in both volume and surface integrations. This is amplified by problems where the exact geometry becomes critical to the solution structure, as is the case with contact. Once all primitives (curves and surfaces) are defined for a part, the projected point and exact surface normal can be computed for any given point. These projections are applied to surface integrals, which are computed via numerical integrations of lines or triangles that make up the boundary. The integration points within these lines (or triangles for 3D) can be projected onto their

closest true surface, and their true normal computed. However, there remains the issue of inaccurate stiffness due to the approximation of the true part geometry. The stiffness in the IBFEM method is computed using the volume of each element that is inside of the part. Currently, this is accomplished by splitting this region into triangles (or tetrahedrons for 3D) and performing numerical integration. In this case, a projection of integration points doesn't make sense as they are embedded within the surface. In short, only surface integrals can benefit from this projection. Further work could be made to use the exact representation of surfaces to improve the accuracy of volume integrations.

CHAPTER 5
5. MODELING CONTACT WITHIN IBFEM

Now contact between two parts is considered. Both parts have their own underlying mesh (or grid), as shown in Figure 5-1. In the potential contact region, these meshes overlap to form contact elements. Thus, each contact element can be thought of as an element that includes the nodes and displacements of both overlapping elements.

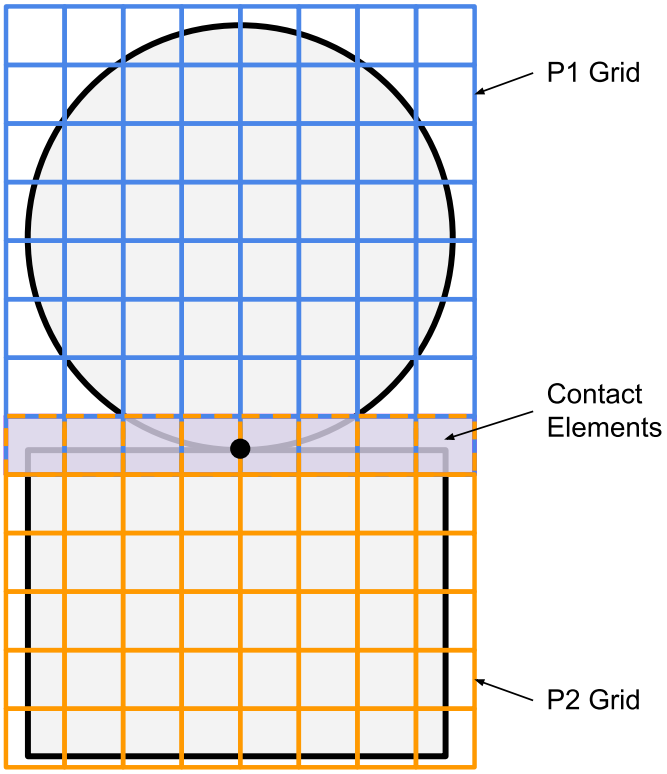

Figure 5-1. Underlying grids for each part in a contact problem. Which are connected by the overlapping elements known as contact elements. The contact point in this example is shown by the black dot.

It is noted that there is no condition that the overlapping meshes move or deform continuously at the nodes; rather, both overlapping elements will take on different displacements for each of their respective nodes. The displacements can be written like

Equation (3-1), but now each part's element has its own displacement approximation as:

$$\{u^{h1}\} = [N]\{X_e^{g1}\} \qquad \{u^{h2}\} = [N]\{X_e^{g2}\} \tag{5-1}$$

Where u^{h1} and u^{h2} are analogous to the traditional FEM element shape function displacement approximations. The contact elements are regions where potential contact can occur between the two parts. If no contact is occurring within a particular contact element, its contribution is zero to both the assembled stiffness and delta force.

5.1. Contact Solution Structure

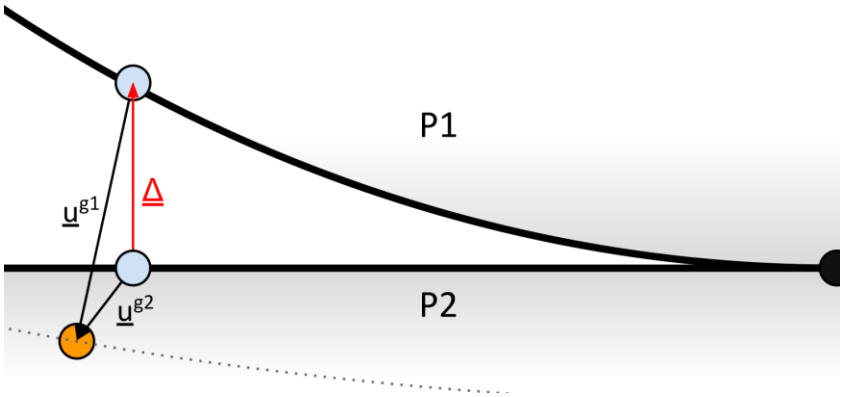

Figure 5-2. Compatibility condition for contact. Consider two points that come into contact due originally separated by a displacement Δ_i.

Consider two points that come into contact, as shown in Figure 5-2. A vector Δ can be drawn between the original position of the two points. If the two points are in contact, then their final position x_i^{g1} and x_i^{g2} must be equal. Which leads to the condition shown in Equation (5-3), requiring the difference in the displacement of the two points on the surface which come into contact should be equal to the original gap between them.

$$\Delta_i \equiv X_i^{g1} - X_i^{g2} \tag{5-2}$$

$$\Delta_i = u_i^{g2} - x_i^{g2} - u_i^{g1} + x_i^{g1} = u_i^{g2} - u_i^{g1} \tag{5-3}$$

To enforce this contact between the two grids, the following solution structure is applied to the contact elements.

$$\{u\} = [H]\{u^{h1}\} + [I - H]\{u^{h2}\} + [H]\{\Delta\} \tag{5-4}$$

$$\{u\} = [H][N]\{X_e^{g1}\} + [I - H][N]\{X_e^{g2}\} + [H]\{\Delta\} \tag{5-5}$$

This structure for contact was first identified in [5] where the requirement of Δ was found to ensure that the parts come into contact. Without Δ, there is no enforcement that the two points will come into contact, and any deformation that occurs would just maintain that gap. Applying the principle of virtual work defined in Equation (3-13) to this new contact solution structure results in:

$$\sum_{e=1}^{NE} \int_{\mathcal{B}} \delta\varepsilon^T \sigma \, dV = \sum_{e=1}^{NE} \int_{\partial\mathcal{B}} \delta u^T t \, dS + \sum_{e=1}^{NE} \int_{\mathcal{B}} \delta u^T b \, dV \tag{5-6}$$

$$\sum_{e=1}^{NE} \{\delta X_e\}^T \left(\underbrace{\int_{\mathcal{B}} [\bar{B}]^T [C][\bar{B}] dV}_{\text{Element Stiffness } [\mathrm{K_e}]} \{X_e\} + \underbrace{\int_{\partial\mathcal{B}} [\bar{B}]^T [C][\partial H]\{\Delta\} \, dS}_{Delta\ Force\ \{F_\Delta\}} \right) = \sum_{e=1}^{NE} \{\delta X_e\}^T \underbrace{\int_{\partial\mathcal{B}} [\bar{N}]^T t \, dS}_{\text{Applied Traction } \{\mathrm{F_t}\}} + \sum_{e=1}^{NE} \{\delta X_e\}^T \underbrace{\int_{\mathcal{B}} [\bar{N}]^T b \, dV}_{\text{Body Forces } \{\mathrm{F_b}\}} \tag{5-7}$$

$$\underbrace{\sum_{e=1}^{NE} \{\delta X_e\}^T [K_e]\{X_e\}}_{\text{Element Stiffness } (LHS)} = \underbrace{\sum_{e=1}^{NE} \{\delta X_e\}^T (\{\mathrm{F_t}\} + \{\mathrm{F_b}\} - \{F_\Delta\})}_{\text{Element Force (RHS)}} \tag{5-8}$$

Where $\{\mathrm{F_t}\}$ are externally applied tractions and $\{\mathrm{F_b}\}$ is the body force. The delta force $\{F_\Delta\}$ is included into the final assembly RHS as shown in Equation (5-8). Conceptually $\{F_\Delta\}$ can be thought of the force required to compress extra stiffness at the contact boundary to enforce two points coming together. For example, for a 2d plane

stress/strain problem with four-node elements $\{F_\Delta\}$ would take the form for each element as:

$$\{F_\Delta\} = \int_{\partial\mathcal{B}} \underbrace{[\bar{B}]^T}_{16x3}\ \underbrace{[C]}_{3x3}\ \underbrace{[\partial H]}_{3x2}\ \underbrace{\{\Delta\}}_{2x1}\ dS \tag{5-9}$$

5.2. Contact Area Representation

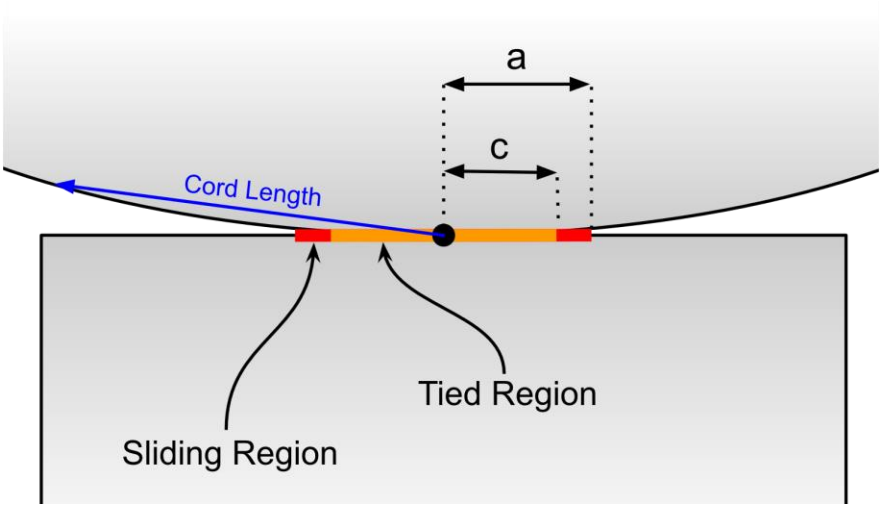

Figure 5-3. Sliding and tied region of a contact area. Measured by half-widths a and c which represent the entire region and tied region. A example cord length is shown measuring from the contact point to an arbitrary point on the boundary.

From Hertzian contact theory, there are two scalar lengths to consider in 2D point contact the tied half-width c and total contact half-width a shown in Figure 5-3. Where the contact ratio $\frac{c}{a}$ is given by Equation (2-29) and depends on the ratio of contact forces transferred through the contact region and the coefficient of friction. From Hertzian theory, we expect that a will depend only on normal force transferred through the contact. Within IBFEM, contact width a is incremented with each Newton iteration to determine the correct contact width. One can also consider the sliding region length b defined as:

$$a = b + c \tag{5-10}$$

As the tangential force applied through the contact region increases, so does the sliding region. When enough tangential force is applied to make the entire region slide, the problem is no longer partial-slip but instead a gross-slipping problem. In this case, the entire contact region will have a relative displacement. To determine if a particular point on the part boundary is within the tied or sliding region, the cord length from the contact point to the point on the boundary is used as shown in Figure 5-3 and compared to the length of a or c. The use of the cord length is an approximation for curved surfaces, while it is exact for a flat line. The cord length used is also based on the original undeformed geometry and not the updated, which is a further approximation but in line with small-displacement theory. The use of projecting points is crucial here for determining the correct displacement between two points that come into contact. For small contact regions, it can be observed the cord approaches the value of the arclength. This can be seen in Figure 5-3 by considering the difference in cord vs. arc length of the region in contact, represented by the red and orange bar.

5.3. Non-Linear Automatic Solution

Consider the Equation (2-23) if the contact load is known a priori, the contact width could be simply computed. However, if the contact load is not known, such as the case with a displacement boundary condition an iterative solution must be used. If you consider the Hertz problem cases shown in Figure 2-2, the vertical displacement is not linearly proportional to the normal contact force. Even if a force boundary condition is used, the problem remains inherently non-linear as the contact width is not linearly proportional to the normal contact force. Thus, solving contact problems even with small-strain theory requires a Newton-Raphson iterative solution. Here the global

stiffness matrix $[K]$ is used as the tangent stiffness matrix for each step, but only the contact stiffness $[K_c]$ contribution will change. Between iterations only the contact widths a and c will change which effects only the stiffness and delta force within the contact elements $[K_c]$.

The general form for automatic solution of non-linear finite element equations is given by [24] as:

$$[K]_{i-1}^{t}\{\Delta U\}_i = \{R\}^t - \{F\}_{i-1}^{t} \tag{5-11}$$

Where $[K]_{i-1}^{t}$ is the tangent stiffness matrix for the current load step t at the current iteration i. The value $\{R\}^t$ is the external load at the current load step. $\{F\}_{i-1}^{t}$ is the internal force and $\{\Delta U\}_i$ is the displacement vector which is solved for in each iteration. The solution procedure can be thought of as two nested loops, one which increases the externally applied load (load step), and the other which finds the correct solution for a given load step. A correct solution is obtained when $\{\Delta U\}_i$ is driven too zero, or rather the internal force correctly balances the externally applied load. The difference in these loads $\{R\}^t - \{F\}_{i-1}^{t}$ is known as the residual.

The externally applied load $\{R\}^t$ is the result of implicit and explicit boundary conditions applied to the model. While $\{F\}_{i-1}^{t}$ is the internal force which is the sum reactions of all the elements and the contact forces including any friction interactions. The final solution $\{U\}_i$ is updated each iteration as:

$$\{U\}_i^t = \{U\}_{i-1}^{t} + \{\Delta U\}_i^t \tag{5-12}$$

In each load step, the externally applied load is increased. If the load applied is linear, the externally applied load is equal to:

$$\{R\}^t = \lambda^t\{R\} \tag{5-13}$$

Where $\{R\}$ is the total externally applied load. Multiple schemes have been proposed for updating λ between load steps. The simplest is a fixed step method which simply increments λ by a fixed amount until $\lambda = 1$. One alternative method is the constant work approach which uses the solution $\{\Delta U\}_i^t$ to help determine how much to increment λ by; this constant work approach is explained in [5] Convergence must be achieved at each load step; this point is determined by the convergence criteria. This criterion must incorporate both the displacements and the residual load. To this effect, a tolerance based on the ratio of the residual work done has been proposed as:

$$\frac{\{\Delta U\}_i^t(\lambda_i^t\{R\} - \{F\}_i^t)}{\{\Delta U\}_i^r(\lambda_i^r\{R\} - \{F\}_i^r)} \leq TOL \tag{5-14}$$

The numerator is the current iteration's residual work done, while the numerator is the reference residual work. The reference is initially the first computed value, after that point, the reference is updated after each iteration if $\{\Delta U\}_i^t(\lambda_i^t\{R\} - \{F\}_i^t > \{\Delta U\}_i^r(\lambda_i^r\{R\} - \{F\}_i^r)$. For results in the present work, a tolerance over 10^{-10} was always used.

The tangent stiffness matrix $[K]_i^t$ is approximated as the stiffness matrix of the analysis for a Full Newton-Raphson iteration scheme with this matrix being updated each iteration. This is compared to the modified Full Newton-Raphson scheme, which only updates the tangent stiffness matrix after each step. For the present analysis, the Full Newton-Raphson method was always used; this is due primarily to the constantly changing contact stiffness $[K_c]$ which depends on the contact width. Thus in order to achieve convergence within a particular load step, this stiffness must constantly be updated to allow for a correct search of penetration and tension points. Further work to identify a better tangent stiffness matrix for the changing contact stiffness may increase convergence speed and accuracy.

5.4. Frictional Contact

Determining the contact width ratio can be done using the analytical result from Equations (2-29) and (2-30) by knowing the net contact force ratio being transferred through the contact region. To determine this ratio, the net forces transferred through the contact elements must be computed relative to the contact direction. The contact direction is simply the normal vector at the contact point. In other words, the normal force and tangential force for the contact must be computed, and thus the ratio determined. Consider a single contact element's assembly as:

$$[k_c]\{x_e\} = \{f\} + \{\Delta f\} \tag{5-15}$$

$$\{f\} = [k_c]\{x_e\} - \{\Delta f\} \tag{5-16}$$

Where the external load is split into $\{f\}$ and the delta force $\{\Delta f\}$ which have approximate relative magnitudes of $\Delta f \approx 10^{11},\ f \approx 10^{8}$ this large magnitude difference leads to numerical error, making the value $\{f\}$ unrecoverable and thus, Equation (5-16) is not valid. This load $\{f\}$ summed across the contact elements yields the net load transferred through the contact. In order to compute $\{f\}$ the solution must be found neglecting the contribution from $\{\Delta f\}$ to accomplish this the modified solution $\{\bar{X}\}$ must be found via:

$$\{K_C + K_E\}\{\bar{X}\} = \{F\} \tag{5-17}$$

Where $\{F\}$ no longer contains any contribution from the delta force. Which can be assembled into the individual element displacements $\{\overline{x_e}\}$. This value is used to find the elements' net force due to the contact and is found from:

$$\{f\} = [k_c]\{\overline{x_e}\} \tag{5-18}$$

These are summed to find the net contact force as:

$$\{F_{contact}\} = \sum_{i=0}^{NCE} [k_c]_i \{\overline{x_e}\}_i \tag{5-19}$$

However, $\{F_{contact}\}$ will be in terms of global coordinates; this must be converted to the local contact direction by using the normal of the contact point. This yields the normal and tangential forces transferred through the contact region. The ratio β of these defined in Equation (2-27) yields the contact width ratio $\frac{c}{a}$ knowing the coefficient of friction.

5.4.1. Tied Formulation

Within the tied region, the contact is considered bonded, which is enforced by the contact solution Equation (5-4). Within this region, the boundaries of the parts in contact are enforced to stay together, no matter the direction. Applying the same treatment from the fully fixed essential boundary condition, H_{ij} is constructed as:

$$H_{ij}^L = \begin{bmatrix} \mathrm{H}(\phi) & \\ & \mathrm{H}(\phi) \end{bmatrix} \rightarrow \quad H_{ij} = R_{ji} H_{ij}^L R_{ij} = H_{ij}^L \tag{5-20}$$

$$[\partial H] = \begin{bmatrix} \frac{\partial H_{11}}{\partial x} & \\ & \frac{\partial H_{22}}{\partial y} \\ \frac{\partial H_{11}}{\partial y} & \frac{\partial H_{22}}{\partial x} \end{bmatrix} \tag{5-21}$$

Within a region defined as tied the friction coefficient can be thought of as infinite since a bonded contact will always be enforced. For a partial slip problem, there is a known tied region that doesn't slip; in this region, the shear force transferred is not limited by the maximum friction force. So, the use of this tied assumption for this region correctly maintains the required tangential force transfer within this region.

5.4.2. Sliding Formulation

In the sliding region, the shear stress due to friction is limited by the definition of friction: $\tau = \mu\sigma_{\mathrm{n}}$. Therefore, a partial slip region develops, this is because friction between the parts is not sufficient to keep them tied within this region.

$$H_{ij}^{L} = \begin{bmatrix} 1 & \\ & \mathrm{H}(\phi) \end{bmatrix} \rightarrow \quad H_{ij} = R_{ji} H_{ij}^{L} R_{ij} \tag{5-22}$$

$$[\partial H] = \begin{bmatrix} \dfrac{\partial H_{11}}{\partial x} & \dfrac{\partial H_{12}}{\partial x} \\ \dfrac{\partial H_{21}}{\partial y} & \dfrac{\partial H_{22}}{\partial y} \\ \dfrac{\partial H_{11}}{\partial y} + \dfrac{\partial H_{21}}{\partial x} & \dfrac{\partial H_{22}}{\partial x} + \dfrac{\partial H_{12}}{\partial y} \end{bmatrix} \tag{5-23}$$

By allowing the local tangential direction to slide, the contact is now only bonded in the normal direction between the parts. If frictionless contact is considered, the entire region will use the sliding formulation and thus be restricted only to not penetrate each other while still allowing relative sliding. An example of frictionless contact is given in Chapter 6. If the friction coefficient is non-zero, an internal force between the bodies will occur; thus, a frictional force must be added as:

$$\{\mathrm{F_f}\} = \sum_{i=0}^{NCE} \int_{\partial\mathcal{B}} [\overline{N}]^T \vec{t}\, dS = \sum_{i=0}^{NCE} \int_{\partial\mathcal{B}} [\overline{N}]^T \{\hat{n}_t\}\, \sigma_n \mu\, dS \qquad \sigma_n = \hat{n}\sigma\hat{n} \tag{5-24}$$

In the present project, this extra friction force within the sliding region is neglected, relying on the tied region to enforce the required tangential force between the parts in partial-slip contact. This assumption was made to eliminate numerical issues found while computing the additional force $\{\mathrm{F_f}\}$.

5.5. Contact Width Growth

Since the contact width is not known a priori, an iterative method that works with the non-linear solver is used to find the correct contact width. For contact, there are two

required conditions: 1) no penetration between the parts and 2) no tensile stress between two regions in contact. The first is common among all contact problems, but the second assumes that the contact is completely non-adhesive. In reality, there will exist van der Waals forces between the surfaces in contact, which allows some tensile stress between the contact. This is known as adhesive contact [25] and it is not represented in the present work or within Hertzian theory.

Within each contact element, there is potential for the boundary to be in tied, relative sliding, or not in contact. Using the cord length from the contact point these boundaries can be identified within each contact element. The no contact region becomes important for detecting penetration. With this formulation, for each point on the boundary of $P1$ there is a constant matching point on the boundary of $P2$ based on the cord length. The difference between these points equal to $\vec{\Delta}$. When partial slip is considered, there is a relative displacement within the sliding region between two points that originally came into contact. This relative sliding is allowed by the formulation of $[H]$, which enforces $\vec{\Delta}$ only in the normal direction. The use of the cord length approximates the arc length as such for progressively larger deformations; this assumption becomes less and less accurate. It is assumed that for small displacements and thus small contact regions, the difference is negligible.

5.5.1. Enforcing No Penetration

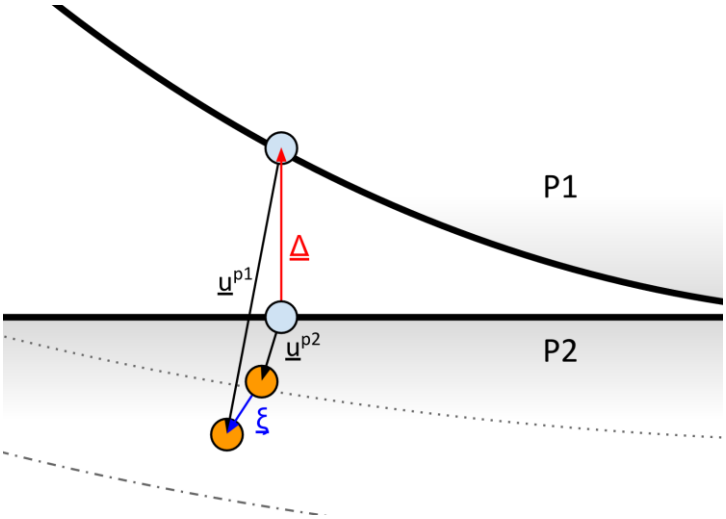

Figure 5-4. Determination if a point on Part 1 is penetrating Part 2.

If two regions are considered in contact, Equation (5-4) enforces in this region that there is no penetration between the two parts. However, consider that the contact width a has been underestimated. In this case the contact forces are still being fully transmitted through the region, but penetration will occur between the two parts outside of the known contact region. Of course, penetration is a violation of the contact conditions meaning the contact width needs to be increased. To detect this penetration within the contact elements, the no-contact region is searched to find points that penetrate between the two parts. This search is performed following an iteration of the non-linear solution structure. Each penetrated point found increments a penetration counter. To find if two points are penetrating each other, consider Figure 5-4 and the displacement between the two points that can come into contact $\vec{\xi}$. This gives a penetration condition when:

$$\vec{\xi} \cdot \vec{\Delta} < 0 \tag{5-25}$$

This is to say that if the displacement between the two points $\vec{\xi}$ are in the same direction as $\vec{\Delta}$ there is no penetration.

5.5.2. Enforcing No Tensile Stress

There also exists the problem of overestimating the contact width, which affects the final force distribution through the contact, and produces unrealistic results. To detect if the contact width is overestimated, a search for normal tensile forces is performed within the contact region. If normal tensile stress is found between the parts (positive), this is an indication that these points want to pull apart from each other, thus a need for reducing the overall contact width. The normal stress is computed along the boundary as:

$$\sigma_n = \vec{n} \cdot \sigma \cdot \vec{n} \tag{5-26}$$

For any points within the contact region where tensile normal stresses are found, a tension point counter is incremented. Unlike penetration, which is based on displacement alone, the search for tension points depends on the secondary quantity of normal stress. This means that during iterations, when the correct solution is still unknown fictitious tensile points can occur.

5.5.3. Incrementing the Contact Width

An initial contact width increment is selected relative to the size of the mesh elements. This increment is reduced in the event of oscillations while iterating the contact width, this allows each iteration to take progressively smaller steps once a value close to the contact width is achieved. After each iteration, both the penetration and tensile stresses are checked within their respective regions. Resulting in a count of detected penetration points and detected tension points. These counts are then used to determine how the contact width should be updated. If no tensile or penetration points

are found, the contact width isn't updated. If there are only tensile points, the contact is decreased; similarly, if only penetrations points are found, the contact width is incremented. If both tensile and penetrations points are detected, the width is incremented by a smaller amount using the larger count to determine whether the contact half-width a should be incremented or decremented. Logically there should only ever be tension or penetrations points, but due to numerical error and uncertainty in the answer between steps, often some tension points might be found. However, penetration which is based on displacement is the driving force of change in the contact width, which is expected as the load is increased each step. Thus, the tension points can be thought of more as preventing overshooting in the solution for the half-width a.

5.5.4. Determining the Width Increment

The amount the half-width a is incremented and decremented is crucial to the convergence of the problem. Consider an increment Δa which is used to update the half-width a each iteration. If the increment is too small (i.e., less than 4% of the final half-width), the solution time increases since more iterations are required; these extra iterations occur just due to the limited size of Δa as they must each increment a to eventually find the correct value. The opposite problem is to pick a value of Δa, which is too large; this can cause constant oscillations between incrementing a or decrementing a. To alleviate these issues, Δa is updated each iteration based on multiple criteria. The most important is detecting oscillations while converging to a solution; this means the half-width a goes back and forth, increasing and decreasing, unable to reach the correct contact width. This can be detected by monitoring the sign of Δa between iterations and whenever there is a switch decreasing the magnitude of Δa by a set factor η as:

$$\Delta a \ = \eta \Delta a \tag{5-27}$$

For the present analysis, a factor of $\eta = 0.5$ is used. The smaller increment Δa progressively cuts out oscillations by allowing it to find a solution that would otherwise be forever skipped back and forth over. In other cases, an increase of Δa can reduce the number of iterations needed. To this effect, when only penetration points are detected Δa is increased by a factor of $\eta = 1.05$. This allows the contact half-width a to *jump faster toward* the correct solution. At the start of each load step, the contact width increment Δa is reset back to its initial value. This initial value is determined by the initial size of the mesh used. If a sufficiently small increment value Δa is used, then there is no need to update Δa; however, this comes at the expense of extremely slow convergence and is not practical. Likewise, the opposite issue of having a set value of Δa that is too large limits the possible accuracy and can prevent convergence.

CHAPTER 6
6. RESULTS

6.1. Effect of Projected Geometry on an Ellipse in Contact

This example examines the effects and needs for the projection algorithm introduced in Chapter 4. Here a half-ellipse on a block under point contact is analyzed as shown in Figure 6-1; a vertical displacement of $-0.1mm$ is specified on the top of the half-ellipse, while the bottom boundary is specified to be fixed reactions. Both parts are elastically similar, with a Young's modulus of $2 * 10^{11}$ Pa and Poisson's ratio of 0.3.

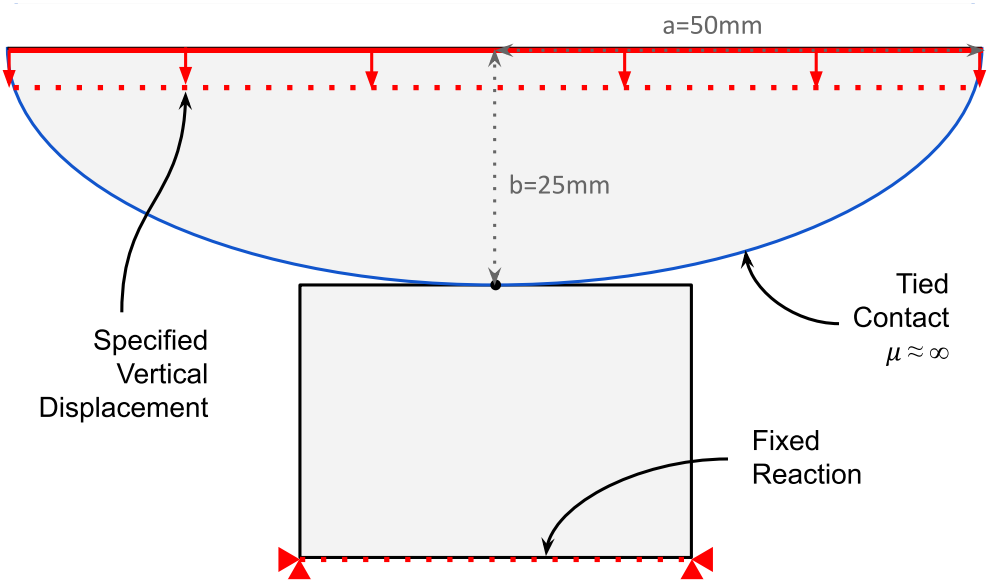

Figure 6-1. Boundary conditions for ellipse on plane contact.

The need for geometric accuracy for surface integration became very apparent while including contact analysis within IBFEM. While geometry with small inaccuracies will often still converge to a result, these results are considerably worse and do not match the analytical solution. Consider the Von Mises stress results shown in Figure 6-2, where (a) integration points are projected on accurate geometry (projected results) and (b) is the result without projection of integration points on accurate geometry (non-projected results). In (b), one can identify a lack of symmetry and large stress risers on

the contact surface. Iterations also took significantly longer for the non-projected result suggesting numerical issues from the approximate surface.

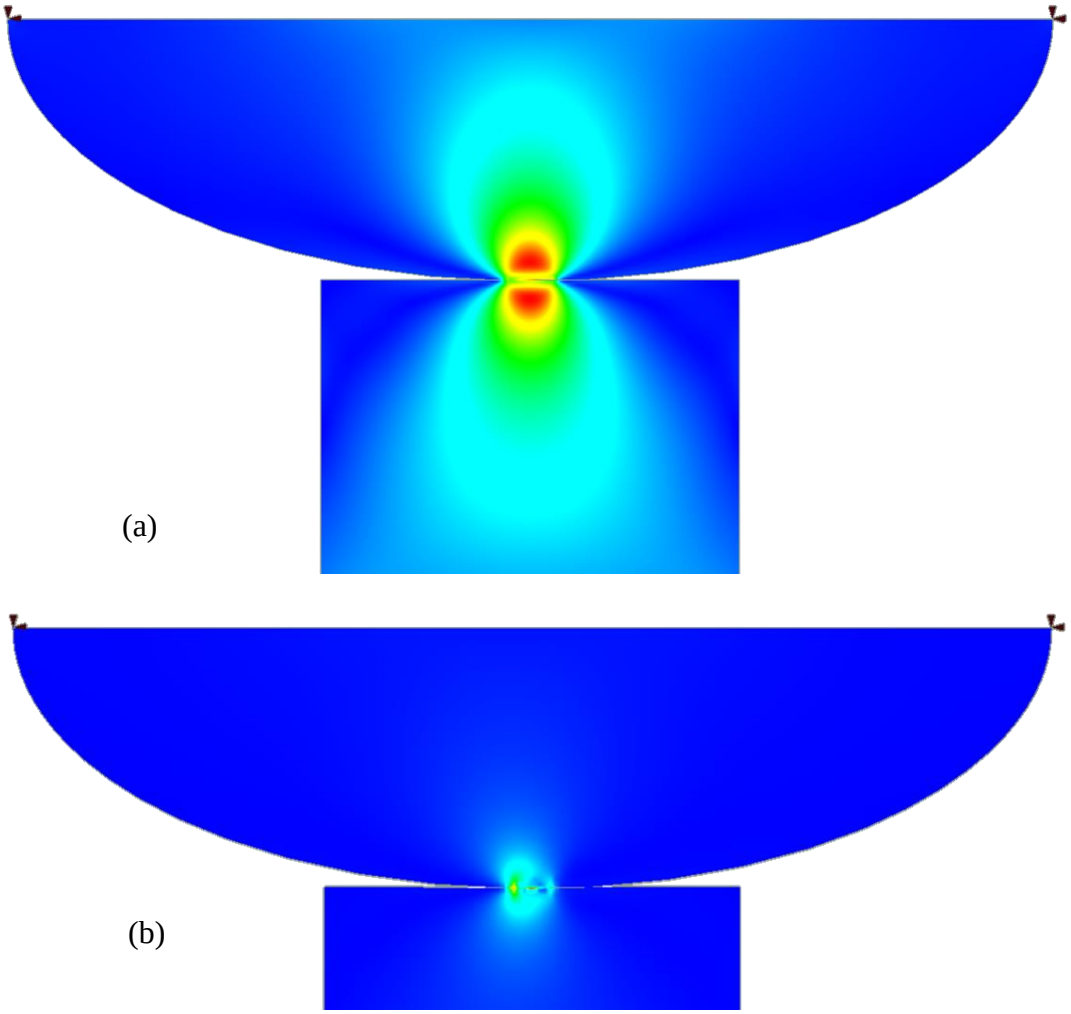

Figure 6-2. Comparison of the Von Mises stress plot between (a) projected and (b) non-project results. The only difference between simulations and results is the addition of the ellipse projection algorithm.

6.1.1. Comparison of Contact Width

An analytical solution for the contact half-width a can be determined from Equation (2-23), knowing the composite modulus E^* and composite radius R^* one can determine a. For an ellipse the curvature is no longer constant thus, its curvature κ can

be computed for a point on the surface defined by the parametric coordinate θ. For an ellipse defined by semi-major axis a and semi-minor axis b the curvature is given by:

$$\kappa_{ellipse} = \frac{ab}{\sqrt{a^2 \sin^2\theta + b^2 \sin^2\theta}} \tag{6-1}$$

$$R_{ellipse}(\theta) = \frac{1}{\kappa} \tag{6-2}$$

For the location of the contact point ($\theta = \frac{\pi}{2}$) on the ellipse, the radius is $R_1 = 0.1$. For the bottom block, the radius is considered infinite giving: $R_2 \cong \infty$. This gives composite values for this contact problem as $R^* = 0.1$ and $E^* = 1.10\mathrm{E}+11$. Using Equation (2-23) and the final applied load N the analytical solution to contact half-width is given as $2.47\ mm$. The results found for the contact half-width are compared below:

Table 6-1. Contact Half-Width comparison for Example 1.

	Analytical Solution	Projected Results	Non-Projected Results
Contact Half-Width a [mm]	2.47	2.399	1.694
Percent Error		**2.88%**	**31.4%**

While the non-projected results are within an order of magnitude of the expected solution, the projected solution results in a much lower error as well as faster convergence, and the projected results have a faster solution time even considering it has to perform an iterative search on an ellipse each time an integration point is projected.

6.1.2. Comparison of Contact Pressure

Using the computed contact width a, and the known externally applied normal load reaction, the contact pressure distribution will take on the elliptical distribution from Equation (2-19). This is compared to the IBFEM results for the pressure within the contact region in Figure 6-3. It can be seen the non-projected results do not reflect the

expected distribution, while the projected solution matches very well. The peak pressure P_0 can be computed using total rection force from the fixed displacement condition via Equation (2-20).

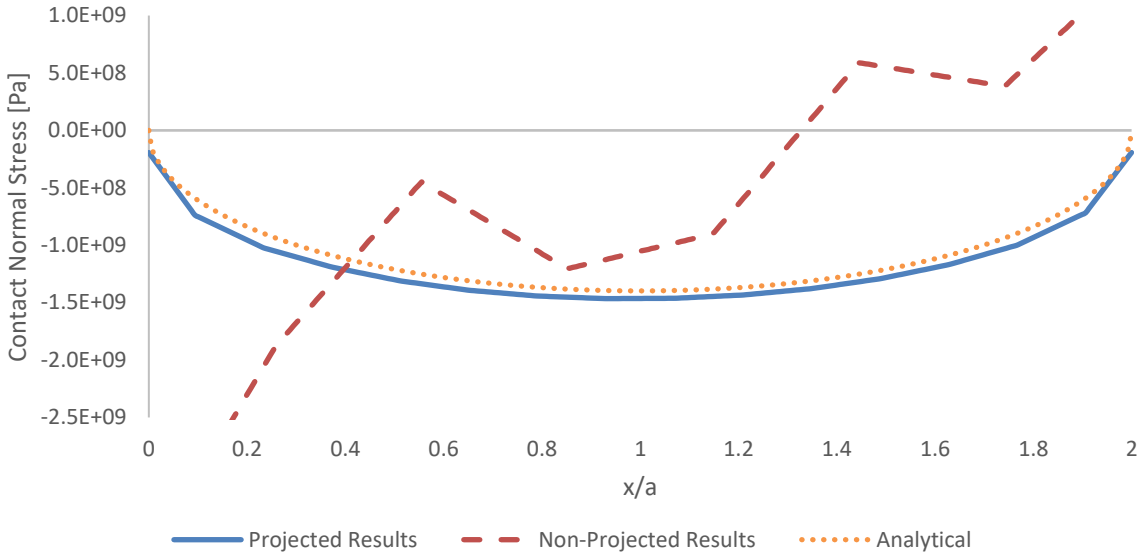

Figure 6-3. Contact pressure distribution using both the IBFEM method with projection and without projection compared to the analytical solution.

6.1.3. Comparison of Sub Surface Von Mises Stress

Numerical solutions have been computed for ellipse-on-ellipse contact. For line contact, such as the current case, the peak Von Mises Stress is found to be $0.558P_0$ with a vertical location of 0.703a [26]. The sub-surface Von Mises Stress plots are compared for both the projected and non-projected results. The numerical peak stress and location computed in [26] are also included for comparison. The projected solution closely matches the peak stress and location. The projected solution also lacks the surface singularity which is found in the non-projected result. However, the non-projected results still yield semi-accurate results away from the contact point.

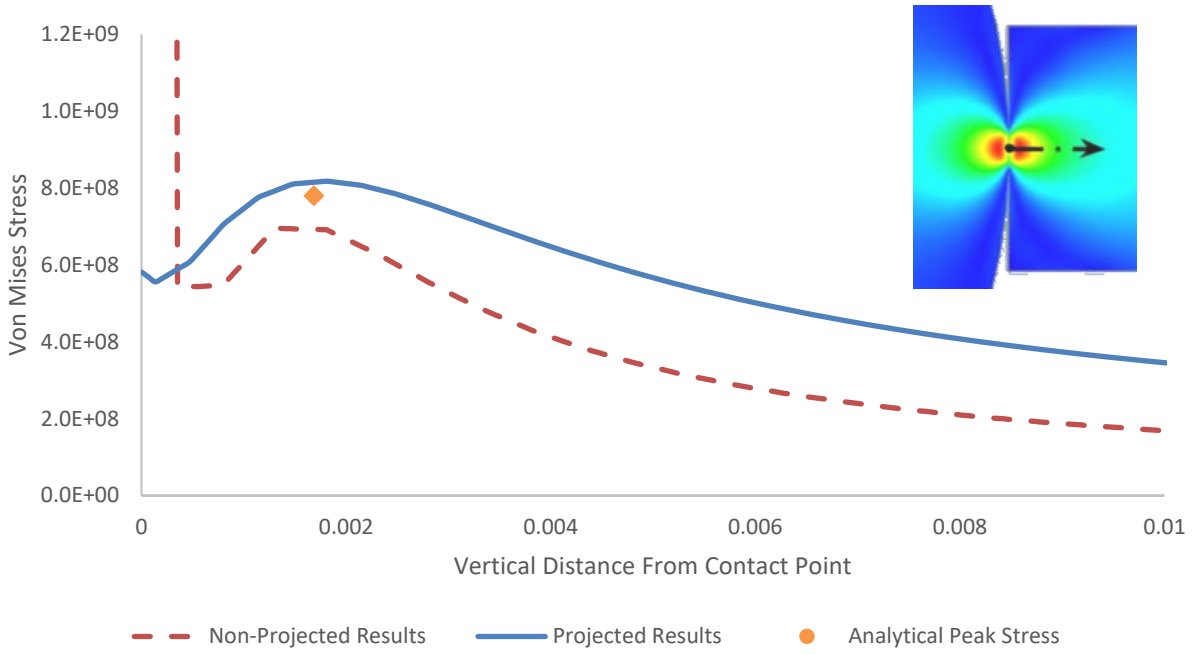

Figure 6-4. Subsurface Von Mises stress along the vertical axis from the contact point.

6.1.4. Displacement results

The displacement magnitude is shown for the projected result in Figure 6-5 and the non-projected results in Figure 6-6. Within the contact region, the project result displacements are continuous, which is the expected result for Hertzian contact; however, for the non-projected results, an asymmetry appears with what looks like contact only on the left side. It may be noted in both cases, the same contact point was used, along with the same mesh. A possible source of asymmetry in the non-projected solution could arise from an imbalance in numeracy and position of the line segments used to approximate the surface. An even worse case arises when the contact point is in the middle of one of these approximate line segments instead of a vertex, thus making it hard to identify if the problem is point contact.

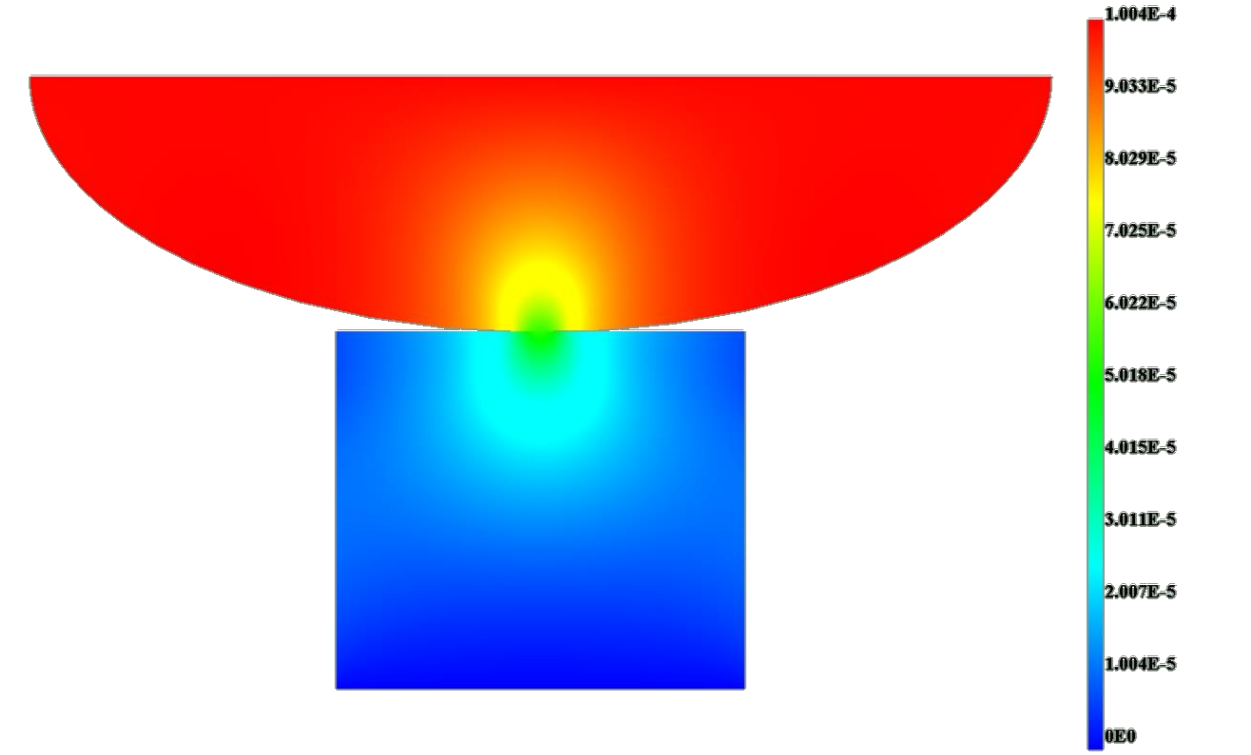

Figure 6-5. Projected result displacement magnitude.

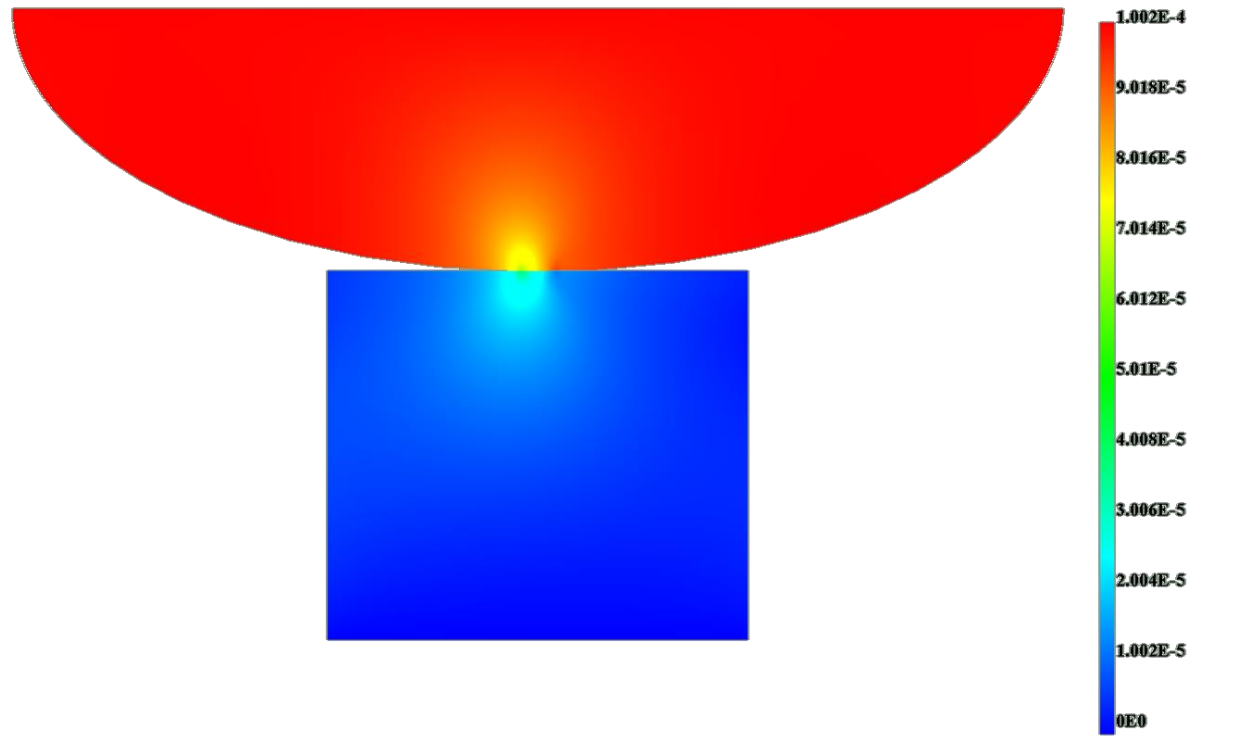

Figure 6-6. Non-projected result displacement magnitude.

6.2. Mesh Independent Convergence of Contact Width

For a contact analysis program to be reliable there needs to be consistent results across differing load and mesh conditions. There is also the expectation that the results are independent of the mesh used. To this effect, using the same geometry, various differing normal load boundary conditions are applied and compared to the analytical result. The error in contact width is also examined over progressively finer meshes. For this analysis, two elastically similar materials are used with a Young's modulus of $2 * 10^{11}$ Pa and Poisson's ratio of 0.3. The load is applied via a fixed displacement boundary condition, as shown in Figure 6-7.

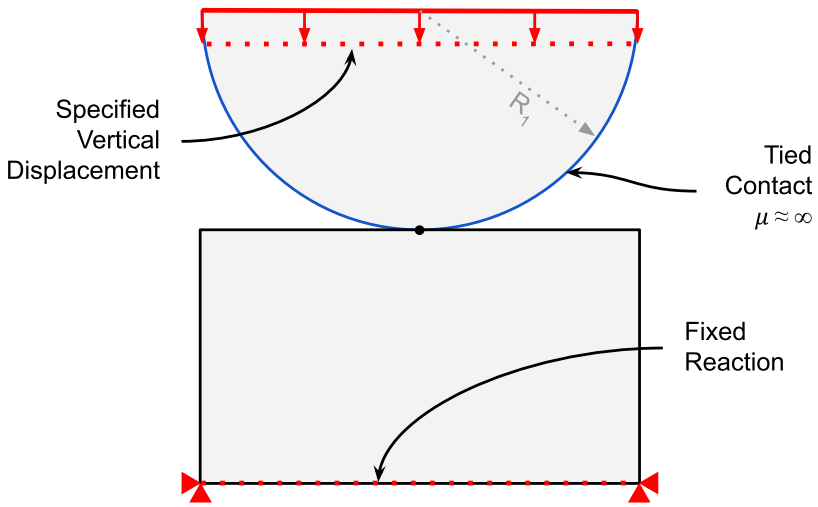

Figure 6-7. Boundary conditions for mesh independent convergence analysis. The bottom part is fixed at the bottom, while the top part has a specified displacement.

6.2.1. Comparison of Half-Width for Differing Loads

The non-linear nature of the relationship between the load applied and the contact width is given by Equation (2-23). This analytical solution depends on the geometry curvature and elastic constants. The IBFEM solution uses the identification of penetration and tension points to determine the contact width. These are compared

across multiple analyses where only the vertical displacement is varied, and the mesh is kept the same. For each vertical displacement, there is a corresponding reaction normal load; these analyses are compared in Figure 6-8. As can be seen, the IBFEM result closely matches the analytical expectation for half-width across various applied displacements.

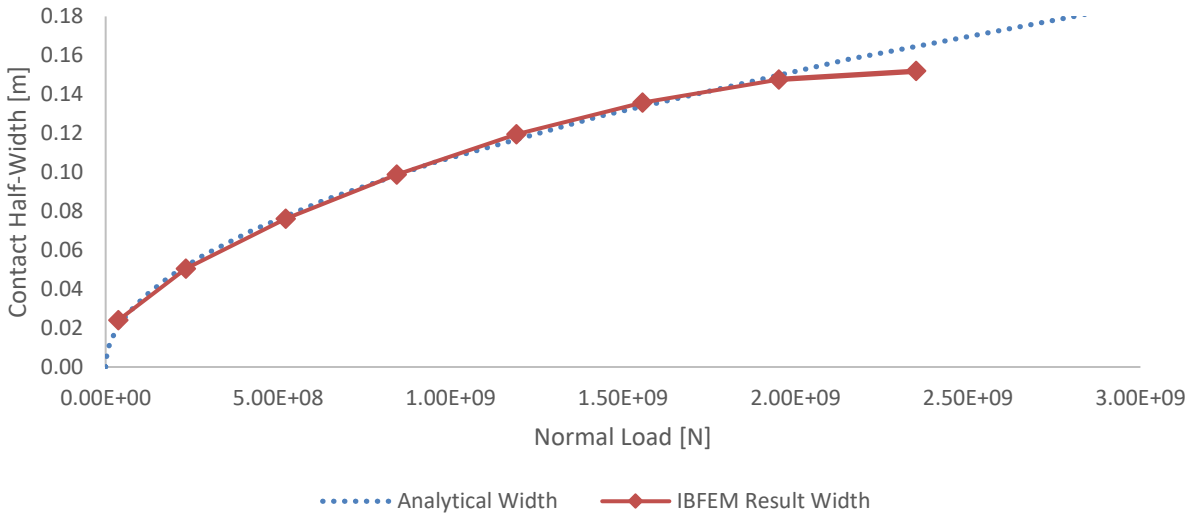

Figure 6-8. Contact half-width computed during eight different analyses while using the same mesh density (25 contact elements). Only the normal load boundary condition was varied between analyses. This is compared to the analytical contact half-width from (2-23)

6.2.2. Error In Contact Width Across Differing Meshes

Using the same geometry and boundary conditions, multiple analyses were run. Between each analysis, only the mesh density was varied. The results of this can be seen in Figure 6-9; one can observe with an increase in mesh density, the error in contact width progressively reduces until it oscillates around the true answer with an error bounded by 3% for fine meshes. In this case, the number of elements used refers to the number of contact elements and not the total number of elements in the mesh. An example of a course and dense mesh used for the analysis is shown in Figure 6-10.

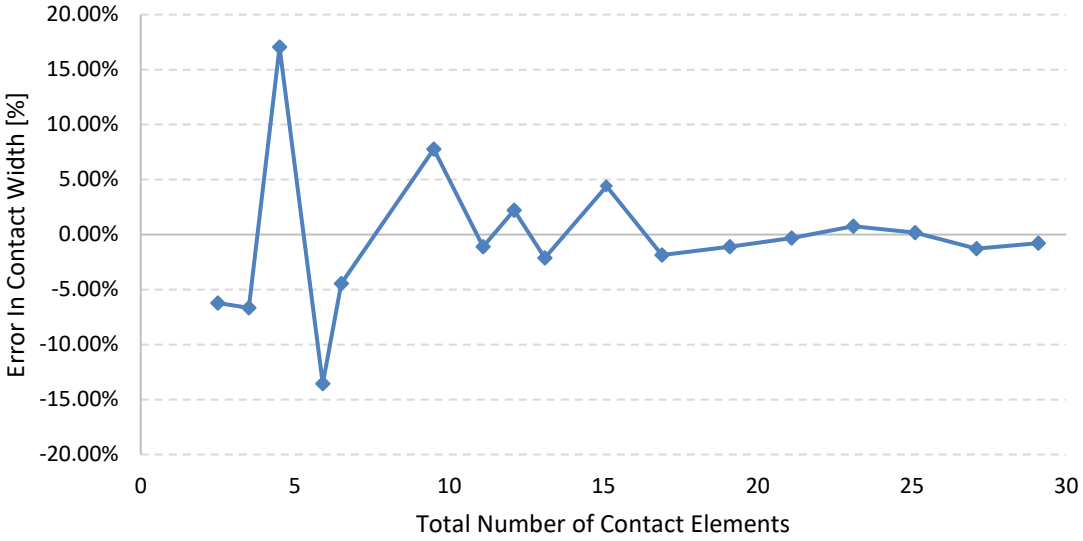

Figure 6-9. Error in contact half-width compared across increasing mesh density. The same boundary conditions were used for all analyses with only the background mesh was modified

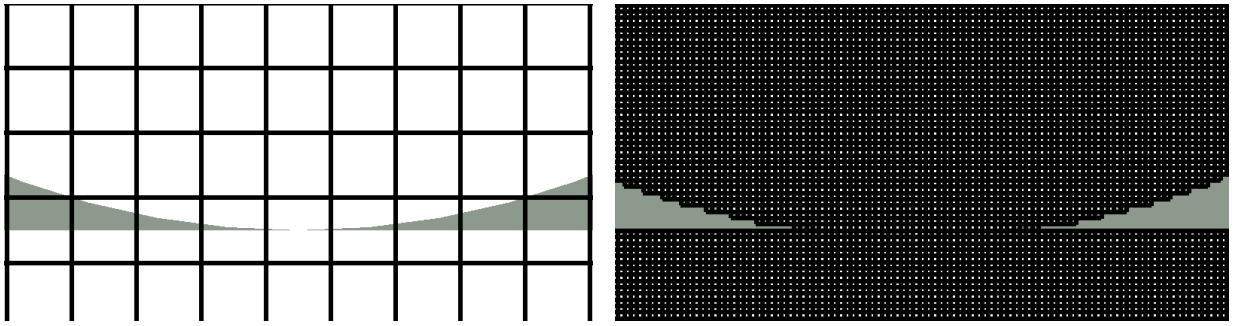

(a) (b)

Figure 6-10. Comparison of mesh densities: (a) Course mesh containing ~5 contact elements (b) Fine mesh containing ~30 contact elements

6.3. Frictionless Contact

In frictionless contact, no tangential forces are transferred between the surfaces in contact. This means only pressure between parts in contact will be transferred. This is tested using cylinder-on-cylinder contact where a fixed vertical and horizontal boundary condition is specified; this is shown in Figure 6-11. The expected result is a stress distribution identical to Hertzian contact theory while allowing the specified displacement in a tangential direction without any resistance; thus, in this case, there is no tied region instead only a sliding region. Frictionless contact is a purely

manufactured concept; however, this example helps validate the allowance for sliding within the new contact formulation. Frictionless contact is also available in many FEM applications [16].

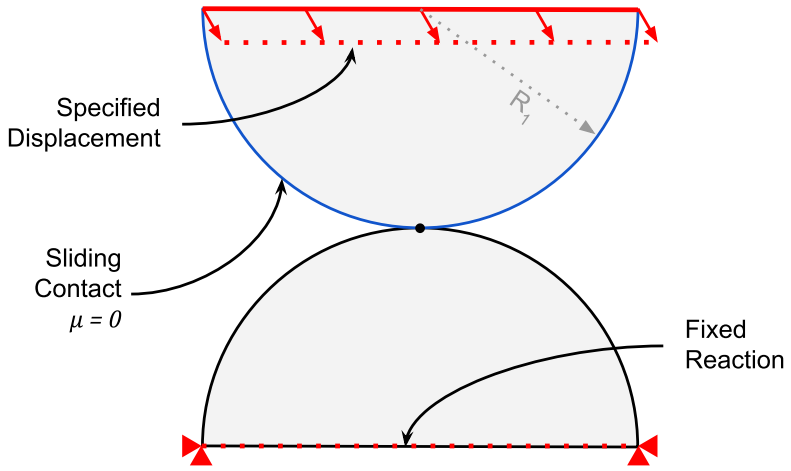

Figure 6-11. Cylinder-on-Cylinder boundary conditions. Both vertical and horizontal displacements are specified. The contact is frictionless with $\mu = 0$.

6.3.1. Contact Width Comparison

The resulting reaction on the top boundary was found as $[F_x \quad F_y] = [-1.30 * 10^6 \quad -7.49 * 10^8]$ which is equal and opposite to the bottom boundary. For cylinder-on-cylinder contact of elastically similar materials, the expected contact region is a flat line. In this case, this is along the x-axis; thus, for frictionless contact, one would expect $F_x = 0$. Consider an estimate of the expected friction if it was included as $\mu F_y = 0.3F_y = 1.5 * 10^8$. This force is two orders of magnitude larger than the found value of F_x; thus, making it a numerical error most possibly due to the found contact width not being truly flat.

The analytical solution for the half-width can be found similarly according to Equation (2-23). Using the composite modulus and radius, which for this problem is given as $R^* = 0.5\,m$ and $E^* = 1.1 * 10^{11}$ Pa. Which corresponds to an analytical half-

width of $0.06589\ m$. The half-width found from the analysis was found to be $0.0667\ m$ this results in a 1.37% error when compared to the analytical solution.

6.3.2. Displacement Results

The vertical and horizontal displacements are shown in Figure 6-12 it can be seen the displacements are continuous through the contact in the Y-direction while they are discontinuous in the X-direction. This is the expected result as without friction, there is no forces restricting movement in a tangential direction of the contact surface, which in this orientation is along the X-direction. The displacement in the Y-direction is the same results expected for purely Hertzian normal pressure contact, while the displacements in the X-direction are the fixed displacement plus Poisson effects from the contact.

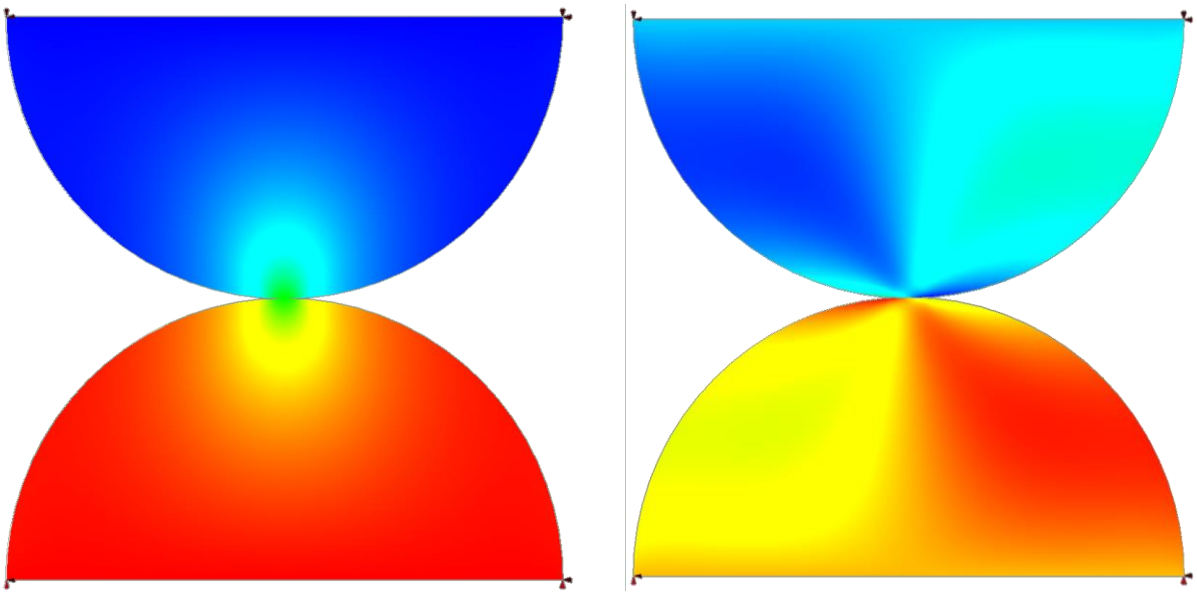

(a) Y-Displacement (b) X-Displacement

Figure 6-12. The components of displacement for frictionless contact (a) the displacement in the Y direction and (b) the displacement in the x-direction.

6.3.3. Von Mises' Stress Field

The Von Mises Stress is shown in Figure 6-13; the results are symmetrical in both the vertical and horizontal directions; this is because no meaningful force was transmitted in the tangential direction. This is the expected result for Hertzian contact, similar to the distribution shown in Example one. Thus, the fixed displacement in the horizontal direction (x-direction) has no effect on the final stress field. This is the expected result for frictionless contact as there should be no other resistance between the parts in contact other than normal forces transferred between them.

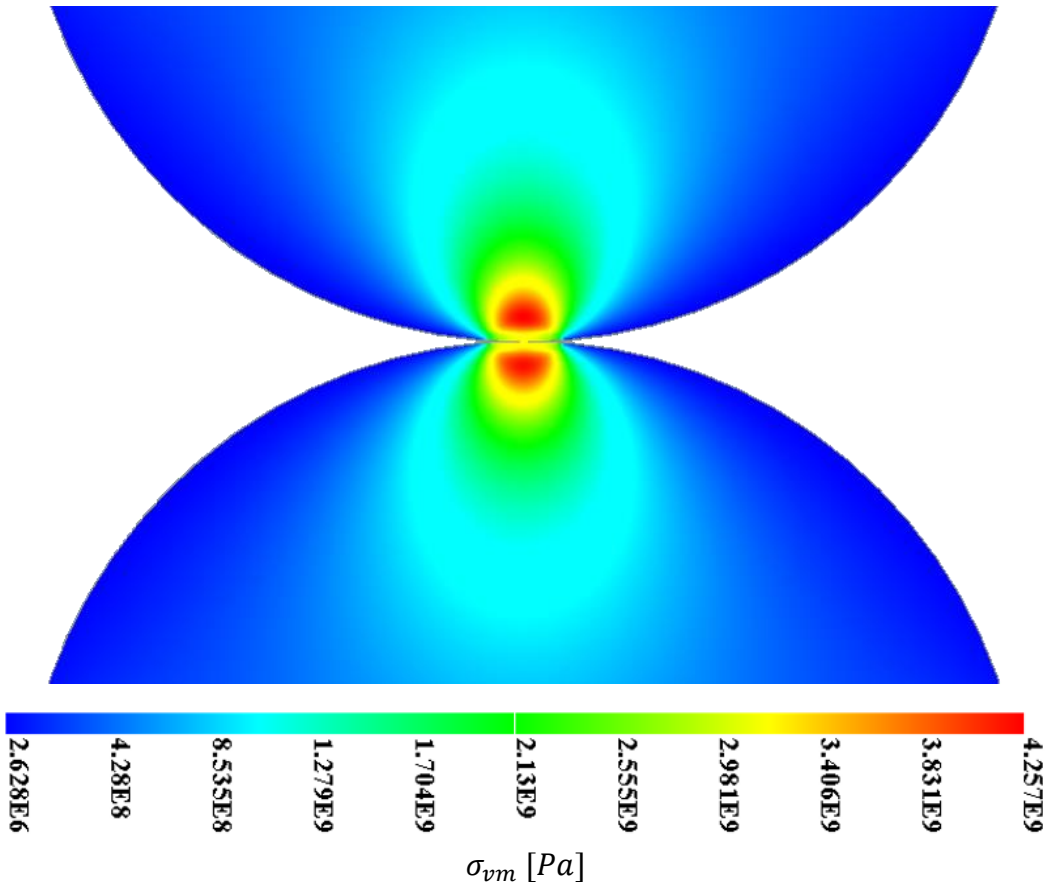

Figure 6-13. Von Mises Stress for Frictionless contact. This result is expected to match the Hertzian normal force only Von Mises contour plot.

6.4. Partial-Slip: Cylinder on Flat

Now partial slip is considered between a cylinder and a block, as shown in Figure 6-14. The coefficient of friction between the surfaces is 0.3 and both parts are elastically similar with a Young's modulus of $2 * 10^{11}$ Pa and Poisson's ratio of 0.3. A fixed displacement in both the vertical and horizontal direction is specified for the top boundary, while the bottom boundary is fixed.

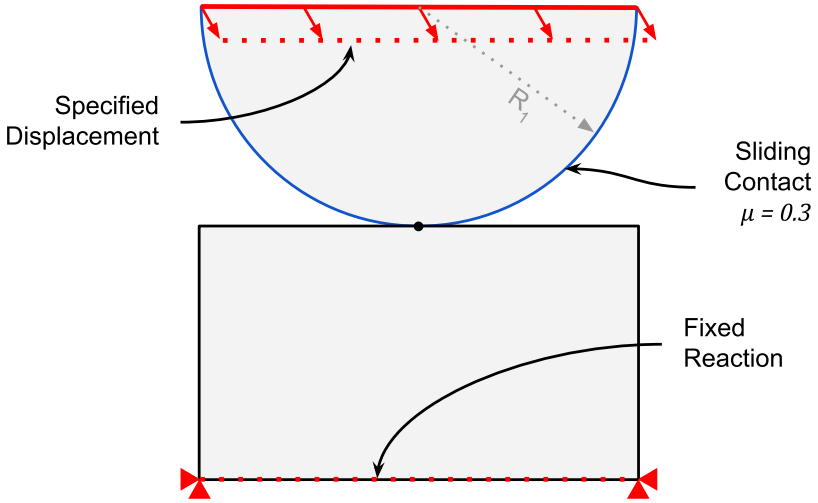

Figure 6-14. Cylinder-on-Flat plane boundary conditions. Both vertical and horizontal displacement is applied along the top boundary.

6.4.1. Contact Width and Ratio Comparison

From the specified displacement, the resulting reaction force, which is equal and opposite to the bottom fixed reaction, is $[F_x \quad F_y] = [-5.55 * 10^7 \quad -5.22 * 10^8]$. Due to the contact being along the Y-direction, the relation $[F_x \quad F_y] = [Q \quad N]$ can be made. Knowing the composite radius and modulus for this problem which is computed as $R^* = 1\ m$ and $E^* = 1.1 * 10^{11}$ the analytical half-width a can be determined from Equation (2-20). The analytical result for the contact ratio can be found knowing the ratio of shear force Q to the normal force N and the coefficient of friction between the parts from

Equation (2-29). Here, the contact force ratio $\frac{Q}{N}$ is 0.106 which corresponds to contact width ratio of 0.804. These results are compared in the table below.

Table 6-2. Contact half-width and ratio comparison for Example 4.

	Contact Width a [m]	Contact Ratio c/a
Analytical Solution	0.07777	0.803669
IBFEM Result	0.07818	0.801898
Percent Error	**0.52%**	**0.22%**

The resulting widths are very accurate to the analytical solution, with a relative error under one percent.

6.4.2. Contact Region Shear Stress

The shear stress along the contact surface is plotted in Figure 6-15 along with the analytical result, which is given by Equation (2-25). The x-axis is normalized by the half-width a. As can be seen, the IBFEM results are overestimated compared to the analytical result. This error could be attributed to not plotting along the exact region of contact.

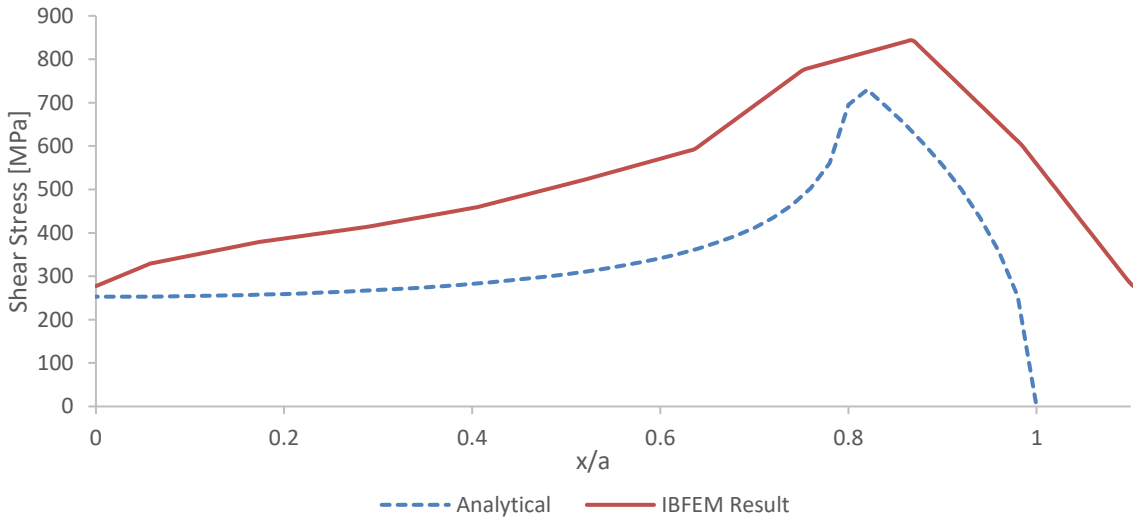

Figure 6-15. Shear Stress through the contact half-width compared to the analytical result. Only half of the geometries' contact width is plotted.

6.4.3. Contact Region Normal Stress

The expected contact pressure or normal stress distribution should be the same elliptical one defined for Hertzian contact. The pressure distribution at the contact region is given by Equation (2-19) and depends only on the contact half-width a and total normal force N transferred through the contact. This analytical result is compared to the IBFEM result in Figure 6-16, which is normalized by the peak contact stress $P_0 = 4.25E9\ Pa$ and the contact half-width a.

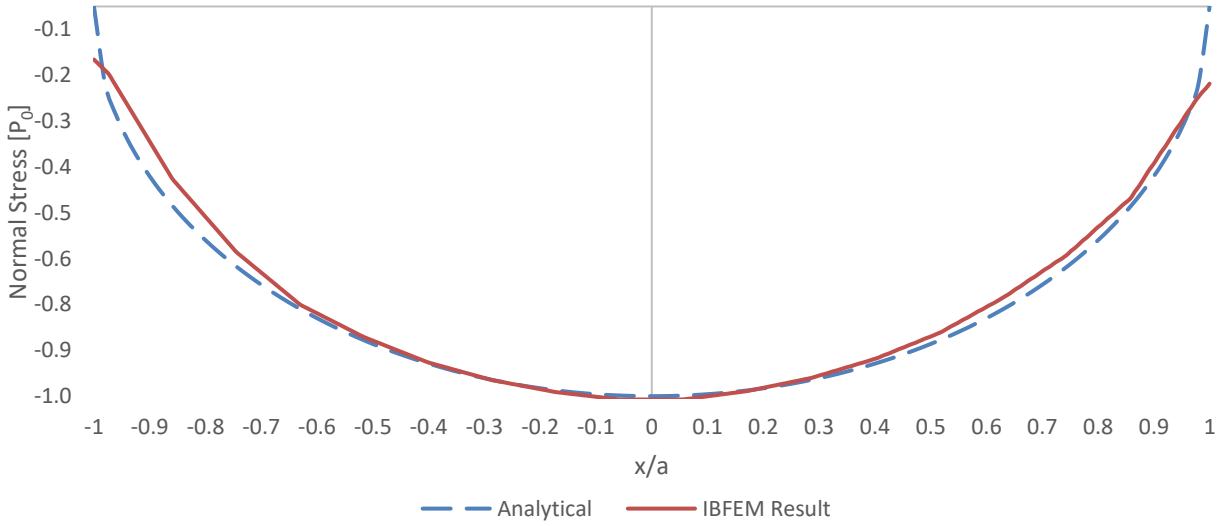

Figure 6-16. The Normal Stress plotted through the contact region.

As can be seen from Figure 6-16 the IBFEM analysis results in a close match to the analytical solution. Unlike the shear plot, the normal pressure is less sensitive to ensuring your plot is directly along the contact boundary, which helps with accuracy while comparing.

6.4.4. Von Mises Results

The Von Mises Stress distribution is shown in Figure 6-17; the key difference that can be observed from the preceding examples is the tilt in the location of the peak Von Mises stress. This is exemplified in (b), where a vertical line is drawn to show this tilt.

(a)

(b)

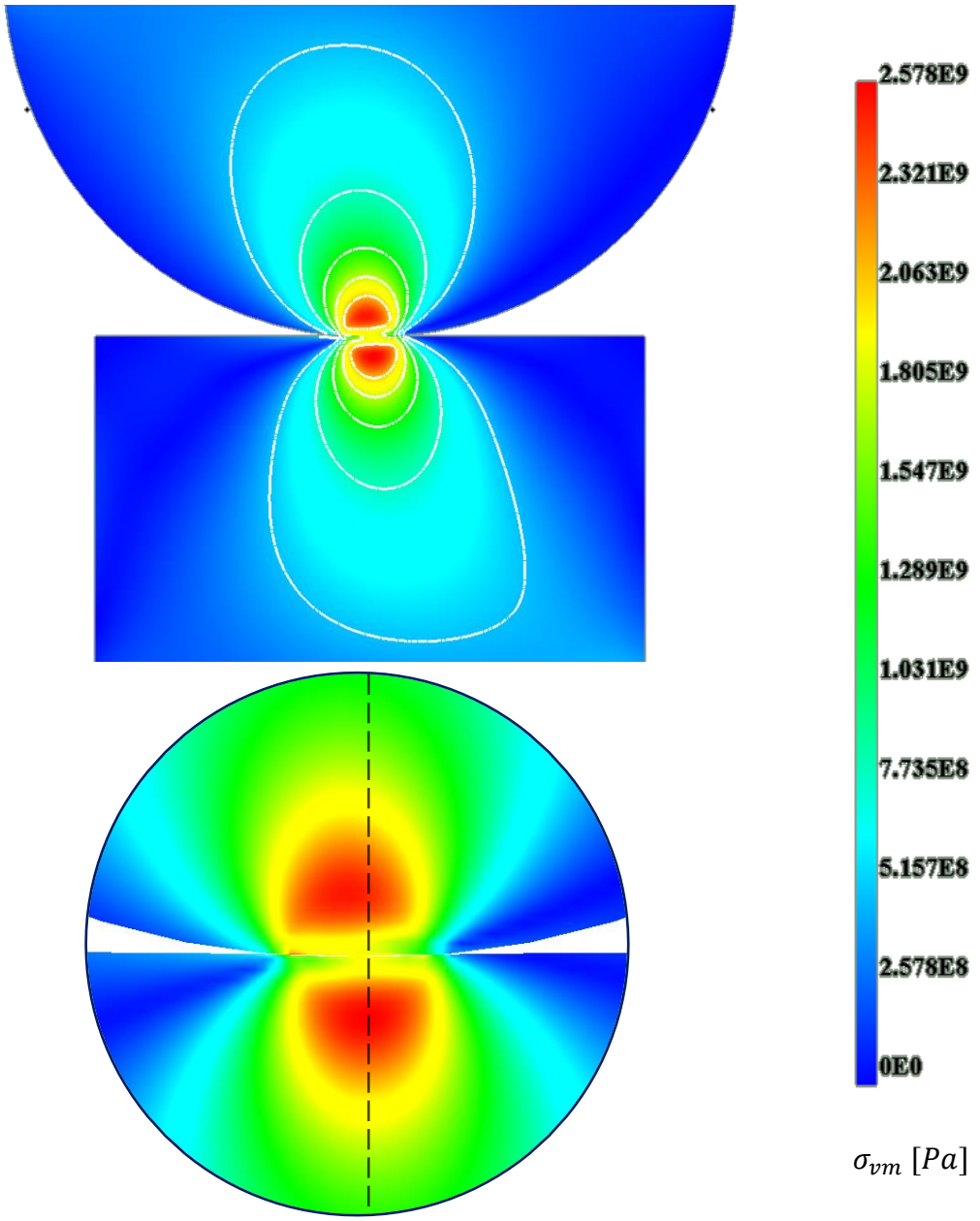

Figure 6-17. Von Mises' Stress field for cylinder-on-flat contact under partial slip. (a) Full result view (b) Zoomed, contact region result view

The full analytical stress field cannot be readily computed and compared for partial-slip problems [14]. However, consider Figure 6-18 reproduced from the results of a physical experiment that used photoelasticity to show the true stress field. Photoelasticity is an experimental method which makes use of birefringence properties of some materials (ie. Plastics and glass) to visualize the stress field. When these

materials undergo stress light passing through is doubly refracted in two directions along the principal axis of stress thus allowing for the identification of the maximum shear stress [27]. Qualitatively Figure 6-18 can be compared regarding the expected stress contour shape however the tilt angle is dependent on boundary conditions.

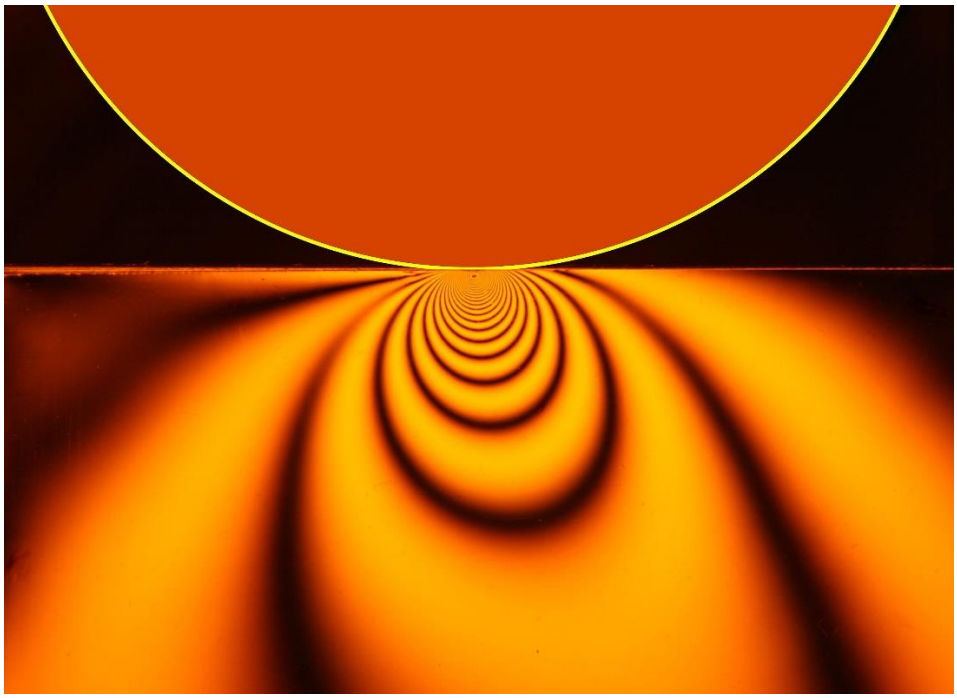

Figure 6-18. "Stresses produced by a contact with a combined normal and tangential load made visible by polarization optics" courtesy of Valentin Popov, who released this image into the public domain [17].

6.5. Partial-Slip: Cylinder on Cylinder

Partial slip is now considered between two cylinders, as shown in Figure 6-19; these boundary conditions are similar to the frictionless example, except now partial-slip with friction is considered between the parts. The top boundary has a specified vertical and horizontal displacement, while the bottom boundary is fixed. The coefficient of friction between the surfaces is 0.3, and both parts are elastically similar with a Young's modulus of $2 * 10^{11}$ Pa and Poisson's ratio of 0.3.

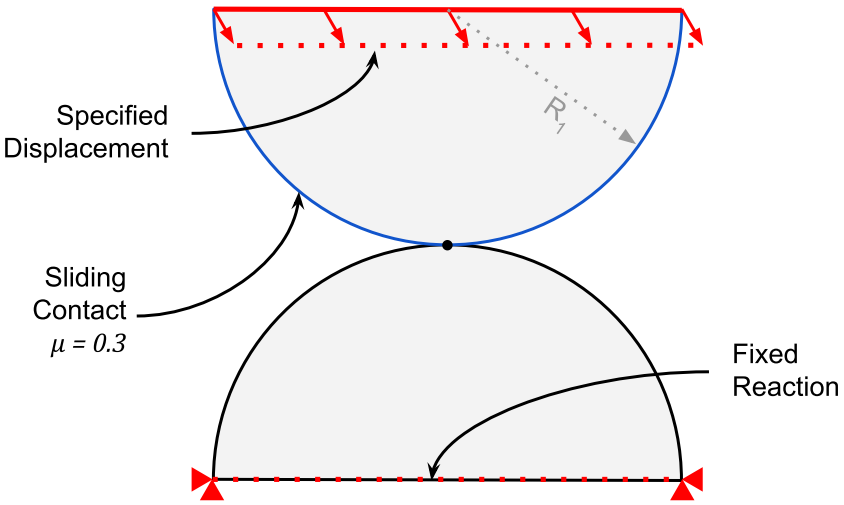

Figure 6-19. Boundary conditions for Cylinder-on-Cylinder contact under partial-slip.

6.5.1. Contact Width and Ratio Comparison

The analytical half-width a can be computed the same as the frictionless example. Knowing the composite radius and modulus given for this example as $R^* = 0.5\ m$ and $E^* = 1.1 * 10^{11}\ Pa$. The analytical contact ratio can be computed knowing the reactions on the top boundary, which was found from the analysis as: $[F_x \quad F_y] = [8.69 \times 10^7 \quad -7.50 \times 10^8]$. This gives a contact force ratio of 0.116, from which the analytical contact ratio can be found from Equation (2-29). The analytical contact half-width and ratio are compared to the IBFEM results in the table below. It can be seen that the IBFEM matches very closely with the analytical solution.

Table 6-3. Contact half-width and ratio comparison for Example 5 Cylinder-on-Cylinder contact.

	Contact Half-Width a [m]	Contact Ratio c/a
Analytical Solution	0.06593	0.78342
IBFEM Result	0.06523068	0.792036
Percent Error	**1.06%**	**-1.10%**

6.5.2. Contact Region Normal Stress

The contact normal stress through the contact region is plotted in Figure 6-20 and compared to the analytical solution given by Equation (2-19). The y-axis is normalized by the peak pressure $P_0 = 7.25 * 10^9\ Pa$ while the x-axis is normalized by the contact half-width a.

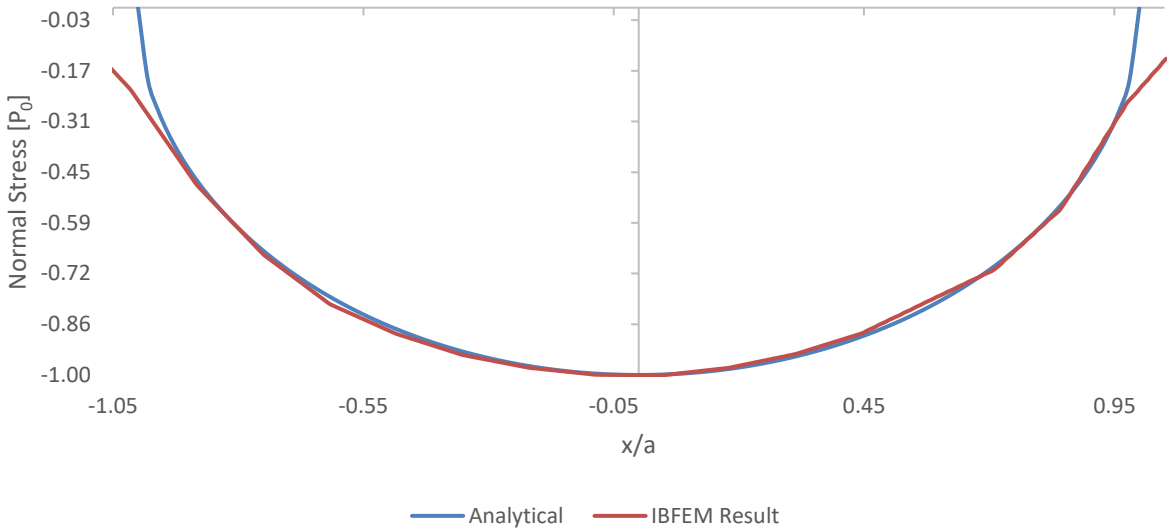

Figure 6-20. Normal stress through the contact region for Cylinder-on-Cylinder contact

The result matches very well; however, some error can be accounted for by the fact this plot is not exactly along the contact surface. Instead, to achieve this, a plot needs to be made which follows along the surface, in this case, the circle. Thus, error in the region being plotted will get worse away from the contact region. This is compared to examples that have a plane where it is much easier to plot along the boundary since it is a straight line.

6.5.3. Stress Fields

The Von Mises field is shown in Figure 6-21, which can be compared roughly to the photoelasticity results shown in Figure 6-18. Note here the change in tilt direction is due to the tangential force being applied in the opposite direction compared to Example

4. The normal stress in the y-direction σ_{yy} field is shown in Figure 6-22 which on the contact region is effectively the normal stress between the parts or rather the pressure between them. It is this value this is plotted and compared in Figure 6-20 for the contact pressure. As can be observed σ_{yy} is symetric about both axis at the contact point, this is the expected result for herztian contact. Finally the shear stress field σ_{xy} field is plotted in Figure 6-23.

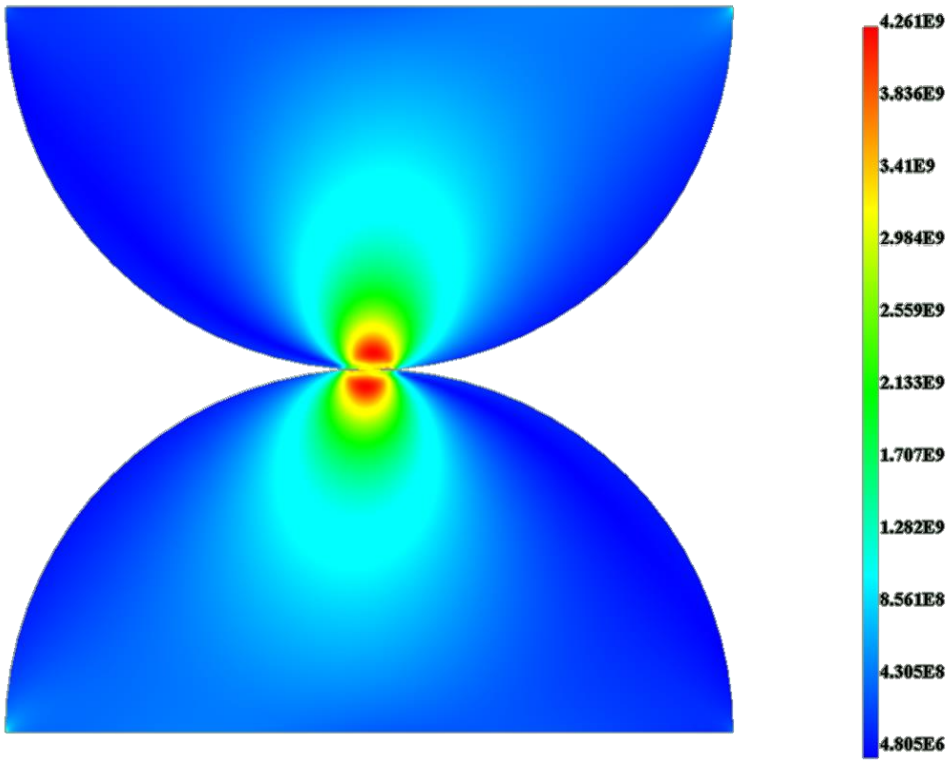

Figure 6-21. Von Mises' Stress for Cylinder-on-Cylinder contact with normal and tangential load

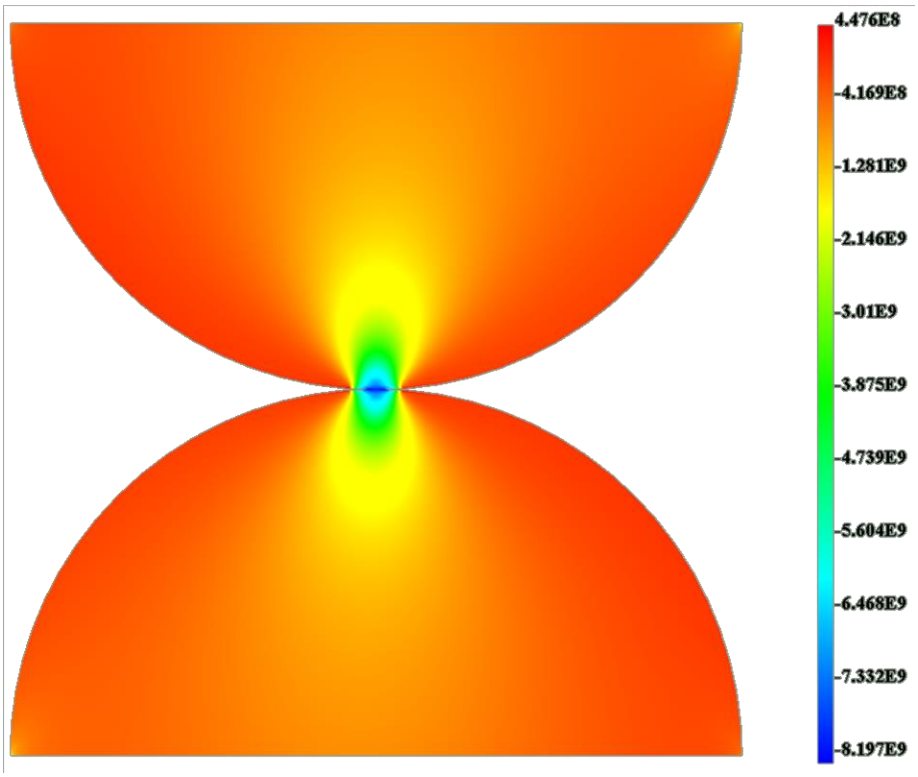

Figure 6-22. σ_{yy} stress field for Cylinder-on-Cylinder contact with normal and tangential load.

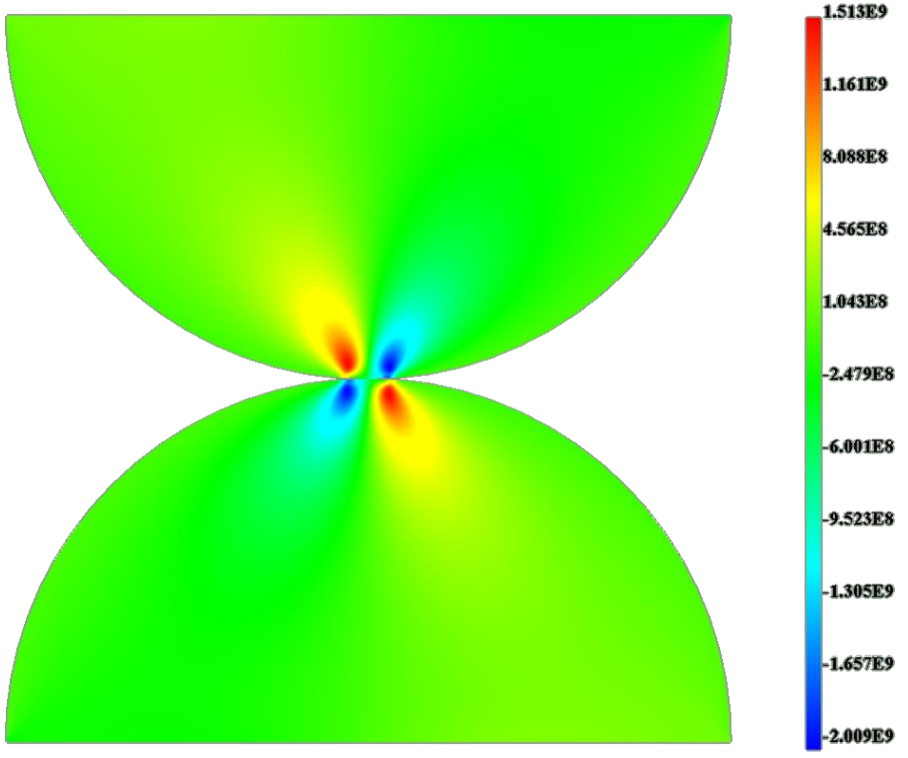

Figure 6-23. σ_{xy} stress field for Cylinder-on-Cylinder contact with normal and tangential load.

6.5.4. Displacement results

The x-component of displacement is shown in Figure 6-24; as can be seen, these values are now continuous through the contact region (at least within the tied region). This can be compared to the frictionless example where the displacements are not continuous. Note the geometry is such the x-axis is along the tangent of the contact point. The y-component of displacement is shown in Figure 6-25, where it can be observed the displacements are continuous through the contact region and follow a pattern like traditional Hertzian contact. This result can be compared to the frictionless example as shown in Figure 6-12, where a now a small tilt in the y-component contours of displacement can be observed.

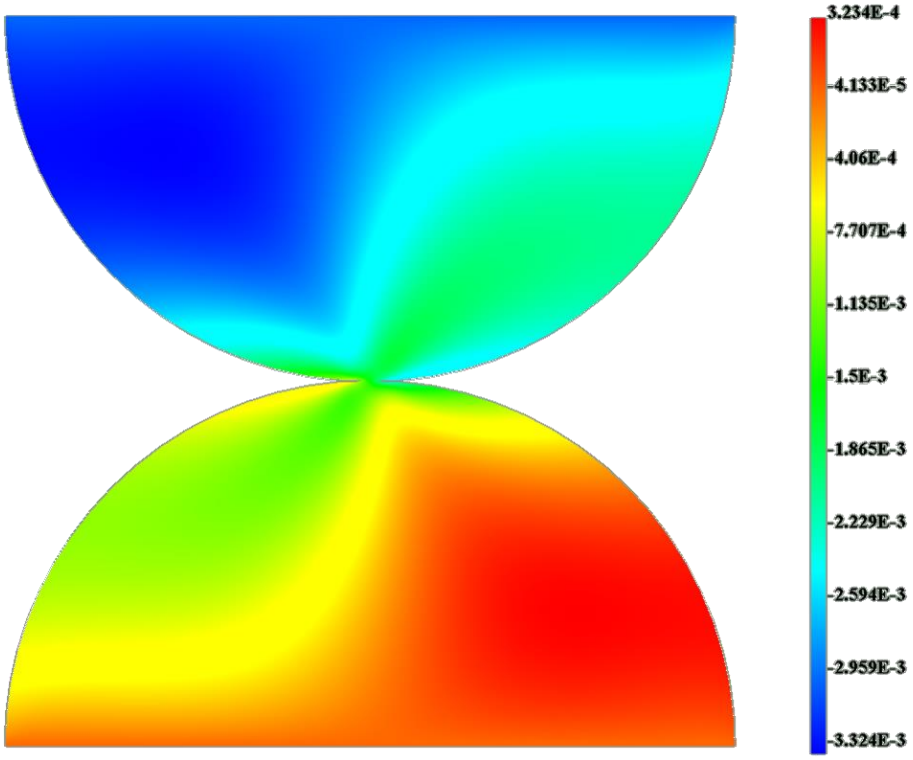

Figure 6-24. u_x displacement field for cylinder-on-cylinder point contact.

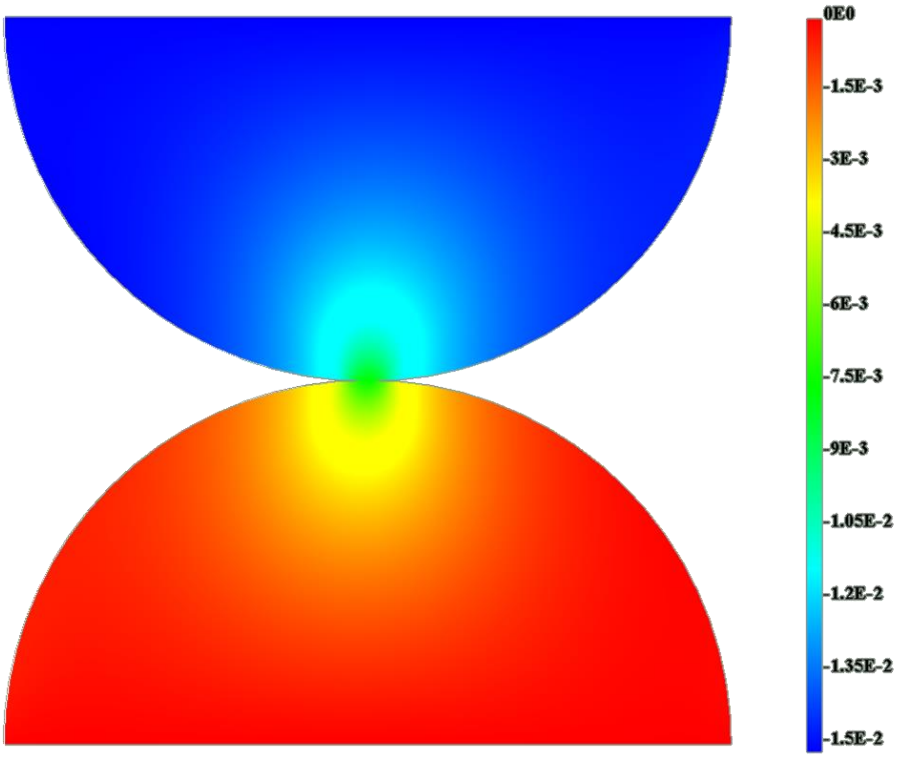

Figure 6-25. u_y displacement field for cylinder-on-cylinder point contact

6.6. Partial-Slip: Cylinder on Concave

In this example, now a concave partial slip condition is considered between elastically similar parts with a Young's modulus of $2 * 10^{11}$ Pa and Poisson's ratio of 0.3. The boundary conditions for this example are shown below in Figure 6-26; a fixed horizontal and vertical displacement of $-8mm$ and $0.5mm$ respectively is specified for the top boundary. The bottom boundary is fixed in place. The contact is applied to the top curve with a friction coefficient of $\mu = 0.3$ as shown in blue.

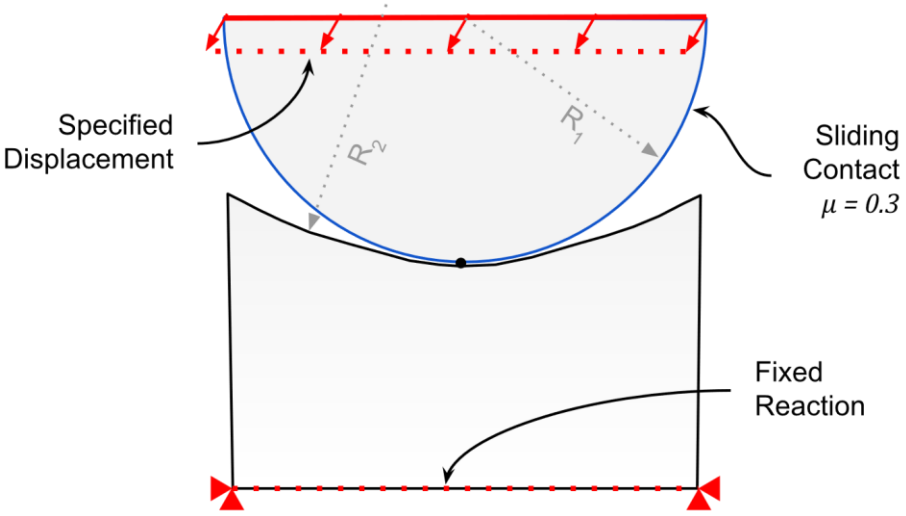

Figure 6-26. Boundary conditions for Cylinder-on-Concave. Both vertical and horizontal displacements are applied to the top boundary.

6.6.1. Contact Width and Ratio Comparison

The analytical half-width a can be computed like the other examples now accounting for the concave surface, which simply takes the form of a negative number as $R_2 = -2m$. The top circle has a radius of one, giving $R_1 = 1m$. From Equation (2-22), the composite radius is computed as $R^* = 2\text{m}$. From the parts elastic constants the composite modulus is computed from Equation (2-21) to be $E^* = 1.10 * 10^{11}$. This gives an analytical solution for the contact width from Equation (2-23) as 0.103 m. For cylinder on concave contact as the curvature of the two circles become equal in magnitude, the contact width gets larger and larger until they are fully in contact; in such a case, Equation (2-23) no longer holds as R^* becomes undefined. The force through the contact was found from the reactions as $[F_x \quad F_y] = [Q \quad N] = [1.72 * 10^7 \quad 4.63 * 10^8]$ which gives a load ratio of 0.037. From Equation (2-29) the contact ratio can be found as 0.936. These analytical values are compared to the IBFEM results in the table below.

Table 6-4. Contact half-width and ratio comparison for Example 6.

	Contact Half-Width a [m]	Contact Ratio c/a
Analytical Solution	0.10363	0.936093
IBFEM Result	0.099976	0.935674
Percent Error	**3.53%**	**0.04%**

There is a slight error in the contact width found a, while almost no error is found for the contact ratio suggesting the algorithm to compute the forces transferred to the contact elements is accurate.

6.6.2. Contact Region Shear Stress

The shear stress is plotted through the contact region in Figure 6-27, which is compared to the analytical solution given by Equation (2-25); the x-axis is normalized by the contact length a. As can be seen like other examples the shear stress is overestimated compared to the analytical solution, but the general shape is exhibited by the IBFEM result. This may be accounted for by plotting along the exact surface.

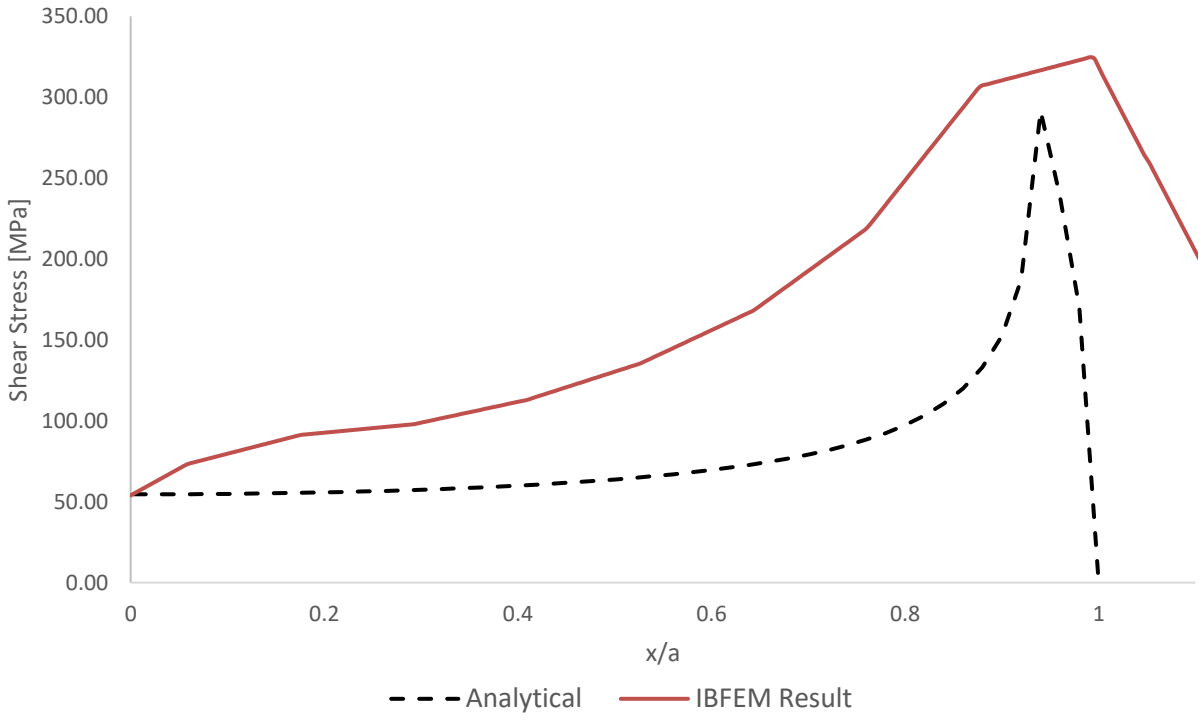

Figure 6-27. Shear Stress through the contact half-width compared to the analytical result for Cylinder-on-Concave contact. Only half of the geometries' contact width is plotted.

6.6.3. Contact Region Normal Stress

The normal stress which is the value σ_{yy} is plotted through the contact boundary in Figure 6-28; the IBFEM results are compared to the analytical solution given by Equation (2-19). Some error is associated with plotting as the plot is done along a straight line from the point of contact instead of along the actual surface, which in this case is curved.

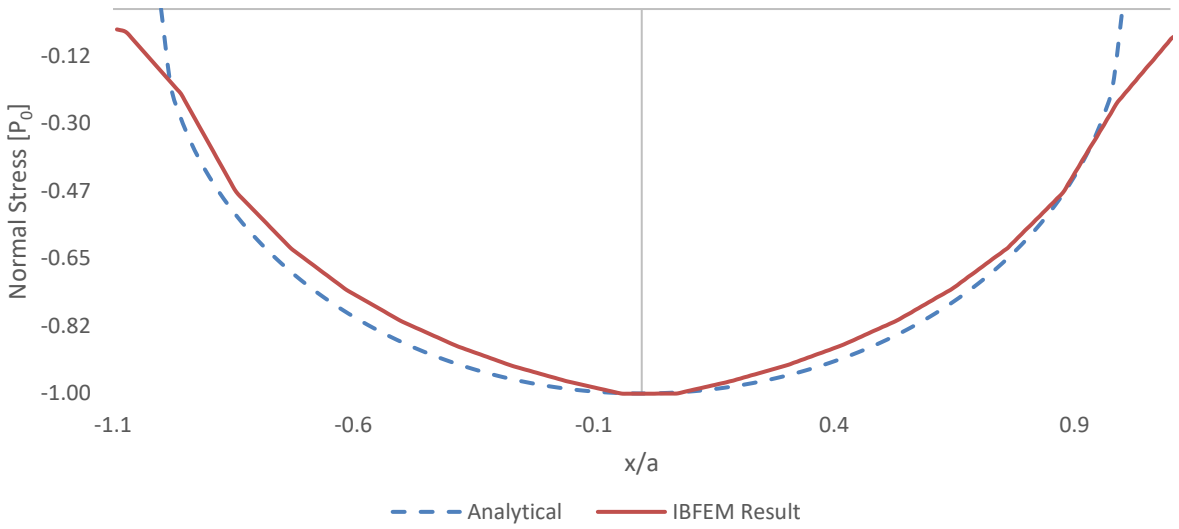

Figure 6-28. Normal Stress plotted through the contact region for Cylinder-on-Concave contact

6.6.4. Stress Fields

The Von Mises stress is shown in Figure 6-29; a tilt in the location of the peak stress is observed. However, compared to the previous examples, a much smaller tilt is seen; this is due to a larger contact ratio or a small load ratio. This is the expected result because as the load ratio approaches zero, the traditional Hertzian Von Mises stress distribution is found; thus, this tilt may be thought of as a function of the contact ratio.

The normal stress σ_{yy} distribution is shown in Figure 6-30 is symmetrical about the vertical axis, which is expected. The shear stress σ_{xy} field is shown in Figure 6-31, here one can observe some stress concentrations near the contact surface, these are not expected based on the analytical solution, otherwise the stress field matches the expected results.

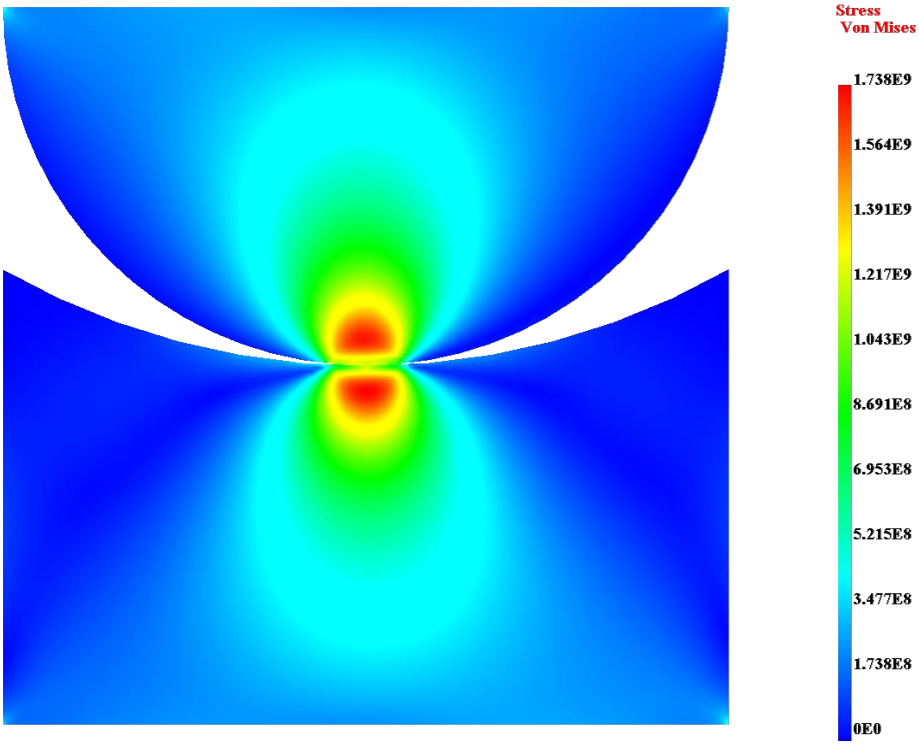

Figure 6-29. Von Mises' Stress field for Cylinder-on-Concave contact

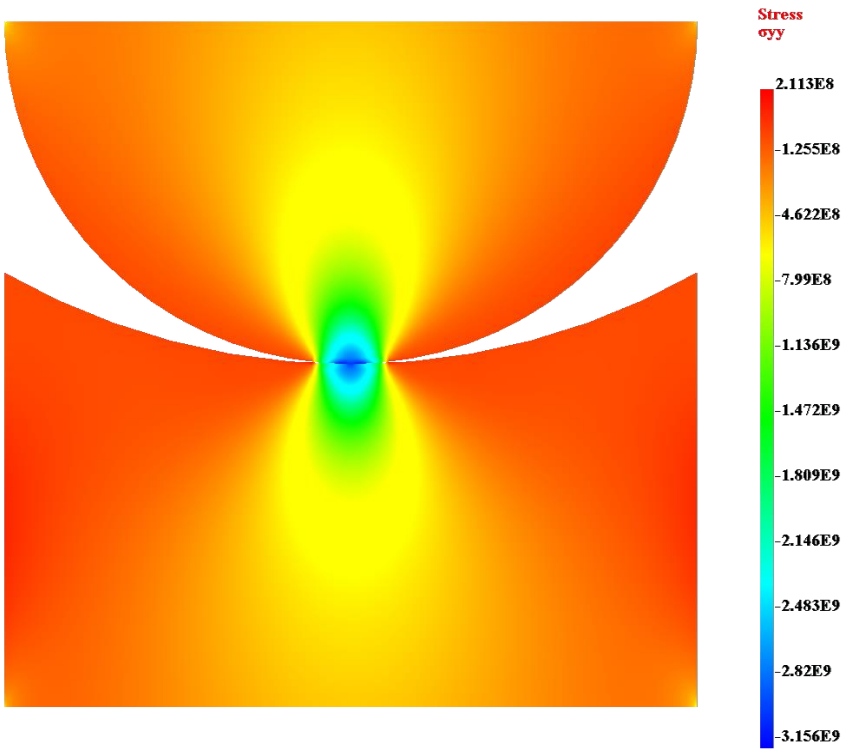

Figure 6-30. σ_{yy} stress field for Cylinder-on-Concave contact

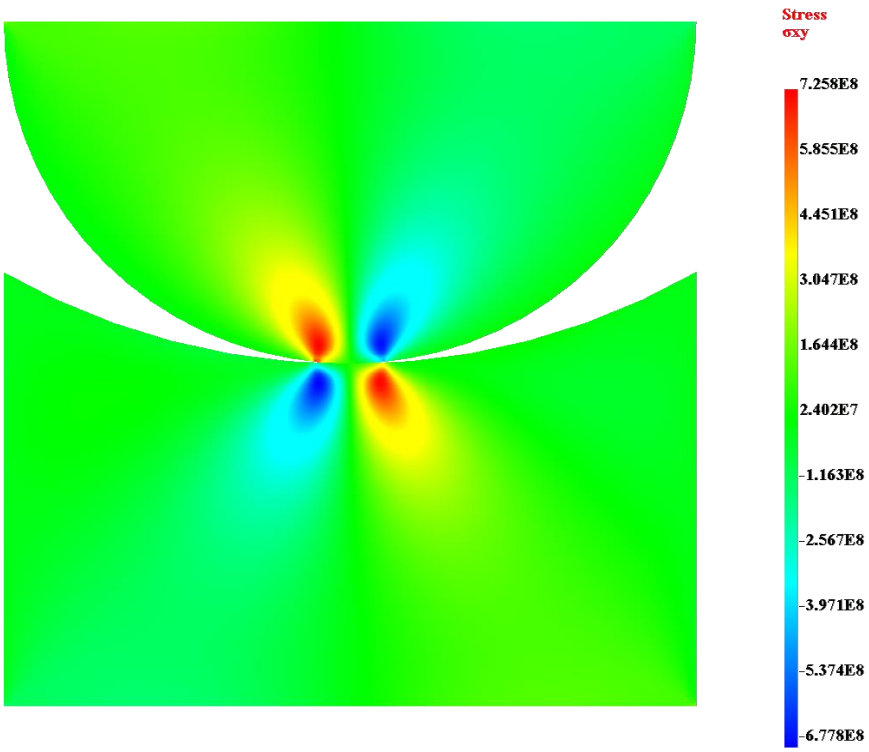

Figure 6-31. σ_{xy} stress field for Cylinder-on-Concave contact.

6.6.5. Displacement results

The x-component of displacement is shown in Figure 6-32; as expected, within the tied region, the displacement is continuous between the parts. Interestingly the largest x-displacement occurred not at the specified displacement but within the part. This could be accounted for by the low contact load ratio used for this example, allowing the x-direction displacement from Poisson's ratio effects to show up. The y-component of displacement is shown in Figure 6-33 and is continuous through the contact region with a similar result to other examples and the Hertzian solution.

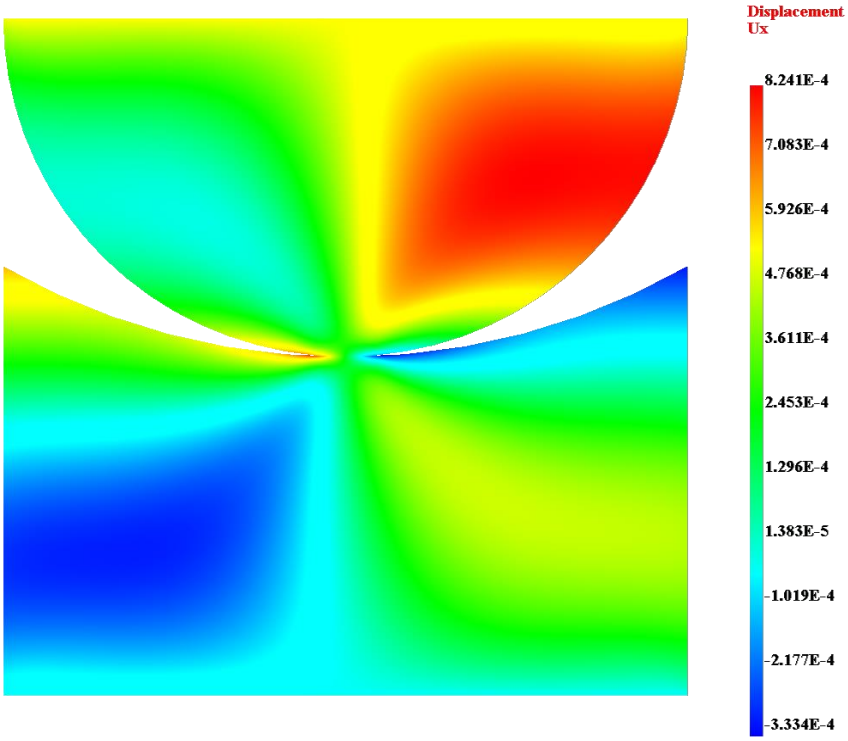

Figure 6-32. u_x displacement field for cylinder-on-concave point contact.

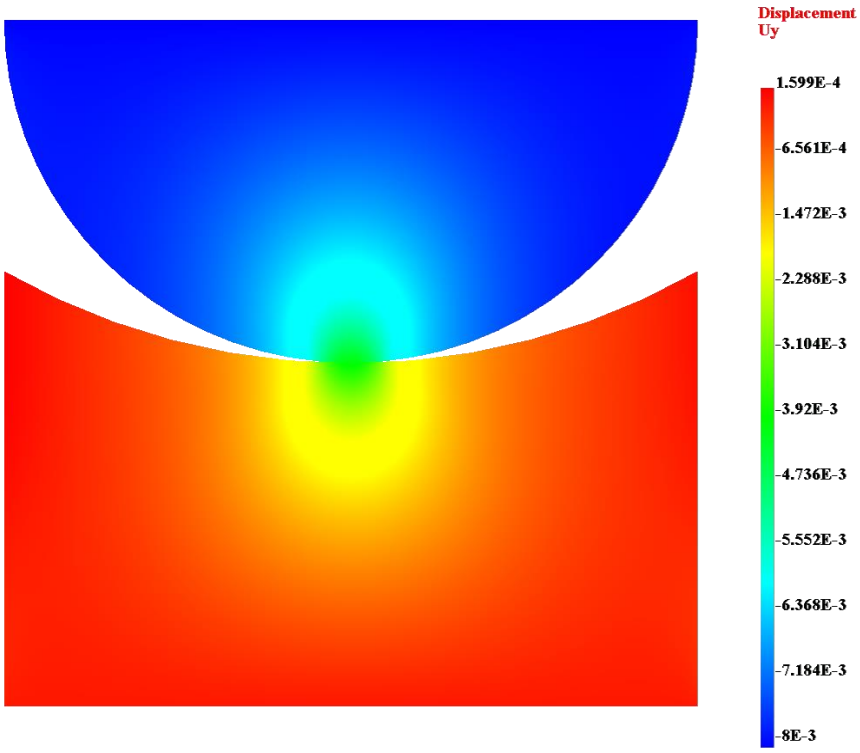

Figure 6-33. u_y displacement field for cylinder-on-concave point contact

6.7. Frictionless Sliding: Cylinder on Wedge

Consider a cylinder pushed into a wedge as shown in Figure 6-34; here only a vertical displacement is specified. However, due to the geometry of the problem at the contact point there exists both a vertical and horizontal force with respect to the global coordinate system. Since frictionless contact is considered, only a compressive force normal to the surface can be transmitted through the contact. There is a symmetry condition down the vertical axis as shown, and only half the model is analyzed using the IBFEM method. The total forces transmitted can be analyzed by considering the free body diagram of the cylinder as shown in Figure 6-35, due to the symmetry of the problem these contact points will also be symmetric. Knowing the angle of the contact force which can be found from the wedge angle, the contact normal F_n force component and tangential force component F_t.can be found as:

$$F_n = \sin(\theta)\, F_x + \cos(\theta)\, F_y \tag{6-3}$$

$$F_t = \cos(\theta)\, F_x - \sin(\theta)\, F_y = 0 \tag{6-4}$$

$$F_x = \tan(\theta)\, F_y \tag{6-5}$$

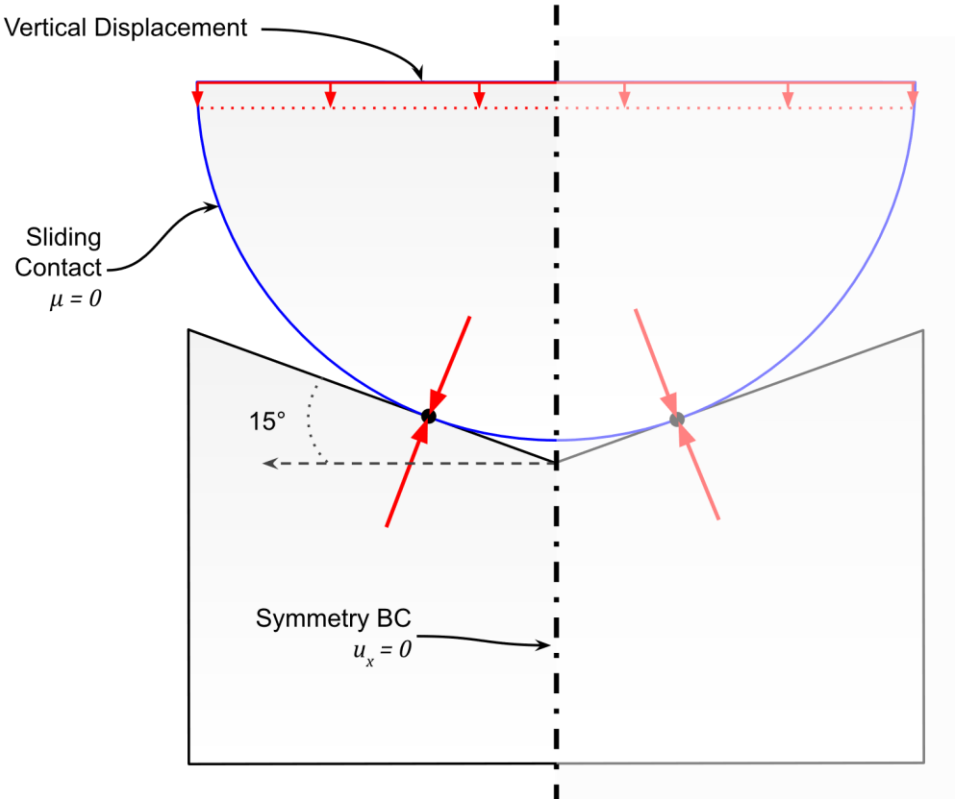

Figure 6-34. Boundary conditions for Cylinder-on-wedge. Only a vertical displacement on the top boundary is specified.

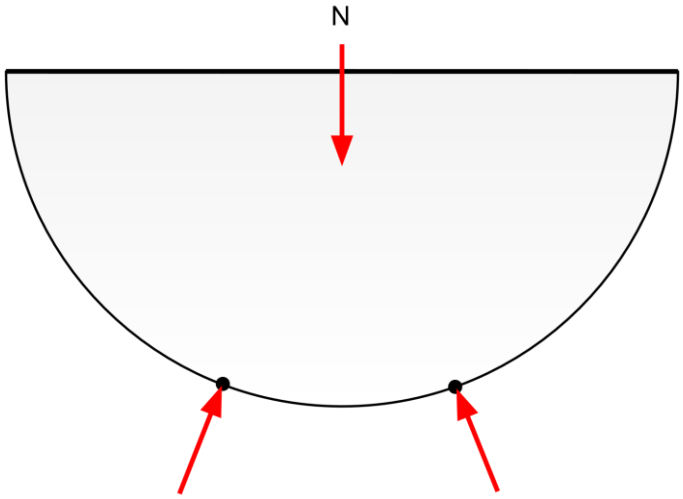

Figure 6-35. Free body diagram of the forces applied to the top cylinder.

For this example, the total force applied on the top boundary is $4.144 * 10^8$ N which results in an F_x value of $1.11 * 10^8$ N transmitted at the contact region from Equation (6-5). This results in a total normal contact load of $4.29 * 10^8$ N transmitted though the contact region.

6.7.1. Contact Width and Transmitted Force Comparison

Knowing the total normal load transmitted through the contact, alike previous examples, the analytical contact width can be computed using the Hertzian solution. Both parts are elastically similar, with a Young's modulus of $2E11$ Pa and Poisson's ratio of 0.3. The composite radius and modulus for this example are $R^* = 1\ m$ and $E^* = 1.1 * 10^{11}\ Pa$ the analytical contact half-width is computed to be 0.071 m using Equation (2-23). This result is compared to the IBFEM analysis of 0.074 m which results in a -4.15% error in contact half-width. This also validates the sliding contact formulation to problems when the contact direction is not in line with the global coordinate system (as with previous examples).

6.7.2. Stress Fields

The Von Mises stress field is shown in Figure 6-36, one can see the interaction of the stress field when two-point contacts are considered on the same cylinder. As this is frictionless contact the Von Mises plot is expected to have no tilt relative to the contact normal direction. The σ_{yy} and σ_{xx} stress fields are shown in Figure 6-37, unlike other example since the contact normal is not aligned with the global coordinate system now $\sigma_{yy} \neq \sigma_n$. However, a similar elliptical distribution within the contact region is found to the other Hertzian problems analyzed.

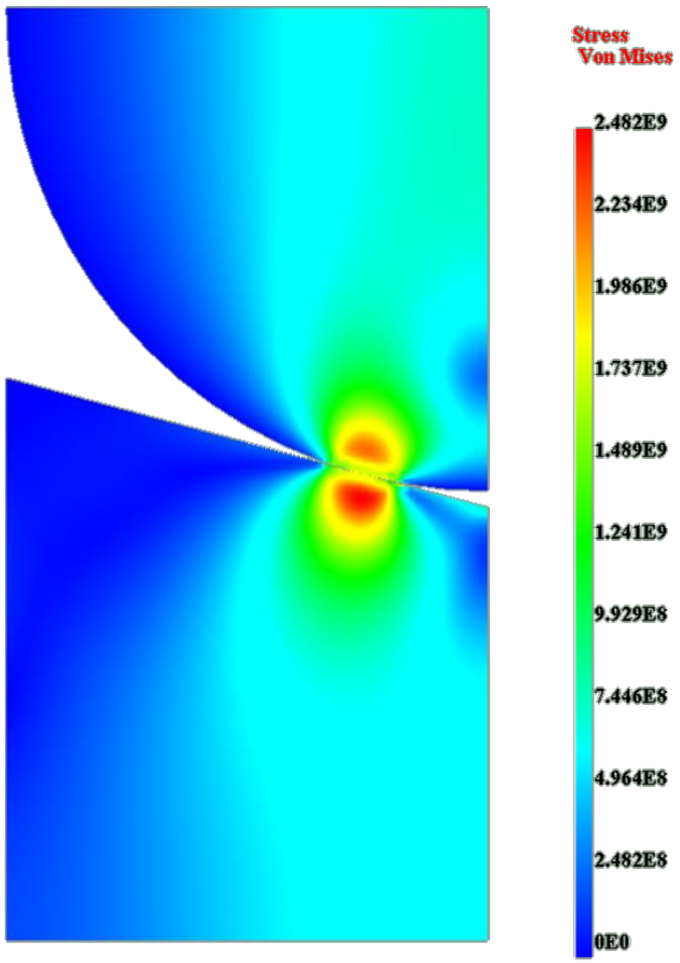

Figure 6-36. Von Misses Stress field for cylinder-on-wedge

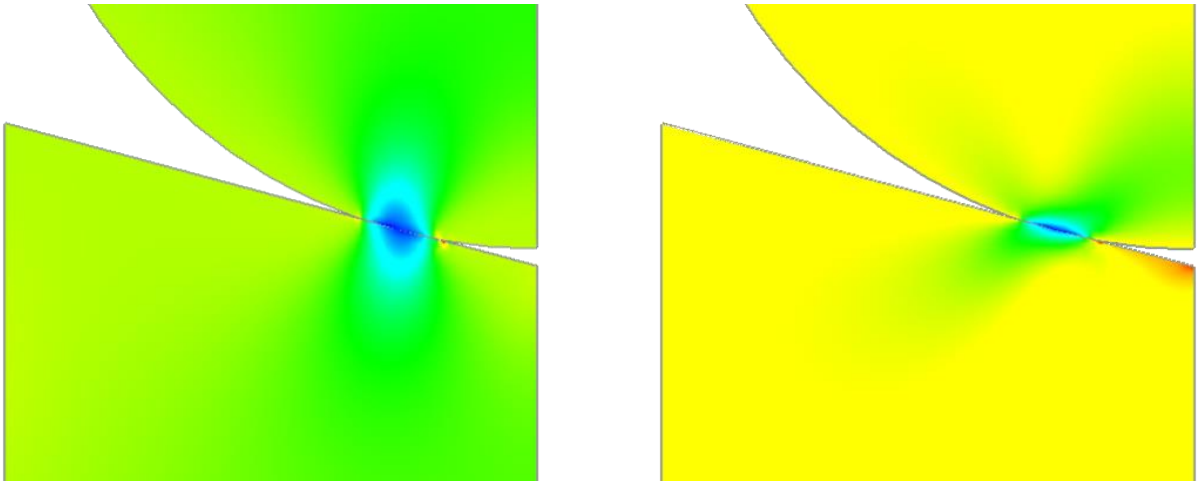

(a) (b)

Figure 6-37. (a) σ_{yy} stress field (b) σ_{xx} stress field for cylinder-on-wedge contact

6.7.3. Displacement results

The displacement magnitude is shown in Figure 6-38, one can see a similar continuous displacement through the contact region as in other examples. Also note the top boundary's specified vertical displacement boundary condition. The components of displacement are shown in Figure 6-39 again since the contact is no longer aligned with the global coordinate system the displacement along the contact direction is no longer the same as u_y (15 degrees off). Within the plot of u_x one can see it is not continuous between the parts, this is expected for frictional contact since the tangential load is generally aligned with the tangent of the contact normal.

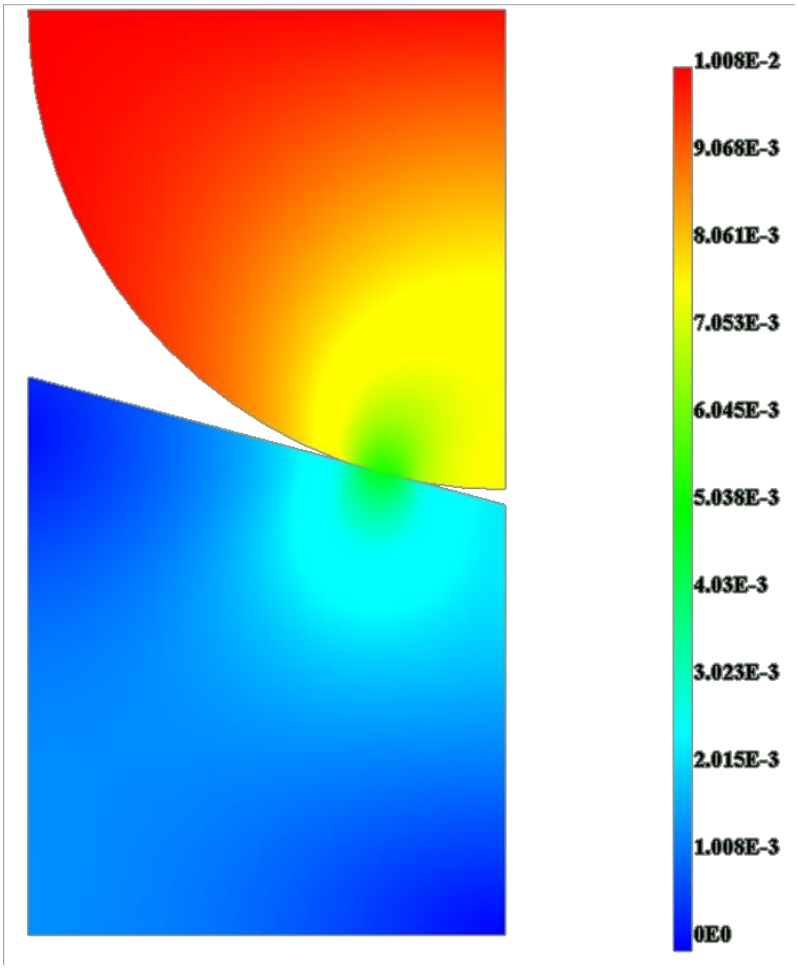

Figure 6-38. u magnitude displacement field for cylinder-on-wedge point contact.

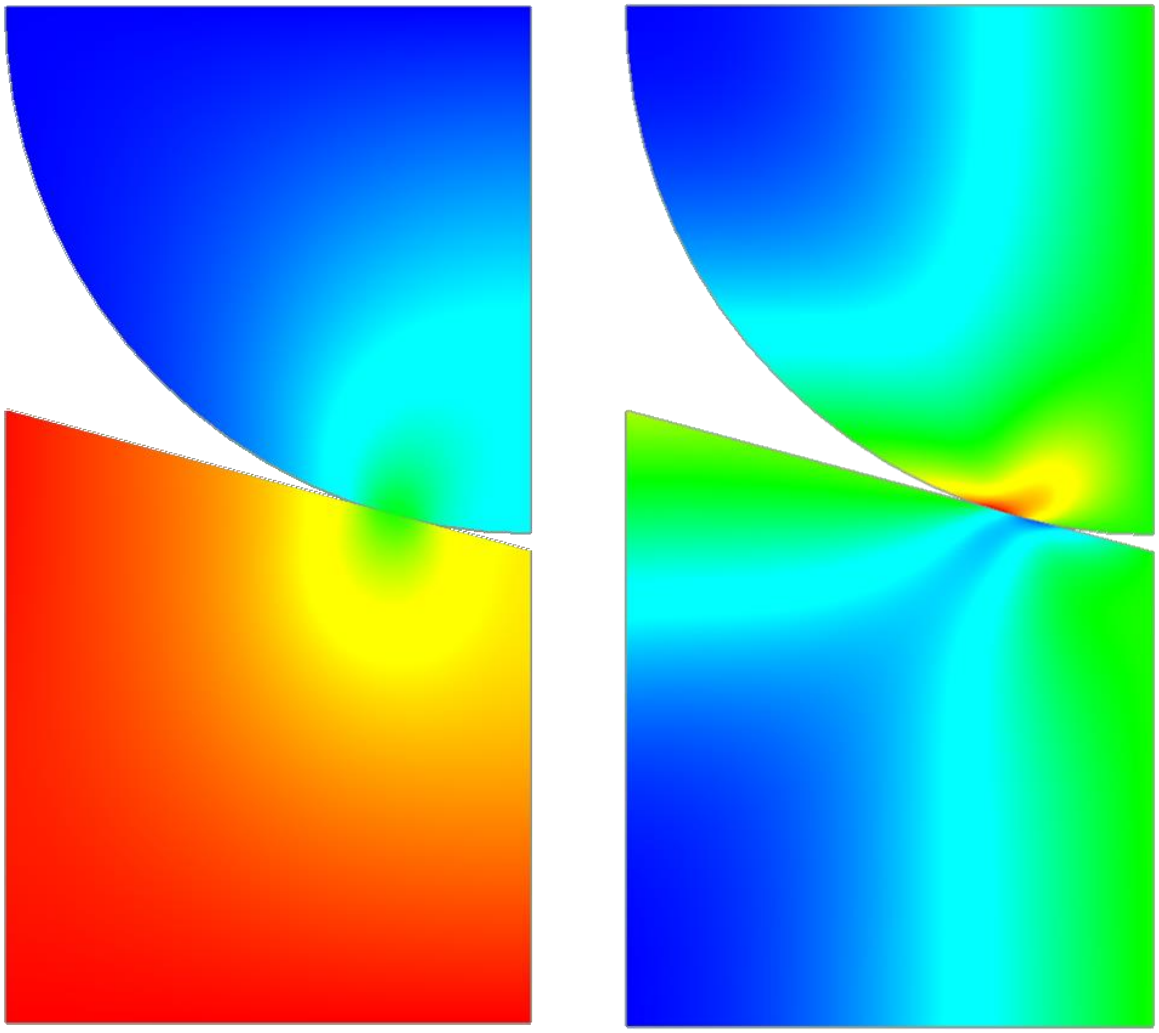

(a) (b)

Figure 6-39. (a) u_y displacement field (b) u_x displacement field for cylinder-on-wedge.

CHAPTER 7
7. CONCLUSION

7.1. Conclusion

The motivation behind the present work was to implement sliding contact in the form of sliding frictionless contact and for partial-slip contact problems.

The need for projection on to the exact surface was identified in order to achieve accurate solutions; this is highlighted in Example 1 where the results difference between the projected and non-projected results are compared. These projection algorithms where also written for 3D primitives as covered in Chapter 4 as their importance will become crucial to application of this contact solution structure to 3D.

The new algorithm was implemented for representing and identifying the region in contact by the scaler half-width a. Thus, allowing for iteratively increase and decreasing a instead of a node-to-node type contact implementation. The accuracy of this algorithm is analyzed in Example 2 in both a mesh and load independent way resulting in reliable results for the half-width a with under 3% error for sufficiently dense meshes. This allows for reducing the contact problem in 2D down to the contact point and contact half-width a.

The sliding contact formulation covered in Chapter 5 allows for unbounded movement tangent to the contact surface. This is examined in Example 3 with a Hertzian-like problem where a horizonal displacement is specified, this results in an expected discontinuity in displacements between the parts while remaining continuous in the direction normal to the contact. The sliding contact formulation was further extended to partial-slip problems where both a tied and sliding region is considered this is compared across Examples 4-6, overall, this formulation proved very accurate

regarding the contact width, and contact ratio compared to the analytical solution. The pressure distribution also matches very well to the expected Hertzian elliptical pressure distribution, however, in all examples the shear stress plotted along the contact surface was overestimated compared to the analytical result. However, the total contact forces transferred through the contact are accurate for the contact region identified and always equal and opposite between the parts. More accurate plotting along the contact region could elevate this issue, or the possibility of mesh refinement within these regions. Example 7 primarily validates the sliding contact condition even when the normal at the contact point is no longer aligned with the global coordinate system.

Together these examples show that the contact solution structure is reliable for sliding and partial-slip problems especially in regards to obtaining a solution to the size of the contact region.

7.2. Future Scope

There are many areas this work could be extended and improved. The main to consider are the extension to 3D, addition of large deformation, and more accurate stiffness based on the exact projected geometry, and dynamic/fatigue problems.

A major improvement would be the application of this algorithm to 3D, this would require a more general elliptical contact region represented by two scalers (semi-major and minor axis lengths), application of projection algorithms would allow for easy identification of the delta vector.

Large deformation would greatly extend the application of this solution structure; this would allow rigid body motion as well as continuously updating the mesh and contact elements. This would also eliminate the issues of elements deforming past each other. Projection can still be used based to improve accuracy by virtue of knowing the

exact undeformed geometry. Self-intersection could be implemented and achieved considering contact elements between the same geometry.

Using mesh refinement would allow for more accurate solutions however currently the mesh size is limited to prevent the underlying meshes of the contact element from deforming so far such that they are over a different corresponding background mesh. Alike adding large deformation to solve this a requirement for re-searching for contact elements as the non-linear solver progresses.

The use of exact projection to improve the accuracy of the element stiffness. As so far, the exact projection is limited to use on boundary integrals and has not been implemented to improve the accuracy of volume integration, this has relevancy to all problems within the IBFEM method not only contact problems. More exact stiffness integration would have the effect of eliminating stress risers from triangles (or tetrahedrons) constructed from the approximate tessellated representation.

A large area of interest for partial-slip contact is from the fretting phenomena which arise from cyclical loading which can cause premature failure rooted within the sliding region [12].

LIST OF REFERENCES

[1] N.-H. Kim, “Finite Element Analysis for Contact Problems,” *Introduction to Nonlinear Finite Element Analysis*, pp. 367–426, 2015, doi: 10.1007/978-1-4419-1746-1_5.

[2] A. V. Kumar, “Survey of Immersed Boundary Approaches for Finite Element Analysis,” *Journal of Computing and Information Science in Engineering*, vol. 20, no. 4, Aug. 2020, doi: 10.1115/1.4045054.

[3] R. K. Burla, A. V. Kumar, and B. V. Sankar, “Implicit boundary method for determination of effective properties of composite microstructures,” *International Journal of Solids and Structures*, vol. 46, no. 11–12, pp. 2514–2526, Jun. 2009, doi: 10.1016/J.IJSOLSTR.2009.02.003.

[4] A. S. Tupsakhare, “CONTACT MODELING USING IMPLICIT BOUNDARY FINITE ELEMENT APPROACH,” University of Florida, 2012. Accessed: Feb. 13, 2022. [Online]. Available: https://ufdc.ufl.edu/UFE0044240/00001

[5] S. S. Nittala, “MODELING CONTACT AS A NON-LINEAR PROBLEM USING IMPLICIT BOUNDARY FINITE ELEMENT APPROACH,” University of Florida, 2021. Accessed: May 13, 2022. [Online]. Available: https://ufdc.ufl.edu/UFE0057572/00001

[6] G. Kloosterman, “Contact Methods in Finite Element Simulations,” 2002, Accessed: Jun. 13, 2022. [Online]. Available: www.nimr.nl

[7] P. Wriggers, “Finite element algorithms for contact problems,” *Archives of Computational Methods in Engineering 1995 2:4*, vol. 2, no. 4, pp. 1–49, 1995, doi: 10.1007/BF02736195.

[8] P. Wriggers, “Computational contact mechanics,” *Computational Contact Mechanics*, pp. 1–518, 2006, doi: 10.1007/978-3-540-32609-0/COVER.

[9] J. C. Simo and T. A. Laursen, “An augmented lagrangian treatment of contact problems involving friction,” *Computers & Structures*, vol. 42, no. 1, pp. 97–116, Jan. 1992, doi: 10.1016/0045-7949(92)90540-G.

[10] R. Weyler, J. Oliver, T. Sain, and J. C. Cante, “On the contact domain method: A comparison of penalty and Lagrange multiplier implementations,” *Computer Methods in Applied Mechanics and Engineering*, vol. 205–208, no. 1, pp. 68–82, Jan. 2012, doi: 10.1016/J.CMA.2011.01.011.

[11] H. Hertz, “Ueber die Berührung fester elastischer Körper,” *Journal fur die Reine und Angewandte Mathematik*, vol. 1882, no. 92, pp. 156–171, Jan. 1882, doi: 10.1515/CRLL.1882.92.156/MACHINEREADABLECITATION/RIS.

[12] D. A. Hills and D. Nowell, *Mechanics of Fretting Fatique*, vol. 30. Dordrecht: Springer Netherlands, 1994. doi: 10.1007/978-94-015-8281-0.

[13] Q. Li and V. L. Popov, “NORMAL LINE CONTACT OF FINITE-LENGTH CYLINDERS,” *FACTA UNIVERSITATIS Series: Mechanical Engineering*, vol. 15, pp. 63–71, 2017, doi: 10.22190/FUME170222003L.

[14] K. L. Johnson, *Contact Mechanics*. Cambridge University Press, 1985. doi: 10.1017/CBO9781139171731.

[15] V. L. Popov, *Contact Mechanics and Friction*. Berlin, Heidelberg: Springer Berlin Heidelberg, 2010. doi: 10.1007/978-3-642-10803-7.

[16] “Contact - SOLIDWORKS Manual,” *Dassault Systèmes*. 2021. Accessed: May 15, 2022. [Online]. Available: https://help.solidworks.com/2021/english/SolidWorks/cworks/c_Contact.htm
[17] V. Popov, “Stresses produced by a contact with a combined normal and tangential load made visible by polarization optics.” Nov. 2008. Accessed: Jun. 13, 2022. [Online]. Available: https://commons.wikimedia.org/wiki/File:Kontakt_Spannungsoptik.JPG
[18] N. H. Kim and B. v. Sankar, “Introduction to finite element analysis and design,” p. 419, 2009.
[19] D. Gilbarg and N. S. Trudinger, “Boundary Gradient Estimates,” pp. 333–358, 2001, doi: 10.1007/978-3-642-61798-0_14.
[20] I. Temizer, P. Wriggers, and T. J. R. Hughes, “Contact treatment in isogeometric analysis with NURBS,” *Computer Methods in Applied Mechanics and Engineering*, vol. 200, no. 9–12, pp. 1100–1112, Feb. 2011, doi: 10.1016/J.CMA.2010.11.020.
[21] D. Eberly, “Distance from a Point to an Ellipse, an Ellipsoid, or a Hyperellipsoid,” 2013. [Online]. Available: https://www.geometrictools.com/
[22] J. Corney, *3d Modeling Using the Acis Kernel and Toolkit*, 1st ed. USA: John Wiley & Sons, Inc., 1997.
[23] E. W. Weisstein, *CRC Concise Encyclopedia of Mathematics*. Chapman and Hall/CRC, 2002. doi: 10.1201/9781420035223.
[24] K.-J. Bathe and E. N. Dvorkin, “ON THE AUTOMATIC SOLUTION OF NONLINEAR FINITE ELEMENT EQUATIONS,” *Compurers & S~ruchrres*, vol. 17, no. M, pp. 871–879, 1983.
[25] R. S. Bradley, “LXXIX. The cohesive force between solid surfaces and the surface energy of solids,” *http://dx.doi.org/10.1080/14786449209461990*, vol. 13, no. 86, pp. 853–862, Apr. 2009, doi: 10.1080/14786449209461990.
[26] J. Wang and D. Zhu, “Elliptical Contact of Surfaces,” *Encyclopedia of Tribology*, pp. 967–967, 2013, doi: 10.1007/978-0-387-92897-5_100420.
[27] C. Broniewska and M. S. Mitra, “Photoelastic Method for Stress Analysis,” 1953.

BIOGRAPHICAL SKETCH

John Dews-Flick was born in Clearwater, Florida but spent most of his childhood in Chapel Hill, North Carolina. During high school John started working as a programmer for an eCommerce startup; continuing this work through college. John earned his Bachelor's (2021) and Master's (2022) in Aerospace Engineering from Herbert Wertheim College of Engineering at the University of Florida. John's interest includes programing, solid mechanics, fluid mechanics, design optimization, and finite element analysis.